

Technische Universität München

Chair of Nuclear Technology

Prof. Macián-Juan

Master Thesis

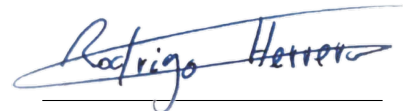
Calculation of the thermal stress on target tiles for the
new upper divertor in ASDEX Upgrade

Author:	Rodrigo Herrero Álvarez de Araya
Matriculation Number:	03727205
Address:	Boltzmannstraße 15 85748, Garching bei München
Academic supervisor:	Prof. Dott. Antonino Cardella
IPP supervisor:	Dr. Irene Zammuto
IPP supervisor:	Dr. Albrecht Herrmann
Submitted on:	1st of December 2020

With my signature below, I assert that the work in this thesis has been composed by myself independently and no source materials or aids other than those mentioned in the thesis have been used.

München, December 1, 2020

Place, Date

A handwritten signature in blue ink that reads "Rodrigo Herrera". The signature is written in a cursive style and is positioned above a horizontal line.

Signature

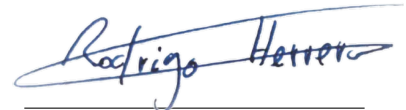
This work is licensed under the Creative Commons Attribution 3.0 Germany License. To view a copy of the license, visit <http://creativecommons.org/licenses/by/3.0/de>

Or

Send a letter to Creative Commons, 171 Second Street, Suite 300, San Francisco, California 94105, USA.

München, December 1, 2020

Place, Date

A handwritten signature in blue ink that reads "Rodrigo Herrera". The signature is written in a cursive style and is positioned above a horizontal line.

Signature

Abstract

ASDEX Upgrade (AUG) is an experimental Tokamak (www.aug.ipp.mpg.de) in operation since 1991. It is a midsize Tokamak designed for power exhaust research with an ITER-relevant normalized heating power P/R of 15 MW/m. Over the years, many upgrades have been realized and in the next years a new upper divertor with in-vessel coils will be installed. The aim of the project is to prove that alternative divertor configurations (X-divertor or Snowflake divertor) can mitigate the exhaust power problem. To realize the required magnetic configurations, two poloidal field coils close to the strike line must be integrated in the design of the divertor. This upgrade will be carried out in the upper divertor of AUG that, since its building, has never been modified. Therefore, new components are going to be installed in 2022: cryopump, inner and outer divertor targets, and the in-vessel coils.

The design of the outer divertor is strongly driven by the integration of the coils in the divertor modules and necessity of helicity in the magnetic field configurations. To combine both, the outer divertor is designed as a stiff ring consisting of modules flanged together that do not need to be tilted. The target elements are made of graphite coated with tungsten and they are mounted inside the vacuum vessel in the already existing toroidal ring structure. The shape of the targets is optimized to reduce the effect of leading edges that cause an increment of the heat flux due to the orientation of the smashing particles

The outer upper divertor has three types of target design. The one expecting the higher heat flux is designed without front mounting holes, to avoid any edge effect. The maximum expected heat flux power is in the order of 10 MW/m² and the targets are weakly cooled. They receive the energy during the 10 s long pulse and are cooled down via the clamping to the water-cooled support structure in between discharges. This master thesis is focused on the evaluation of the thermal stresses in this special graphite target, which is designed to protect the in-vessel components. Non-linear modelling was used, including contacts and material properties as function of the temperature. The FEM code used for the thermomechanical simulations is ANSYS. After the completion of the analyses an experimental campaign in a high heat flux test facility was performed. The results from which allowed to validate the simulation design. Finally, normal operation at ASDEX Upgrade was modelled to assess the performance and resistance of the tile.

Contents

Abstract	ii
Contents	ii
List of Figures	v
List of Tables	viii
1 Introduction	1
1.1 Nuclear fusion	1
1.1.1 Binding Energy per nucleon	1
1.1.2 D-T mass defect calculation	2
1.1.3 Nuclear reactions	2
1.1.4 Tritium as a fuel	3
1.1.5 Coulomb barrier	3
1.2 Fusion devices	5
1.2.1 Thermonuclear reactors	5
1.2.2 Tokamak and Stellarator	5
1.2.3 Elements in a Tokamak type reactor	7
1.2.4 Divertor	9
2 State of the art	11
2.1 ASDEX Upgrade	11
2.2 ASDEX Upgrade upper divertor (DivIIo)	13
2.2.1 Upper outer divertor	13
2.2.2 Graphite as a plasma facing component (PFC)	15
2.2.3 Tile description	16
2.2.4 Installation and clamping mechanism	16
3 Material and methods	19
3.1 Software	19
3.1.1 Finite Element Analysis (FEA)	19
3.1.2 CAD software	20

3.2	Material properties	20
3.2.1	Mechanical properties of R6710 and Papyex	20
3.2.2	Failure criteria	22
3.2.3	Thermal properties of R6710 and Papyex	23
3.2.4	Stainless steel	26
3.3	Simulation	26
3.3.1	Meshing	26
3.3.2	Contact behaviour	28
3.3.3	Thermal simulation	30
3.3.4	Mechanical simulation	31
3.4	GLADIS experimental campaign	32
3.4.1	Garching LArge DIvertor Sample (GLADIS) test facility	32
3.4.2	Campaign definition	32
3.4.3	Experimental setup	34
3.5	AUG upper divertor simulation	36
4	Results	37
4.1	GLADIS experimental campaign	37
4.1.1	Infrared imaging and surface temperature	37
4.1.2	Thermocouple data	40
4.1.3	Mechanical results and inspection	42
4.2	Thermomechanical simulation of GLADIS	44
4.2.1	Thermal simulation (GLADIS)	44
4.2.2	Mechanical simulation (GLADIS)	48
4.3	Thermomechanical simulation of AUG divertor	52
4.3.1	Thermal simulation (AUG)	52
4.3.2	Mechanical simulation (AUG)	55
5	Discussion	57
5.1	GLADIS experimental campaign	57
5.1.1	Thermal simulation and comparison to experimental data	57
5.1.2	Mechanical simulation of GLADIS tests	62
5.2	AUG plasma simulation	63
6	Conclusions	65
	Bibliography	67
A	Technical drawings	69
A.1	Graphite tile (CWB-0071D)	71
A.2	Sensor locations and beam positions	73
B	Developed codes	75
B.1	Deposited energy calculation	75

B.2 Bivariate Gaussian heat source in APDL 79

List of Figures

1.1	Average binding energy of the atoms with the mass number.	1
1.2	Simplified fusion power plant. IPP.	5
1.3	Sketch of a magnetically confined plasma where φ refers to the toroidal direction and θ to the poloidal.	6
1.4	(a) Central solenoid. (b) Poloidal field coils.	7
1.5	ITER Tokamak layout drawing. ITER.	8
1.6	ITER Divertor element with main parts named. ITER.	9
1.7	ITER divertor poloidal distribution of thermal loads. F. Escourbiac [3]. . .	10
2.1	Main elements of ASDEX Upgrade Tokamak.	11
2.2	Main elements of ASDEX Upgrade upper divertor.	13
2.3	Main elements of an AUG upper outer divertor module.	14
2.4	Design parameters for the toroidal gap size, where β is the chamfer angle and α_m maximum pitch angle.	14
2.5	Sublimation of graphite in vacuum.	15
2.6	ASDEX Upgrade upper divertor cross section with installed tiles.	16
2.7	Exploded view of the clamping mechanism.	17
3.1	ANSYS simulation path	19
3.2	Model simplifications applied to the original CATIA design.	20
3.3	Final 3D model for FEA with simplifications.	21
3.4	Yield of R6710 variation with temperature.	22
3.5	Mohr Coulomb and maximum stress criterion for 2D stress, where σ_1 and σ_2 are the two principal stresses and S_t and S_c are the tensile and compression limits, respectively.	23
3.6	Specific heat of graphite components according to ASTM standard practice for testing graphite and boronated graphite materials for high-temperature gas-cooled nuclear reactor components (C781).	24
3.7	Thermal conductivity of graphite components.	25
3.8	Thermal expansion of graphite R6710.	25
3.9	(a) Hexahedral linear element. (b) Hexahedral quadratic element.	27
3.10	Skewness bar plot of the generated mesh.	27
3.11	(a) Meshing poloidal direction. (b) Meshing toroidal direction.	28

3.12	Mesh convergence around stress concentrator.	29
3.13	Normalized AUG heat distribution with $[\sigma_x, \sigma_y] = [50, 6]$ mm and centre at 40 mm.	30
3.14	(a) Deformed graphite tile during preload ($\times 1.7 \cdot 10^4$ amplification factor). (b) Contact pressure on clamping region during preload.	31
3.15	View of the GLADIS test chamber.	32
3.16	Heat source axis information for GLADIS experiments.	33
3.17	Gaussian fits and measured beam profiles for 6 distributions of: 130 kW (1), 155 kW (2), 182 kW (3), 252 kW (4), 353 kW (5) and 560 kW (6). H. Greuner [4].	34
3.18	Experimental setup (a) upper side (b) lower side.	35
3.19	Sensor location of test tile for GLADIS experiment.	36
4.1	Maximum surface temperatures of the 10 MW/m ² tests with (a) centred beam and (b) beam focused on the clamping region.	38
4.2	Maximum surface temperatures of the 25 MW/m ² tests with (a) centred beam and (b) beam focused on the clamping region.	39
4.3	Temperature at the beginning of the pulse on thermocouples inserted in the clamps.	40
4.4	(a) Transient data from 10 MW/m ² experiments #248575 and #248596. (b) Transient data from 25 MW/m ² experiments #248647 and #248667.	41
4.5	(a) Inspection with microscope. (b) Heat abrasion on graphite surface ($\times 40$ amplification).	42
4.6	GLADIS test scenario 3. (a) Before pulse. (b) Pulse start. (c) Maximum displacement.	43
4.7	Interest location of simulation results.	44
4.8	Heat source distribution for the 10 MW/m ² and 25 MW/m ² with peak centres in 100 mm and 40 mm, respectively.	45
4.9	Temperature distribution of the upper and rear side of the tile during 10 MW/m ² for 3.5s with centred beam (1 - GLADIS).	46
4.10	Temperature distribution of the upper and rear side of the tile during 10 MW/m ² for 3.5s with beam focused on the clamp (2 - GLADIS).	46
4.11	Temperature distribution of the upper and rear side of the tile during 25 MW/m ² for 1s with centred beam (3 - GLADIS).	47
4.12	Temperature distribution of the upper and rear side of the tile during 25 MW/m ² for 1s with beam focused on the clamp (4 - GLADIS).	47
4.13	Clamping slot with stress concentrator.	48
4.14	Total deformation of the 1 - GLADIS scenario ($\times 10$ amplification factor).	49
4.15	Total deformation of the 2 - GLADIS scenario ($\times 10$ amplification factor).	50
4.16	Total deformation of the 3 - GLADIS scenario ($\times 8.5$ amplification factor).	50
4.17	Total deformation of the 4 - GLADIS scenario ($\times 8.5$ amplification factor).	51
4.18	Heat flux at the peak location for the 15 MW/m ² and 7 MW/m ² distributions.	52
4.19	Heat flux distribution for the two AUG scenarios.	53

4.20	Temperature distribution of the upper and rear side of the tile during 15 MW/m ² for 3s with beam focused on the clamp (1-AUG).	54
4.21	Temperature distribution of the upper and rear side of the tile during 7 MW/m ² for 10s with beam focused on the clamp (2-AUG)	54
4.22	Total deformation of the 1 - AUG scenario (x43 amplification factor). . . .	55
4.23	Total deformation of the 2 - AUG scenario (x64 amplification factor). . . .	56
5.1	Temperature measured in the poloidal symmetry axis during a 10MW/m ² after 3.5s pulse.	58
5.2	Simulation and experimental temperature evolution for GLADIS scenario 1.	60
5.3	Simulation and experimental temperature evolution for GLADIS scenario 2.	60
5.4	Simulation and experimental temperature evolution for GLADIS scenario 3.	61
5.5	Simulation and experimental temperature evolution for GLADIS scenario 4.	61
5.6	Temperature evolution for the two AUG scenarios.	63
B.1	Mesh of the trapezoidal calculation space.	78
B.2	Normalized power surface graph.	78

List of Tables

1.1	Main nuclear reactions, where D and T represent deuterium and tritium, respectively.	2
2.1	Technical data of ASDEX upgrade.	12
3.1	Mechanical properties of graphite materials at room temperature.	21
3.2	Yield of graphite R6710 variation with temperature.	22
3.3	Thermal properties of graphite components at room temperature.	24
3.4	Mechanical and thermal properties of 316L(N)-IG and 304LN steels, characterized according to ITER at room temperature.	26
3.5	Contact behaviour defined on the simulation.	29
3.6	Parameters of the bivariate Gaussian distribution heat source applied on the graphite tile for the GLADIS tests.	34
3.7	Parameters of the Gaussian distribution applied to the graphite tile during AUG plasma.	36
4.1	Beam characteristics and maximum surface temperature results from GLADIS tests.	37
4.2	Measured temperature on thermocouples attached to the graphite tile (1, 2) and inserted on the clamps (3, 4).	40
4.3	Displacement measured on the tile during pulses.	42
4.4	Parameters of the Gaussian distribution heat source applied on the graphite tile.	44
4.5	Heat flux and temperature in the areas of interest in GLADIS simulation.	45
4.6	Displacement and principal stresses on GLADIS mechanical simulation.	49
4.7	Updated yield strength and safety factor of GLADIS tests.	51
4.8	Parameters of the Gaussian distribution heat source applied on the graphite tile in the AUG scenario simulation.	52
4.9	Heat flux and temperature in the areas of interest of AUG simulation.	53
4.10	Displacement and principal stresses on AUG mechanical simulation.	55
4.11	Updated yield strength and safety factor of GLADIS tests.	56

5.1	Maximum surface temperatures of GLADIS (G) and simulation (S) result comparison.	57
5.2	Displacement measured on the tile during pulses and simulation results. . .	62

Chapter 1

Introduction

1.1 Nuclear fusion

1.1.1 Binding Energy per nucleon

The measured mass of the atom is lower than the mass of its constituents (protons, neutrons and electrons). This difference, defined as the mass defect, is proportional to the binding energy (BE) of the nucleus. Figure 1.1 presents two nuclear reaction regions and the area of high stability. In the fission region, heavier elements are transformed into lower mass and more stable elements. Maximum BE per nucleon is found at Fe^{56} , which is the most stable element. A relative maximum is found in the fusion region for He^4 , where the average BE is 7.07 MeV/nucleon with a total energy of 28.28 MeV.

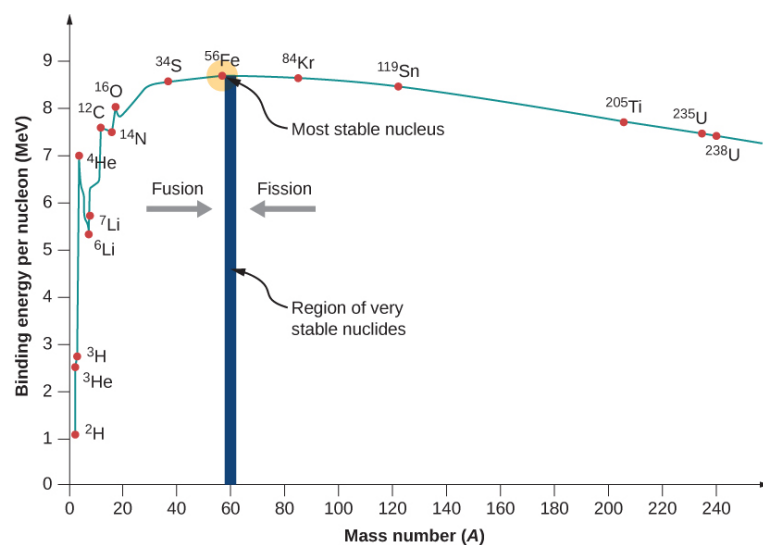
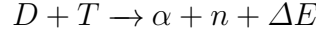


Figure 1.1: Average binding energy of the atoms with the mass number.

1.1.2 D-T mass defect calculation

During fusion part of the mass is transformed into energy to bound the nucleons together. This energy is carried by the resulting fusion products.



$$m_0 = m_D + m_T = 3.34358 \cdot 10^{-27} + 5.00736 \cdot 10^{-27} = 8.35094 \cdot 10^{-27}$$

$$m_f = m_\alpha + m_n = 6.64466 \cdot 10^{-27} + 1.67493 \cdot 10^{-27} = 8.31958 \cdot 10^{-27}$$

$$\Delta m = m_0 - m_f = 8.35094 \cdot 10^{-27} - 8.31958 \cdot 10^{-27} = 3.136 \cdot 10^{-29} \text{kg}$$

Using Einstein's equivalence, we can obtain the conversion of energy and mass.

$$\Delta E = \Delta m \cdot c^2 = 3.136 \cdot 10^{-29} \text{kg} \cdot 299792458 \text{m/s}^2 = 2.8185 \cdot 10^{-12} \text{J}$$

$$\Delta E = 2.8185 \cdot 10^{-12} \text{J} \cdot \frac{1 \text{eV}}{1.602 \cdot 10^{-19} \text{J}} = 17.59 \text{MeV}$$

1.1.3 Nuclear reactions

Table 1.1: Main nuclear reactions, where D and T represent deuterium and tritium, respectively.

Name	Reaction	Reaction	Energy (MeV)	Ref
$D - T$	$T(d, n)He^4$	$D + T \rightarrow \alpha + n$	17.59	(1)
$D - Dp$	$D(d, p)T$	$D + D \rightarrow T + p$	4.03	(2)
$D - Dn$	$D(d, n)He^3$	$D + D \rightarrow He^3 + n$	3.27	(3)
$T - T$	$T(t, 2n)He^4$	$T + T \rightarrow \alpha + 2n$	11.30	(4)
$D - He^3$	$He^3(d, p)He^4$	$D + He^3 \rightarrow \alpha + p$	18.35	(5)
$p - Li^6$	$Li^6(p, \alpha)He^3$	$p + Li^6 \rightarrow \alpha + He^3$	4.02	(6)
$p - B^{11}$	$B^{11}(p, 2\alpha)He^4$	$p + B^{11} \rightarrow 3\alpha$	8.68	(7)

The two branches of the D-D reactions (2) and (3) have roughly equal probabilities. Additionally, if the products of these reactions can react with D atoms the catalysed D-D (Reac. 1.1) will occur. Reactions like these require much higher temperatures to happen at high enough rates.



Reactions (5), (6) and (7) do not generate neutrons, so they would not cause nuclear activation, thus they are known as non-radioactive nuclear fusion. However, in a reactor with presence of D (like on 5), D-D reactions will occur.

Finally, B and Li based reactors (6)(7) do not use or generate D, therefore nuclear activation would not occur. However, the technology to make them viable does not exist yet, which is why they are called exotic fuels.

1.1.4 Tritium as a fuel

Currently the only nuclear fusion considered as economically and energetically viable is the D-T (1), because its maximum reaction rate occurs at the lowest temperature. One drawback of this reaction is the fact that tritium's half-life is only 12.3 years (Reac. 1.2), meaning that it is a radioactive isotope that must be artificially produced. Tritium experiences beta decay into He^3 , electron and an electron antineutrino:



Nowadays, most tritium is produced in fission reactors by neutron activation of Li^6 rods (Reac. 1.3). In the future, it will also be created in breeding blankets located inside of fusion reactors.



1.1.5 Coulomb barrier

In order to achieve fusion of two colliding nuclei, electric repulsion must be overcome. The Coulomb repelling force (Eq. 1.4) is proportional to the product of the atomic numbers of the interacting particles and grows with the inverse of the square of the distance. If the barrier is considered to be the electric potential energy of the two atoms:

$$U = \frac{Z_1 Z_2 e^2}{4\pi\epsilon_0 r} = k_e \cdot \frac{Z_1 Z_2 e^2}{r} \quad (1.4)$$

where

Z_1 = Atomic number of particle 1.

Z_2 = Atomic number of particle 2.

e = Proton charge.

ϵ_0 = Permittivity of the vacuum.

k_e = Coulomb constant.

r = Distance between nucleus.

If the distance is small enough the nuclei will enter the zone of influence of the strong nuclear force, which predominate over the coulomb repelling force, resulting in fusion. This distance is given by the effective radius r_k of the nucleus, that can be approximated with equation 1.5.

$$r_k = r_o \cdot A^{1/3} \quad (1.5)$$

Where

$$r_o = (1.3 \pm 0.1) \cdot 10^{-15} \text{ m.}$$

A = Mass number of the atom.

As an example the coulomb barrier for the D-T interaction is calculated. For this reaction, the radius of maximum potential energy is known to be $r_m = 3.7 \cdot 10^{-15}$ m.

$$U_{max,D-T} = \frac{1.1 \cdot (1.602 \cdot 10^{-19})^2}{4 \cdot \pi \cdot 8.85 \cdot 10^{-12} \cdot r_m} = 6.237 \cdot 10^{-14} \text{ J} = 0.4 \text{ MeV}$$

$$T_{D-T} = \frac{0.4 \text{ MeV}}{8.62 \cdot 10^{-5} \text{ eV/K}} = 4.6 \cdot 10^9 \text{ K}$$

D-T fusion temperature calculated through the Coulomb barrier reaches $4.6 \cdot 10^9$ K. However, fusion occurs at much lower temperatures thanks to various phenomena such as higher energy particles in the Maxwellian distribution, quantum tunnelling and higher than proton radius for the interaction distance of the strong nuclear force. These lower the critical temperature to:

$$T_{D-T} = 4.5 \cdot 10^7 \text{ K}$$

$$T_{D-D} = 4 \cdot 10^8 \text{ K}$$

With the D-D fusion temperature being an order of magnitude higher. This threshold is the reason why they are considered advanced fuel reactions.

1.2 Fusion devices

1.2.1 Thermonuclear reactors

There are two main types of thermonuclear reactors, those which use magnetic confinement, such as Tokamaks and Stellarators and those with inertial confinement, the latter being beyond the scope of the current work. At the moment, the only reaction considered for power generation is D-T. As mentioned before, T will be produced, inside of fusion power plants. With that in mind, a simplified sketch is shown in figure 1.2, which shows the fuel and exhaust flows.

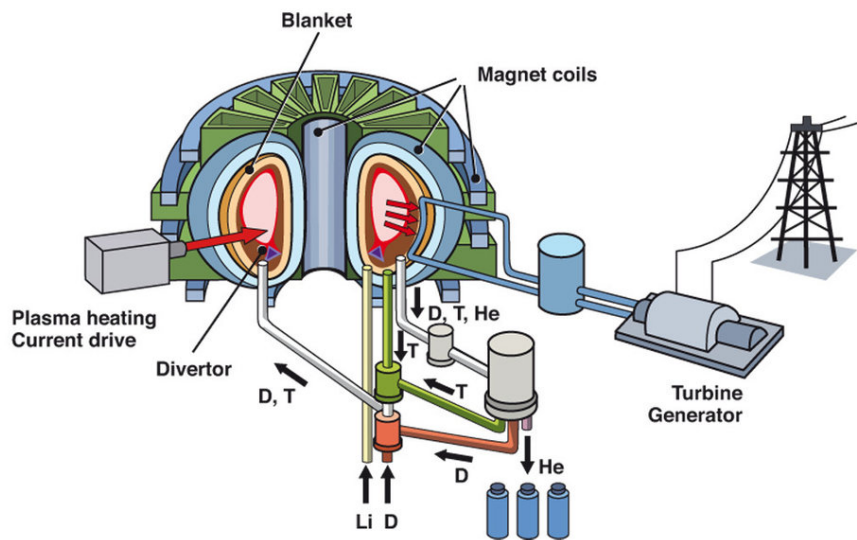


Figure 1.2: Simplified fusion power plant. IPP.

1.2.2 Tokamak and Stellarator

Magnetic confinement is obtained by the generation and control of field lines across a toroidally shaped vacuum chamber. A toroidal magnetic field is used to guide the particles along the torus, whilst a poloidal field is needed to compensate particle drifts and increase confinement. Figure 1.3 shows the main parameters of a magnetically confined plasma.

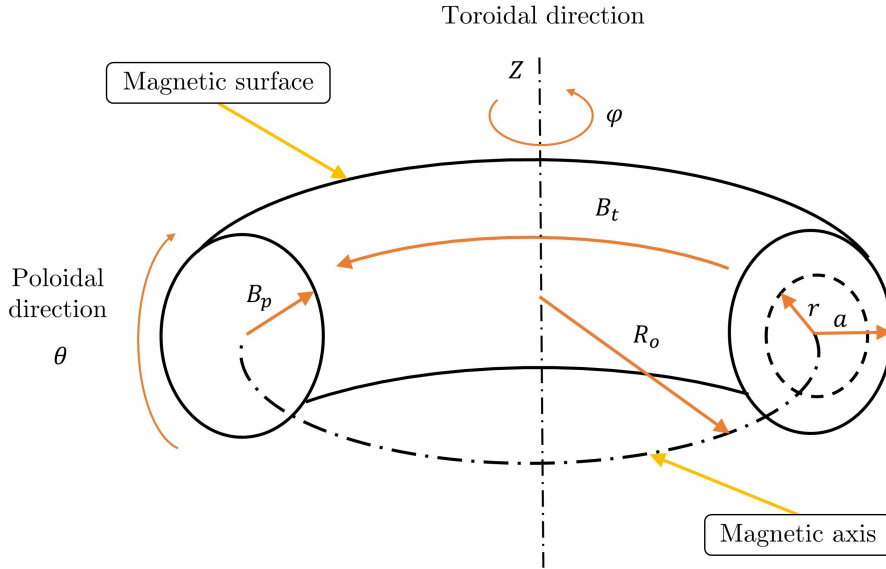


Figure 1.3: Sketch of a magnetically confined plasma where φ refers to the toroidal direction and θ to the poloidal.

- Major axis (Z): Axis of revolution of the torus.
- Major radius (R): Distance from the major axis.
- Plasma magnetic axis: Line along $B_p = 0$. There might be more than one axis.
- Plasma major radius (R_o): Distance to the magnetic axis.
- Minor radius (r): Distance from magnetic axis to magnetic surface.
- Plasma minor radius (a): Distance to the last closed magnetic surface from the magnetic axis.
- Plasma height (b): Height of the plasma measured from the equatorial plane.
- Elongation: Ratio between minor radius and plasma height $\kappa = \frac{b}{a}$.
- Toroidal field (B_T): Magnetic field in the toroidal direction and primary confinement mechanism. It induces the charged particles to move in a spiral motion centred on the field line.
- Poloidal field (B_P): Magnetic field in the poloidal direction. Induces particles to girate in the poloidal direction and increases with the minor radius. Increasing its value, increases the number of turns in the θ direction while doing one toroidal turn.

In a TOKAMAK (Toroidal Chamber With Magnetic Coils) the B_p is generated by induction of a plasma current in the vacuum chamber. This is done by inserting a vertical stack of planar coils in the central region of the torus (Fig. 1.4a). If the current in the coils is varied, a current (I_p) is induced in the plasma, which behaves like a secondary loop of a transformer. The I_p circulates until a maximum current is reached in the solenoid. At that moment the current is ramped down and a new cycle can be started. Additionally, poloidal coils (Fig. 1.4b) are placed on the upper and lower parts of the torus to increase stability. They also allow to detach the plasma from the wall during start-up.

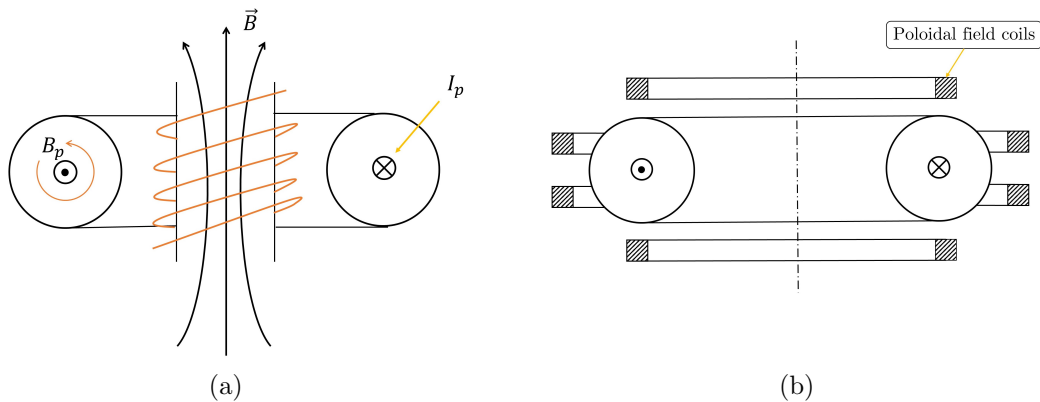


Figure 1.4: (a) Central solenoid. (b) Poloidal field coils.

The main advantages of the Tokamak principle are the intrinsic heating and the advancement of the technology. Disadvantages are its pulsed operation and the possibility of disruptions. Models include JET (Joint European Torus, UK), JT 60 SA (Japan), Tore Supra (France), ASDEX Upgrade (Germany).

In Stellarators two types of magnets are used: toroidal field generators and helicoidal conductors. The B_p is created with helical coils wrapped around the vacuum vessel. Therefore a plasma current is not needed, meaning steady state operation can be reached. The main disadvantage of this concept is the complex geometry of the machine due to the field shape. Models include Large Helical Device (LHD, Japan) and Wendelstein 7-X (Germany).

1.2.3 Elements in a Tokamak type reactor

Figure 1.5 shows the basic layout of the ITER Tokamak

- Cryostat (16,000 m³): Stainless steel high-vacuum chamber. Approximately 30 m in height.
- Vacuum vessel (1,400 m³): Steel container with double walls that acts as the first containment barrier and has circulating water to extract heat.

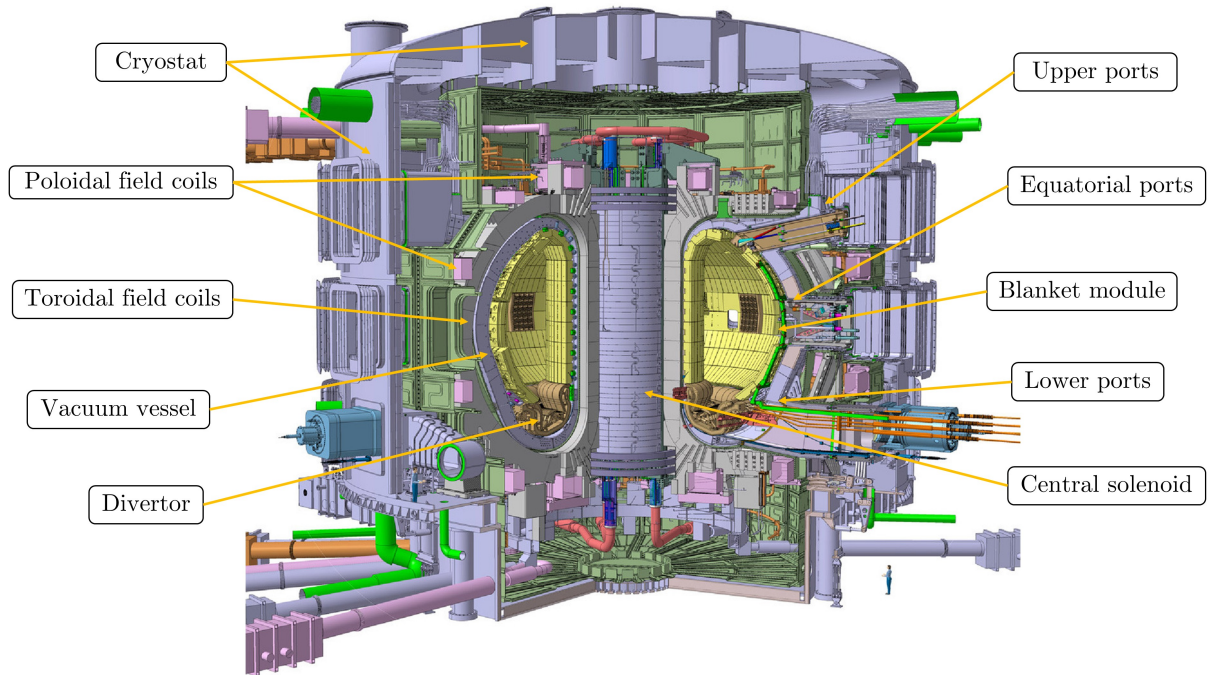


Figure 1.5: ITER Tokamak layout drawing. ITER.

- Divertor: Tungsten structure which acts as the exhaust system of the alpha particle power and ash from the fusion reactions. It aids in minimizing plasma impurity and will withstand the highest heat loads, between 10 and 20 MW/m² (Fig. 1.7).
- Blanket modules: They provide shielding from high-energy neutrons and tritium breeding blankets will be tested.
- Toroidal field coils (11.8 T): Eighteen magnets of 360 tonnes each will confine the plasma particles.
- Poloidal field coils (6 T): Six magnets 400 tonnes each to aid in plasma shaping and detachment of the wall.
- Central solenoid (13 T): Niobium-tin superconducting cable coils. Will generate a plasma current of 15 MA for up to 500s.
- Ports: Allow access to the machine for fuelling, maintenance, diagnostics, heating, and vacuum pumping systems.

1.2.4 Divertor

In Tokamak and Stellarator type reactors exists a boundary between closed and open field lines called separatrix. It separates the confined region with the one where field lines connect to material surfaces inside the plasma chamber. This last closed magnetic surface usually converges in an X-point, which corresponds to a single null configuration. In Tokamak reactors usually one divertor is placed below the plasma to exhaust impurity particles and extract heat. Figure 1.6 shows the ITER divertor design with its main parts.

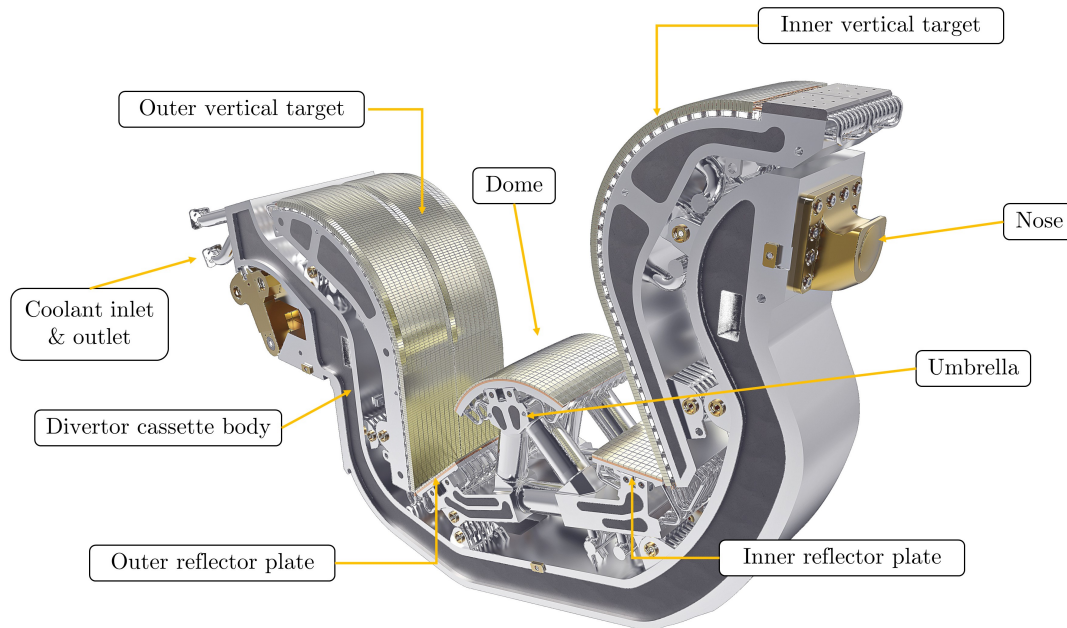


Figure 1.6: ITER Divertor element with main parts named. ITER.

The inner and outer vertical targets (VT) are the plasma facing components that intercept the magnetic field lines. They absorb the main part of the heat flux coming from the plasma. Most of the particles that are not adsorbed by the VT will be in the reflector plates, protecting the cassette body. The umbrella, located below the X-point, baffles mostly alpha particles (He^4). The cassette body is made of stainless steel and provides neutron shielding to the vacuum vessel. Additionally, it contains the coolant pipes and supports the plasma facing components, which are made of solid tungsten.

The divertor is designed to withstand 5000 cycles at 10 MW/m^2 (steady state) and 300 cycles at 20 MW/m^2 (slow transients) [3]. Figure 1.7 shows the heat distribution in the poloidal direction, for steady state operation.

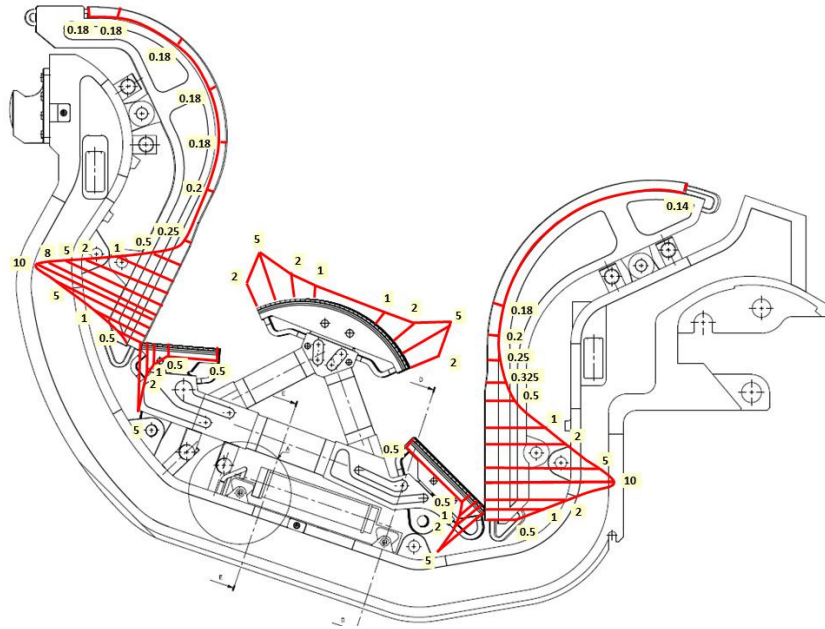


Figure 1.7: ITER divertor poloidal distribution of thermal loads. F. Escourbiac [3].

Chapter 2

State of the art

2.1 ASDEX Upgrade

ASDEX Upgrade (Axially Symmetric Divertor Experiment) is a divertor Tokamak, located at the Max-Planck-Institut für Plasmaphysik, Garching bei München. It is Germany's second largest fusion experiment after stellarator Wendelstein 7-X. Figure 2.1 contains a 3D rendering of the reactor with its main parts, note the presence of two divertors as opposed to one in ITER.

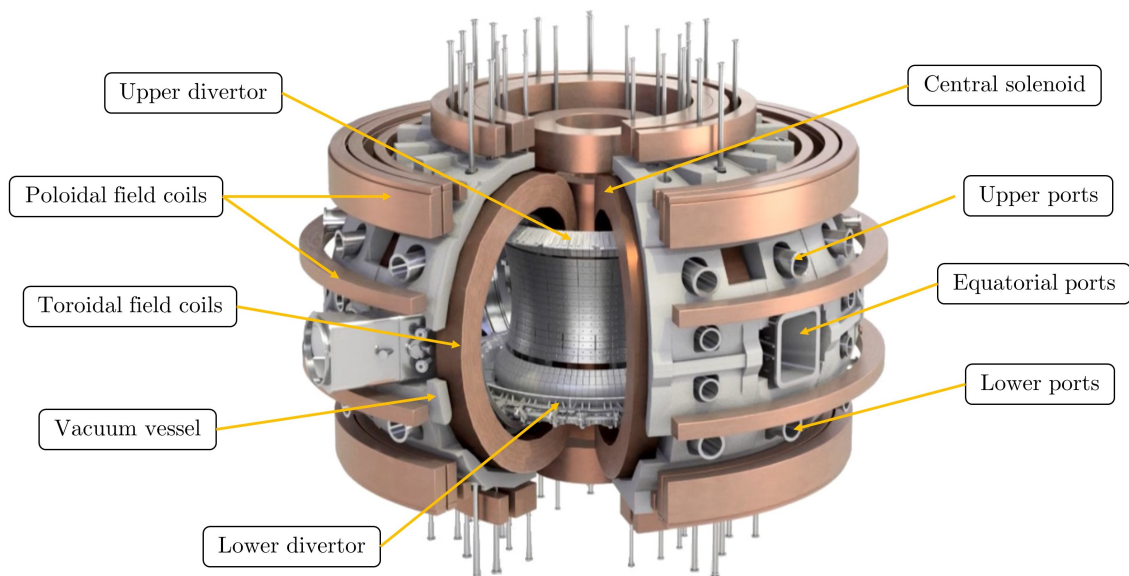


Figure 2.1: Main elements of ASDEX Upgrade Tokamak.

The first plasma discharge was generated in March 1991 and since then over 30,000 pulses have been done. ASDEX Upgrade or AUG is the successor of the older ASDEX system and is of medium size in international comparison to other Tokamaks.

The system has a diameter of 10 meters, a total weight of 800 tons and a heating capability of up to 27 MW. The machine has available neutral particle heating of 20 MW, two electromagnetic wave heating systems (ion and electron-cyclotron) up to 6 MW each and ohmic heating through plasma current of 1 MW. Table 2.1 the main characteristics of the reactor and the plasma at AUG.

Table 2.1: Technical data of ASDEX upgrade.

	Characteristic	Symbol	Value
Machine	Magnetic flux	B	3.9 T
	Weight	m	800 Tn
	Diameter	ϕ	10 m
	Height	h	9 m
	Neutral particle heating		20 MW
	Ion cyclotron heating		6 MW
	Electron cyclotron heating		4 MW
Plasma	Plasma current	I_p	0.4 to 1.6 MA
	Discharge time		10 s
	Energy confinement time	τ	0.2 s
	Major radius	R	1.65 m
	Minor radius	r	0.50 m
	Elongation	κ	1.6
	Volume	V_p	14 m ³
	Weight	m_p	3 mg
	Temperature	m_p	$150 \cdot 10^6$ K

The vacuum vessel interior is completely coated with tungsten ($Z = 74$), which has a very high melting point and is expected to absorb less tritium compared to graphite. AUG uses only deuterium as a fuel, which poses advantages in terms of research and material resistance. Additionally, D-D plasmas generate almost no activation at the working temperatures and require lower shielding than D-T.

AUG aim is to study magnetically confined plasmas in various operating modes that are relevant to ITER development. The ratio of heating power P and plasma radius R is 15 MW/m in AUG, which comes closer to ITER than any other fusion experiment worldwide. Some of the research topics studied are:

- Particle and energy transport in plasma
- Divertor studies in gentle decoupling of the plasma power.
- Investigation of plasma instabilities and turbulence.
- Development of optimized plasma states.

- Test of theoretical models on divertor physics, turbulence, and plasma transport
- Wall material studies.

Initially, the interior of AUG was completely composed of tungsten coated graphite tiles. In 2013 a redesigned solid tungsten lower divertor, Div-III, was installed. In 2016 a project began to develop and install a new upper divertor with internal coils and an in-vessel cryopump [7]. Despite the interest in an ITER like lower divertor made out of solid tungsten, the new upper divertor will remain made out of tungsten coated graphite tiles. The decision behind this was based on the good performance of the previous material and tungsten's higher price, inducted current, and fragility. Additionally, tungsten is almost 10 times heavier than graphite, which would cause much larger stresses on the clamping mechanisms, as the tiles would be hung from the upper part of the already existing support structure.

2.2 ASDEX Upgrade upper divertor (DivIIo)

2.2.1 Upper outer divertor

The new upper divertor will include internal coils, an in-vessel cryo-pump and inner and outer modules, shown in figure 2.2. The development status of these components is discussed in [7].

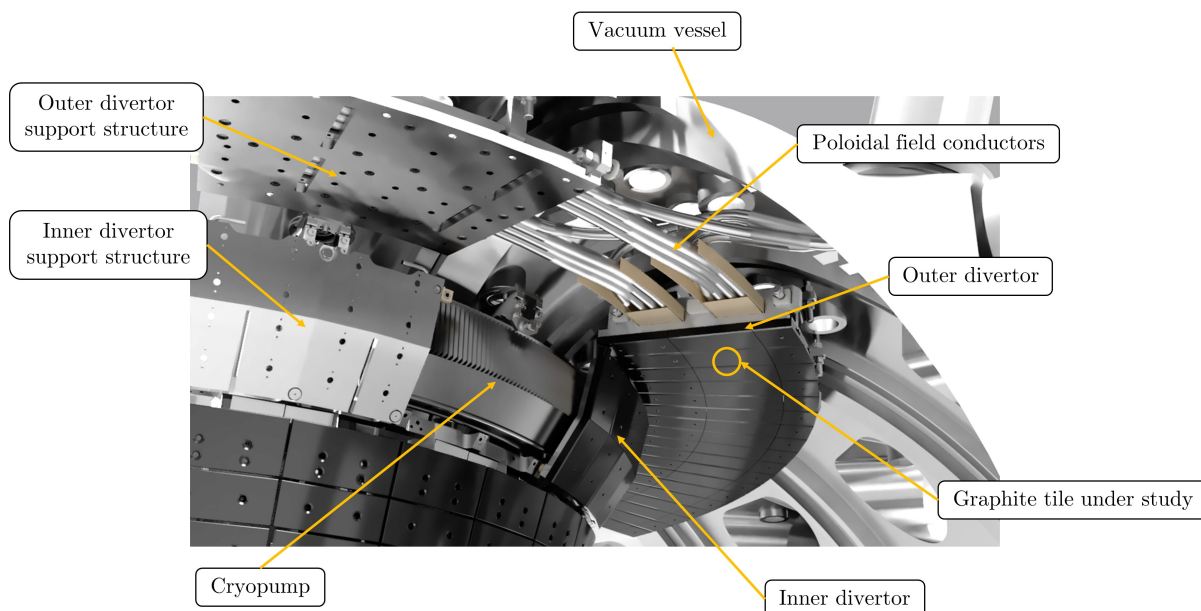


Figure 2.2: Main elements of ASDEX Upgrade upper divertor.

A module of the new upper outer divertor is composed mainly by 18 tiles, 30 clamping mechanisms, a flexible graphite layer, a solid stainless steel structure and a cooling tube (Fig. 2.3).

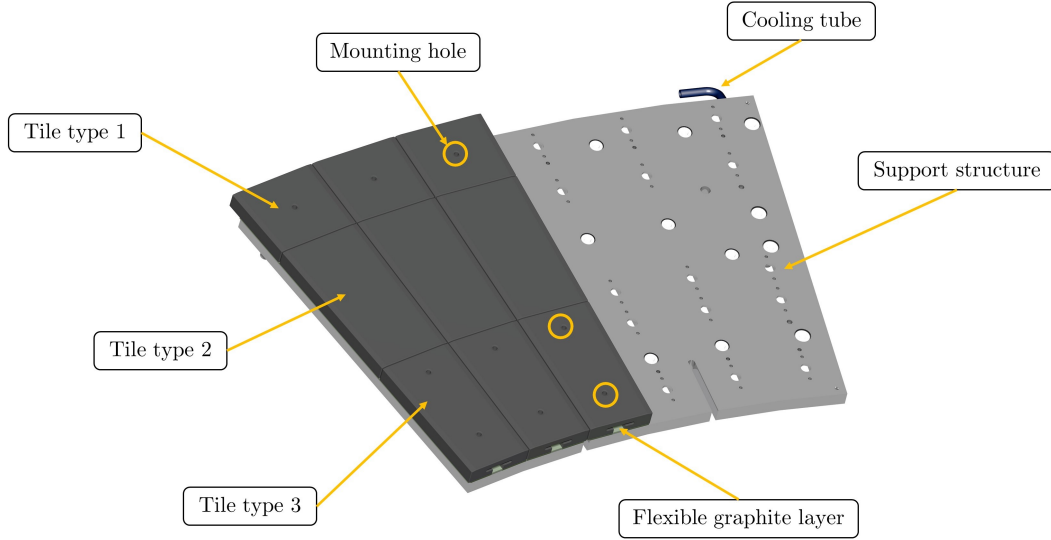


Figure 2.3: Main elements of an AUG upper outer divertor module.

The divertor targets are designed for bi-directional operation, i.e. both helicities. This allows to run experiments with a change of the magnetic configuration from lower single null to upper single null. A consequence of the bi-directional operation is that the tilted design is not applicable and a symmetric and more sophisticated shaping is needed to avoid leading edges. An ideal divertor is flat and has no gaps, but a realistic one needs gaps for thermal expansion and tolerances. Figure 2.4 shows a cross section of the targets in the toroidal direction, where the alignment in the height is $d = 1$ mm and $u = \pm 0.1$ mm. Finite element analysis were performed to optimise the measurements and a chamfer angle $\beta = 8.13^\circ$ and length $s = 7$ mm showed the best performance in the different operating modes [7].

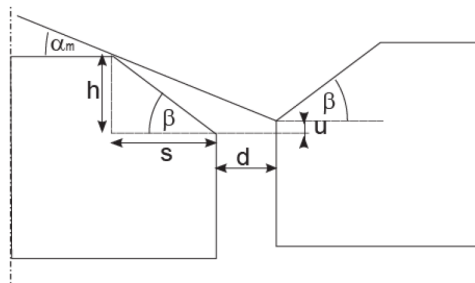


Figure 2.4: Design parameters for the toroidal gap size, where β is the chamfer angle and α_m maximum pitch angle.

2.2.2 Graphite as a plasma facing component (PFC)

In D-D or D-T plasmas high neutron fluxes are generated, which interact and degrade PFC via reduction of thermal conductivity, embrittlement, transmutation and activation. Additionally, high-heat fluxes will result in melting and cracking, meaning that the materials must also have a high thermal conductivity and a high melting point. For these reasons, beryllium (Be^4), carbon fibre composites (C^6) and tungsten (W^{74}) are considered.

Graphite presents many advantages as a PFC, such as the absence of melting, excellent thermal shock resistance and very high thermal conductivity with a low proton number. However, the use of carbon in D-T plasmas will result in the formation of tritium containing hydrocarbon deposits on the surface of the in-vessel components. This, in turn, would lead to an unacceptable tritium inventory under current licensing laws [12]. Thankfully, in AUG the only fuel used is deuterium and no tritium deposition will happen.

One characteristic of graphite as a divertor material is that at high temperatures and low pressures it can suffer from superficial sublimation and dust formation (Fig. 2.5). This can lead to higher plasma contamination and lower confinement times. For that reason, only tungsten coated graphite and full tungsten tiles are used inside AUG. However, coating can present a major issue with delamination, where the W layer separates from the substrate at high heat fluxes. G.F. Mathews and P. Coad findings in their 2009 paper [14] proved this approach may not be suitable for ITER like reactors.

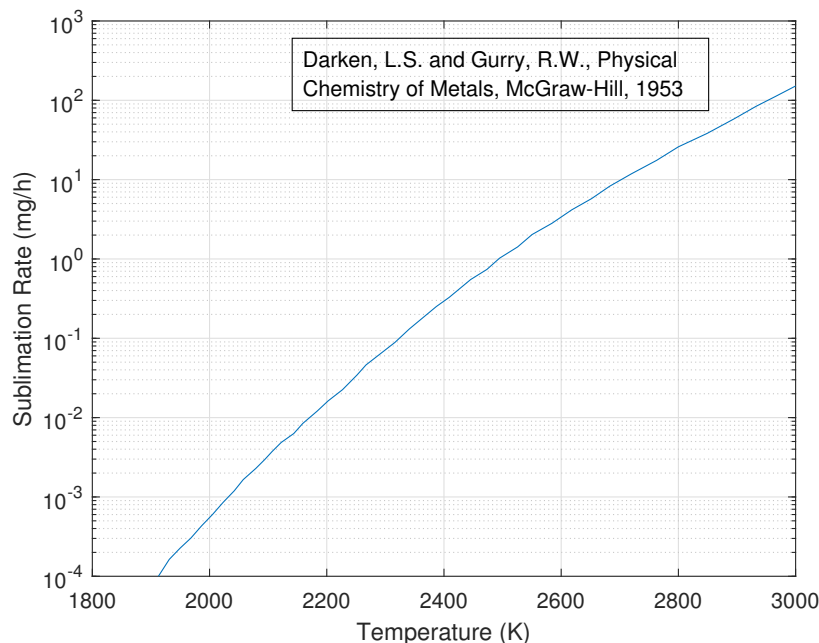


Figure 2.5: Sublimation of graphite in vacuum.

2.2.3 Tile description

Figure 2.3 shows the PFC under study in this master thesis. It is the central tile of the upper outer divertor and is located in the area with the highest thermal loading. Its approximate dimensions are 200x100x20 mm and it is distinguished from the rest by the lack of mounting holes on the plasma side. This approach to clamping avoided the inclusion of leading edges and weak points in the tile, thus increasing its durability and strength. Appendix A shows a technical drawing of the tile.

2.2.4 Installation and clamping mechanism

AUG upper divertor tiles are fixed to the cooling structure with clamping systems. These are composed mainly of a steel body, steel bolt, disk springs and a brass pin that fixes the bolt to the body. Figure 2.6, shows a cross section of the tiles where the main parts of the clamping elements can be seen. Note that a gap is left between the clamp and the graphite tile to avoid damage due to thermal expansion. Installation of the upper divertor is done by placing the tiles over a flexible graphite sheet that covers the cooling structure. Then the body of the clamp is placed in the graphite slot, followed by the bolt with the disk springs, which are inserted from the bottom of the support structure. A steel plate is screwed onto the steel structure from behind to hold the mechanism during installation. Finally, pressure is applied to align the bolt and insert the brass pin. By performing this procedure the disk springs are preloaded, pushing the tiles to the structure with a clamping pressure of 0.25 MPa. By following this approach, with a preloaded spring, the fixing is more resilient under vibration and allows for thermal expansion and a more defined contact pressure.

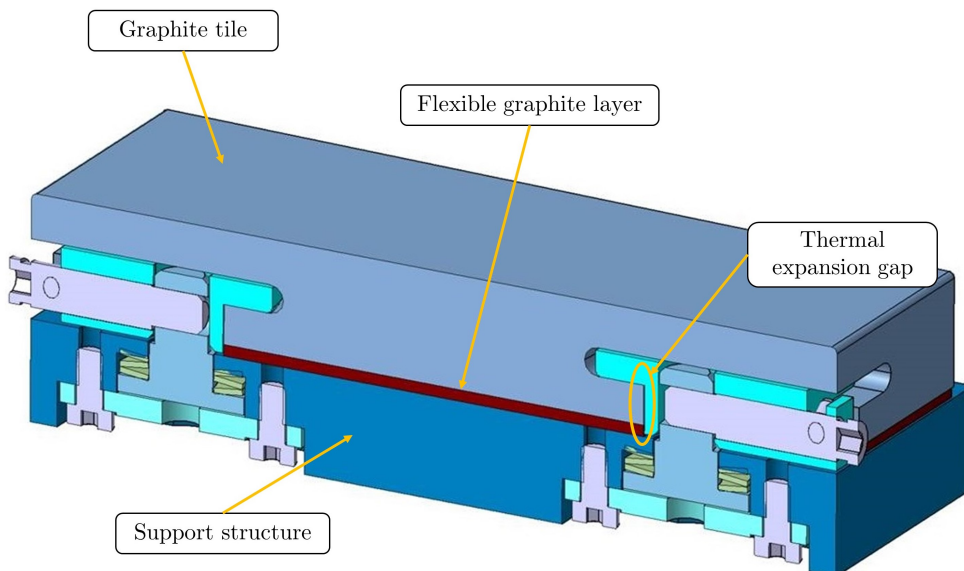


Figure 2.6: ASDEX Upgrade upper divertor cross section with installed tiles.

Figure 2.7 presents an exploded view of the original clamping mechanism with its main parts named.

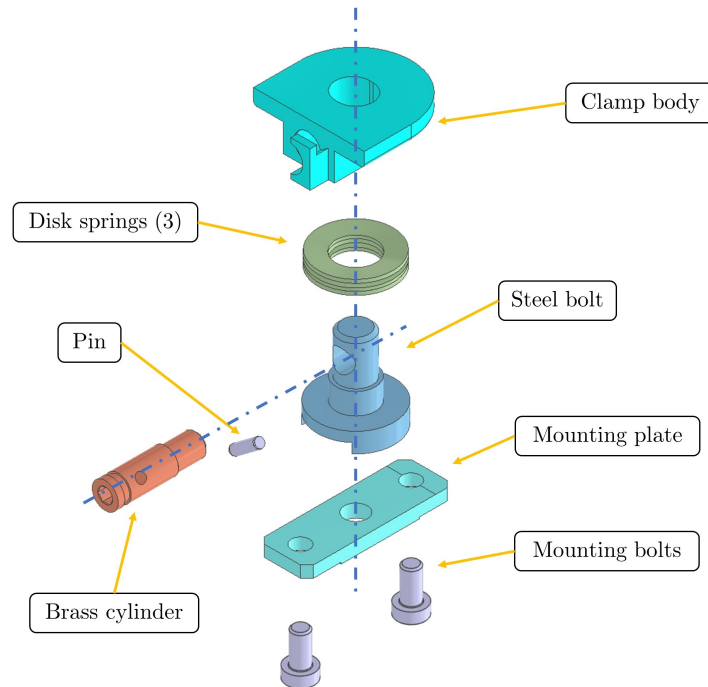


Figure 2.7: Exploded view of the clamping mechanism.

Chapter 3

Material and methods

3.1 Software

3.1.1 Finite Element Analysis (FEA)

The FEA software chosen for this project was ANSYS Workbench 2019 R3, due to its capability of easily combining thermal and structural simulations, with an user friendly interface. A transient thermal simulation with a time dependent heat source was first developed. Later, its results were combined with a static mechanical analysis, which enabled the evaluation of stresses due to thermal expansion.

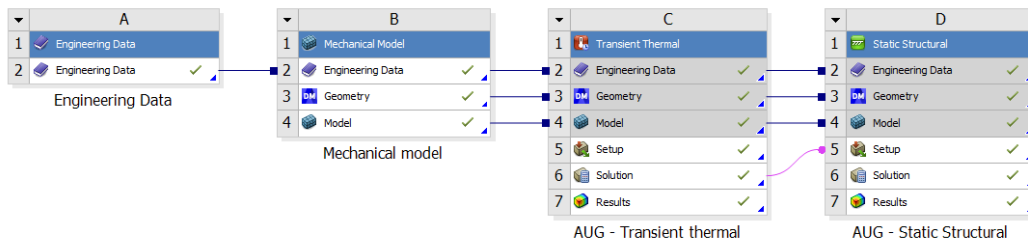


Figure 3.1: ANSYS simulation path

As shown in figure 3.1 the whole simulation is divided into 4 parts with the objective of simplifying the project update. An engineering data file was created with the gathered material information, which could be used for future projects. Following is a mechanical model where the geometry meshing is done. Finally there are the transient thermal and static structural analysis, where the temperature distribution and mechanical stresses are calculated.

3.1.2 CAD software

The prototype for the graphite tile was developed in CATIA, a cad software which has many advantages in the design of large machines. However, the model had to be simplified to reduce computational time, this was done in Inventor (Autodesk). Design modeller (ANSYS) was the final CAD software used and it allowed slicing of the geometries, which increased control over the mesh generation in ANSYS. In figure 3.2 main model feature simplifications can be seen. Support elements were joined together as a steel solid clamp and the supporting structure was simplified by defeaturing the cooling tube and fixing holes. During the meshing process it was found out that a small feature (1 %) of the tile constrained the whole geometry to be modelled with a very small element size (1 mm). Since it played an insignificant role in the thermal and mechanical simulations, it was decided to eliminate it from the model. Figure 3.3 shows the final model geometry used for the ANSYS simulations.

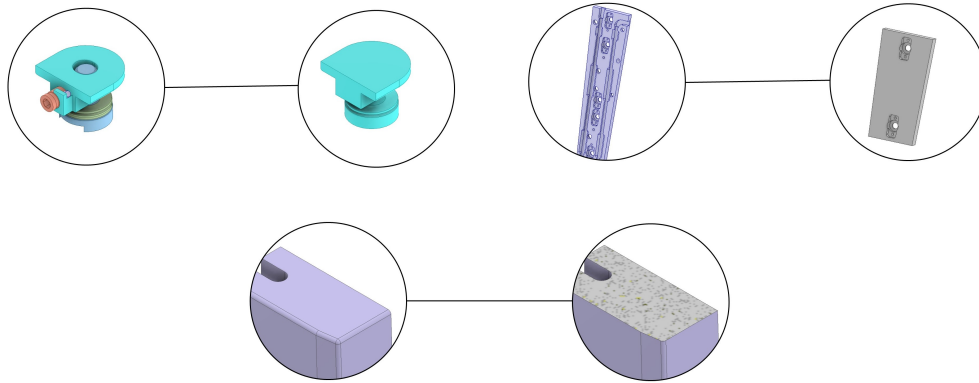


Figure 3.2: Model simplifications applied to the original CATIA design.

3.2 Material properties

In order to accurately simulate the behaviour of the upper divertor tile, material properties were added to the FEM simulation. These were taken from different sources, since manufacturer data proved to be insufficient for a precise enough simulation under large heat loads.

3.2.1 Mechanical properties of R6710 and Papyex

The graphite selected for the AUG upper divertor tile is SIGRAFINE[®] R6710 (SGL)[2]. It is a particularly strong brand of graphite, manufactured by isostatic pressing. It has a tensile yield strength of over 85 MPa, making it a good choice for applications with flexural strain and high temperature gradients. The mechanical properties of R6710 were modelled assuming isotropic elasticity, since no considerable anisotropy was noted. Additionally, the Poisson ratio was included according to Manhani and Borzani [13].

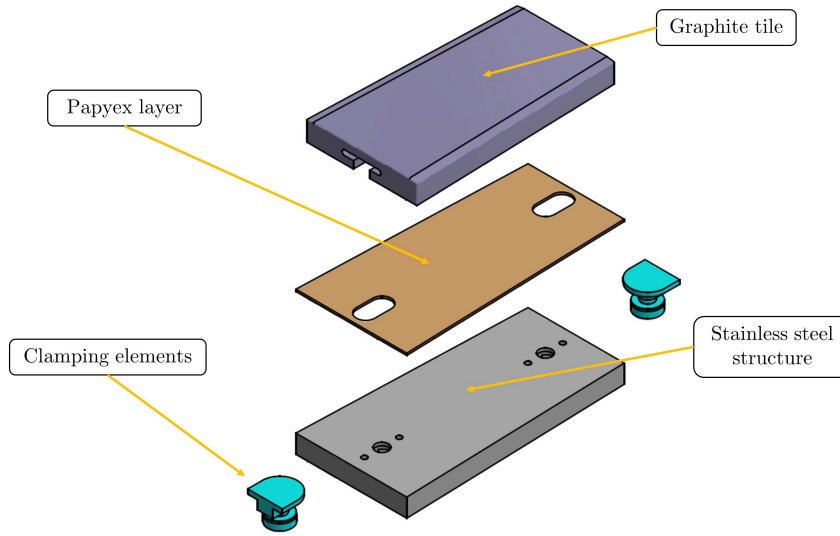


Figure 3.3: Final 3D model for FEA with simplifications.

A sheet of Papyex[®] N998 (Mersen) [15] graded for nuclear applications is used as an interlayer between the graphite tile and the steel structure. This material is produced by compression of graphite flakes, without the need of additional binders. It remains solid only by the inner friction forces generated during pressing. Due to the nature of their lattice, flexible graphite materials present high anisotropy, having high thermal conductivity in the direction of compression. Its mechanical properties were studied by Khelifa M. in 2018 [11] and they were added to the current work.

Table 3.1: Mechanical properties of graphite materials at room temperature.

Material	Property	Expression	Value	Unit
R6710	Young modulus	E	210	GPa
	Poisson ratio	τ	0.187	-
	Tensile yield	S_t	85	MPa
	Compressive yield	S_c	170	MPa
	Density	ρ	1.88	g/cm ³
Papyex	Young modulus	E	190	MPa
	Poisson ratio	τ	0.3	-
	Tensile yield	S_t	1.9	MPa
	Compressive yield	S_c	186	MPa
	Density	ρ	1.0	g/cm ³

Graphite R6710 has a notable property of becoming stronger with an increasing temperature according to material data on table 3.2. Room temperature tensile yield is measured at 85 MPa, whilst the maximum is found at 2800K at 169 MPa.

Table 3.2: Yield of graphite R6710 variation with temperature.

T (K)	S _t (Mpa)	T (K)	S _t (Mpa)	T (K)	S _t (Mpa)
293	85	1250	93.5	2250	116.8
500	87.3	1500	97.5	2500	137.9
750	88.5	1750	101.7	2750	168
1000	90.4	2000	107.1	3000	157.1

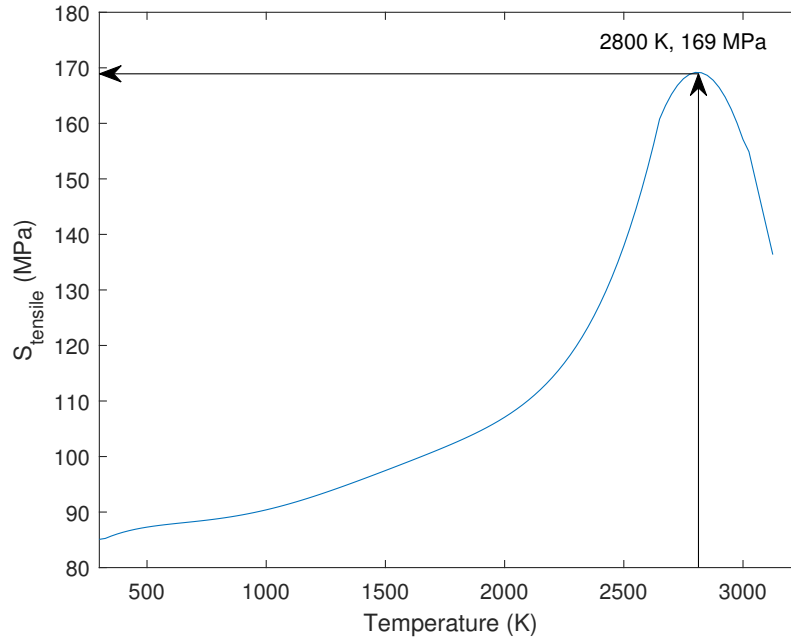


Figure 3.4: Yield of R6710 variation with temperature.

3.2.2 Failure criteria

Graphite materials are not ductile due to the lack of plastic deformation prior to failure. However, large elastic deformation can be observed in materials like R6710. A new type of fracture has been defined for such materials: quasi-brittle. This category, which includes many polycrystalline ceramics, shows considerable deformation prior to failure that is not associated with dislocation motion. Experience with graphite materials has shown that the critical point is reached with the maximum temperature gradient. Thus this is the temperature at which the simulations will be performed. The tensile limit will be modified according to temperature on critical points to adapt the safety factor during the simulation results assessment. As an example, during a 10 MW/m² for 3.5s simulation maximum principal stress reached 73 MPa in a location where the temperature was 480K. In that case, the yield is updated to 87.2 MPa, making the evaluation less conservative. Non-elastic analyses were not considered.

Brittle material failure theory will be used to determine safety factor of the graphite tile. Specifically, Mohr-Coulomb and maximum principal stress safety factors will be presented. This is in accordance with design criteria for nuclear graphite components provided by the Japan Atomic Energy Research Institute (JAERI) [9].

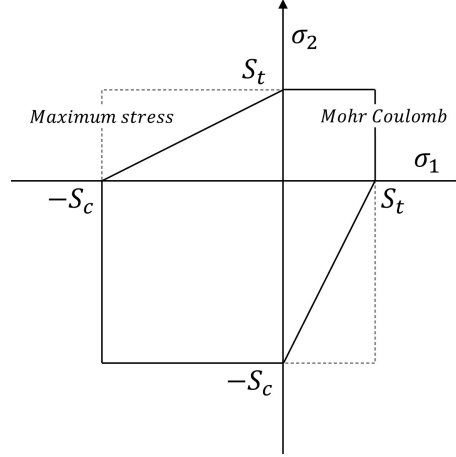


Figure 3.5: Mohr Coulomb and maximum stress criterion for 2D stress, where σ_1 and σ_2 are the two principal stresses and S_t and S_c are the tensile and compression limits, respectively.

Equation 3.1 shows the calculation method for the safety factor (SF) according to 3D stresses, which is the equation used in ANSYS Workbench.

$$F_s = \left[\frac{\sigma_1}{S_{tensile.limit}} + \frac{\sigma_3}{S_{compressive.limit}} \right]^{-1} \quad (3.1)$$

where $\sigma_1 > \sigma_2 > \sigma_3$ and σ_3 and the compressive strength limit are assumed to be negative values.

3.2.3 Thermal properties of R6710 and Papyex

Thermal characteristics of R6710 were modelled as non-linear isotropic temperature-dependant properties, whereas for Papyex they are anisotropic temperature independent. Specific heat (Fig. 3.6) follows the recommended values by the ASTM standard C781 [8] for nuclear reactor components. It is considered equal in both graphite components due to their purity. In table 3.3 room temperature values are given. Emissivity [17] is included to model radiation from the tile. Thermal expansion (Fig. 3.8) and conductance (Fig. 3.7) are obtained through interpolation of given values.

Thermal expansion of graphite R6710 is given only in the range of 20-200 °C, the graph shown in 3.8 is obtained by interpolation of a given curve from the same manufacturer. Papyex is considered to only have expansion in the direction of the thickness, with a constant value of $28 \cdot 10^{-6} C^{-1}$

Table 3.3: Thermal properties of graphite components at room temperature.

Material	Property	Expression	Value	Unit
R6710	Expansion	e	4.7 E-6	C ⁻¹
	Conductivity	λ	110	W/m·C
	Emissivity	ϵ	0.75	-
Papyex	Planar expansion	e_p	0	C ⁻¹
	Thickness expansion	e_t	28 E-6	C ⁻¹
	Planar conductivity	λ_p	11.5	W/m·C
	Thickness conductivity	λ_t	150	W/m·C
Graphite	Specific heat	C_p	700	J/kg·K

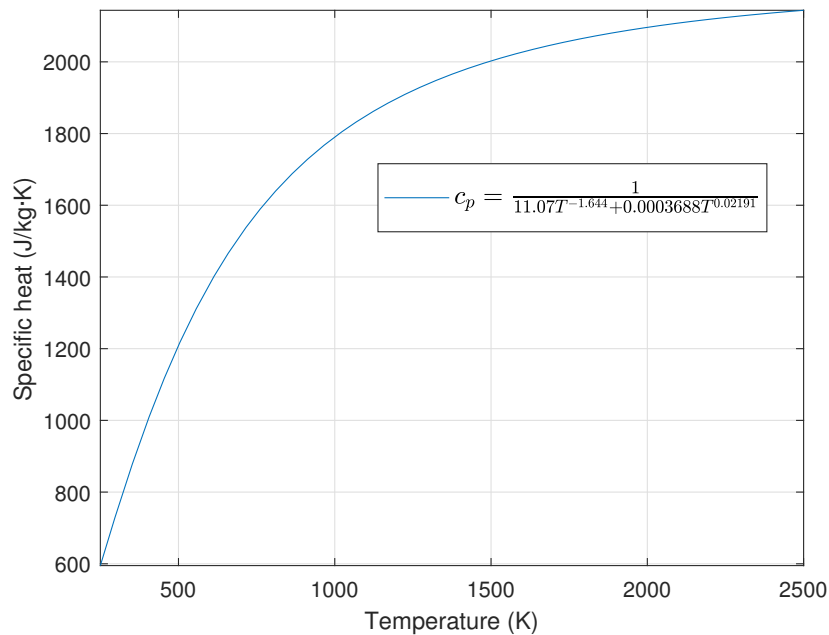


Figure 3.6: Specific heat of graphite components according to ASTM standard practice for testing graphite and boronated graphite materials for high-temperature gas-cooled nuclear reactor components (C781).

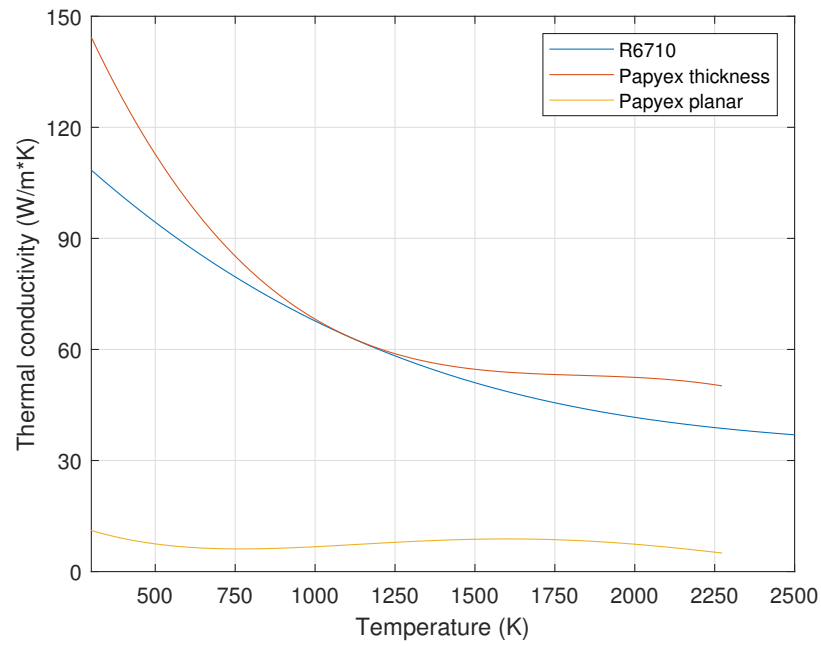


Figure 3.7: Thermal conductivity of graphite components.

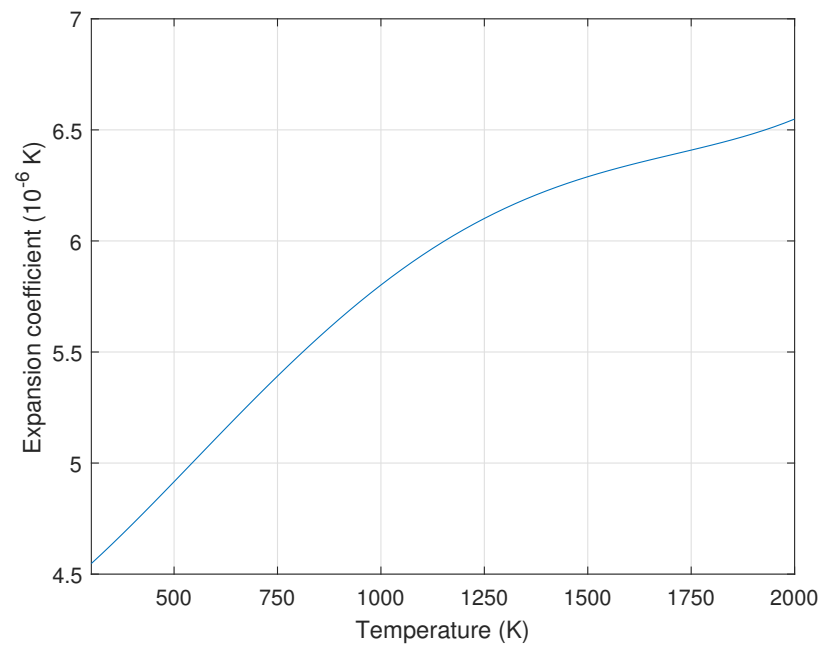


Figure 3.8: Thermal expansion of graphite R6710.

3.2.4 Stainless steel

316L(N)-IG steel is selected for the supporting structures according to ITER's structural design criteria [1]. Main material properties are included in the simulation model. This austenitic steel is used for unirradiated applications, with an operating temperature between 20°C and 500°C. Clamp material is 304LN steel, which has also been characterized. Since their properties are fairly similar, both steels are assigned the same thermal and mechanical properties. Therefore, they will be grouped in a material named Steel ITER, whose properties are shown in table 3.4.

Table 3.4: Mechanical and thermal properties of 316L(N)-IG and 304LN steels, characterized according to ITER at room temperature.

Property	Expression	Value	Unit
Young modulus	E	200	GPa
Poisson ratio	τ	0.3	-
Tensile yield	S_y	180	MPa
Density	ρ	7930	kg/m ³
Thermal expansion	e	0.3	K ⁻¹
Thermal conductivity	λ	14.28	W/m·K
Specific heat	C_p	472	J/kg·K

3.3 Simulation

3.3.1 Meshing

Simulation time and skewness were the two main objectives optimized during the meshing process. To minimize the element count, a hexahedral element shape was chosen for the whole geometry. Skewness is defined as the difference between an element's shape and another with same volume, but with equilateral vertices. This metric was kept under 0.84, with an 80 % of the model being under 0.05.

The low skewness factor proved a high quality mesh and eliminated the need of quadratic elements, reducing the nodal count and hence simulation time. Figure 3.9 presents the difference between linear and quadratic hexahedral elements, which have 8 nodes instead of 20.

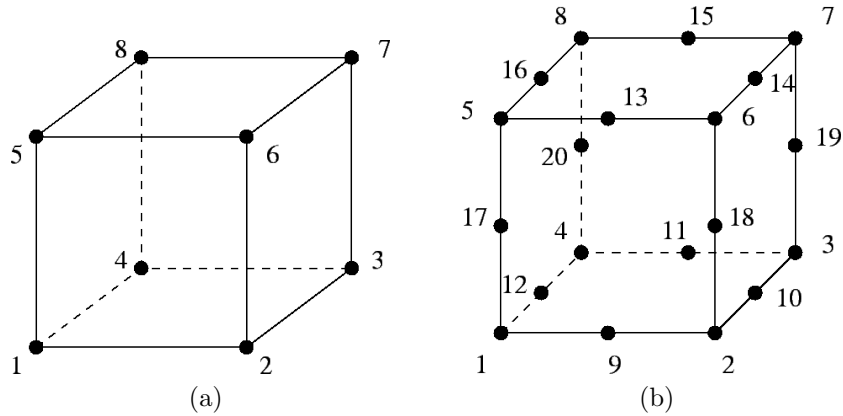


Figure 3.9: (a) Hexahedral linear element. (b) Hexahedral quadratic element.

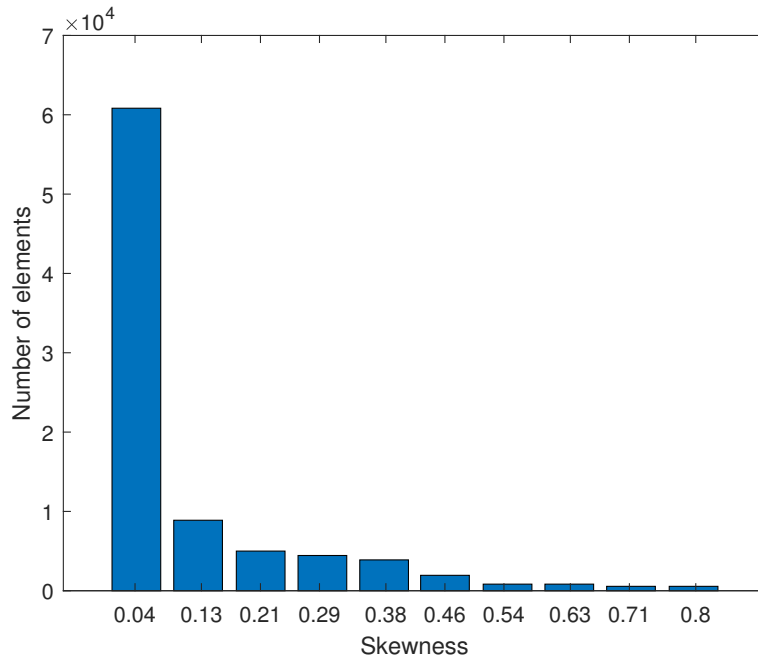


Figure 3.10: Skewness bar plot of the generated mesh.

Generation of a high quality mesh in ANSYS workbench requires for a very precise control over it. In order to achieve that the 5 body model was sliced into 35 with design modeller. These were grouped and meshed in a 13 step meshing worksheet. In the end, the resulting mesh had 105283 nodes and 85904 elements. The meshed mechanical model is shown in figure 3.11, where different colours indicate different bodies. After the first thermomechanical simulation was done a convergence study was performed, indicating a non-singularity point, but a stress concentrator, around the clamping region. Figure 3.12 presents the results of this study with the abscissa containing the element count in the round edge of the clamping slot in the tile.

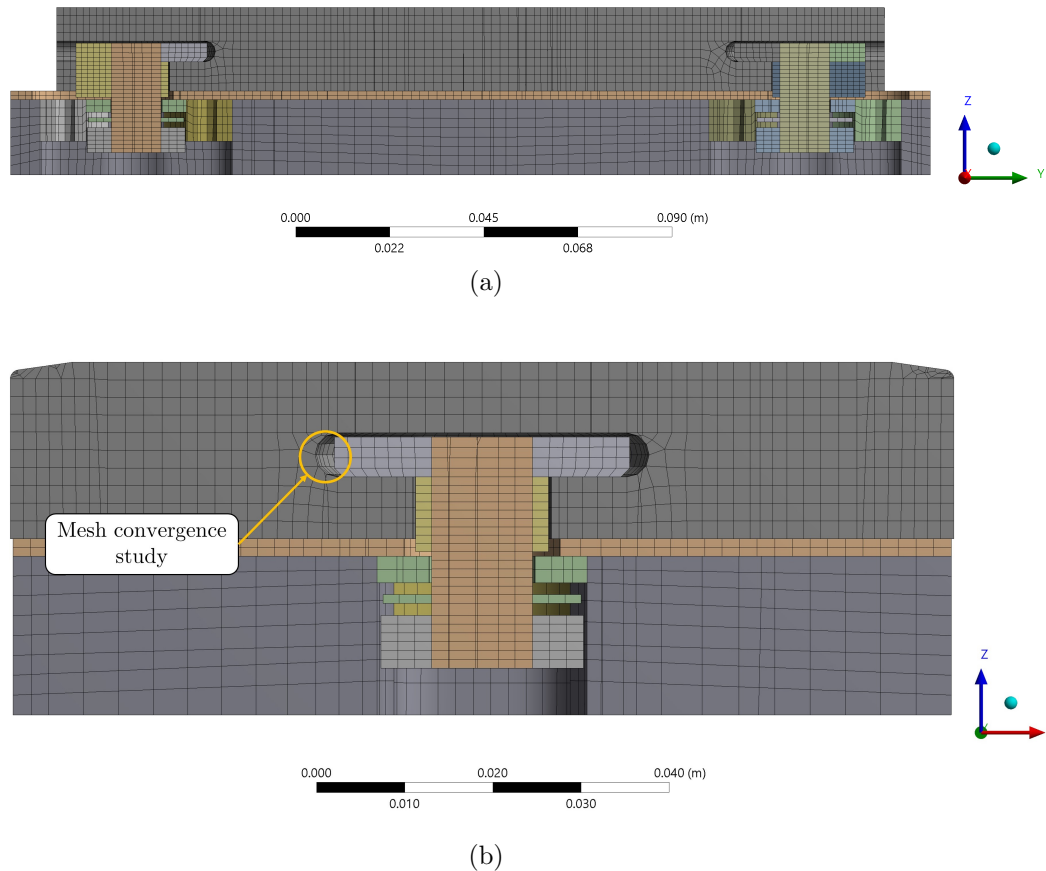


Figure 3.11: (a) Meshing poloidal direction. (b) Meshing toroidal direction.

3.3.2 Contact behaviour

There are a total of 4 contact surfaces defined in the ANSYS model (Table 3.5). These have been modelled as frictional type contacts with augmented Lagrange formulation. The friction coefficient between R6710 and Papyex has been defined as 0.8, according to FP Bowden and JE Young findings on friction behaviour between carbon based materials under vacuum. For graphite materials and steel, a common value for vacuum conditions has been used. Heat transfer coefficients between materials are defined according to previous works regarding their dependence with contact pressure from B. Streibl [16].

Frictional contacts, unlike bonded, have the characteristic of modelling gaps between contacting surfaces if the normal pressure is equal to zero. In addition to that, shear stress are calculated as a fraction of the normal pressure and they are transmitted up to a certain value. Once the limit is reached, the geometries slide relative to each other.

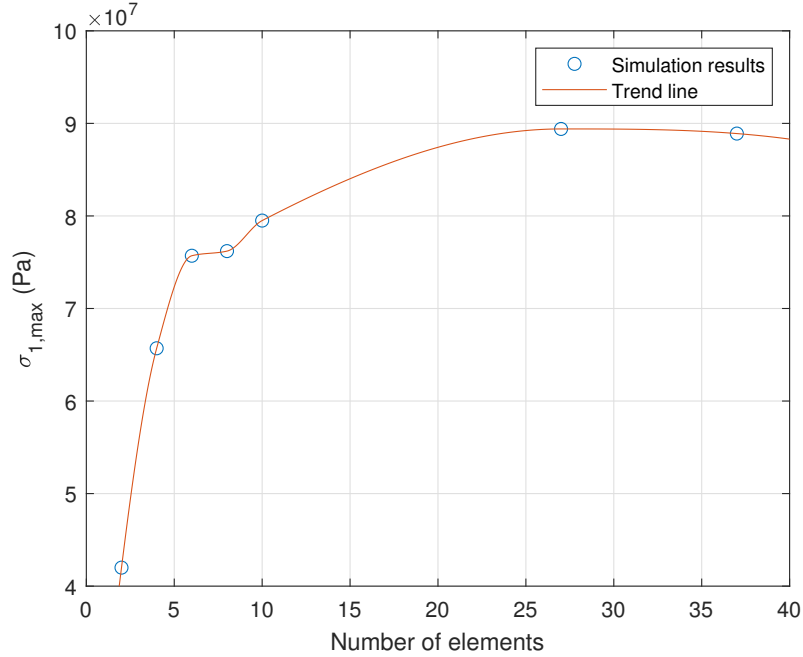


Figure 3.12: Mesh convergence around stress concentrator.

Augmented Lagrange is a non-linear solid body contact penalty-based formulation. According to equation 3.2, where F_n is a finite contact force in the normal direction, k_n is a contact stiffness factor, x_p is the penetrated distance and λ is an extra term that reduces the sensitivity of the formulation to the stiffness factor.

$$F_n = k_n \cdot x_p + \lambda \quad (3.2)$$

Asymmetric behaviour has the characteristic of only calculating values for the contact. Therefore, for the clamping region R6710 will be chosen as the contact. For graphite and Papyex contact region, tile surface is chosen as target because Papyex is a softer material. Therefore, small penetration of the tile into the interlayer will be allowed. Stainless steel structure and Papyex contact region is also defined as asymmetric, and steel is assigned target since it is harder than the other material.

Table 3.5: Contact behaviour defined on the simulation.

Contact	Target	Friction coefficient	Heat transfer coefficient (W/m ² K)
R6710	Clamp 1	0.21	56
R6710	Clamp 2	0.21	56
Papyex	R6710	0.8	105
Papyex	Steel	0.21	105

3.3.3 Thermal simulation

AUG divertor tile has been simulated under various types of heat loads in the search of unsymmetries or errors during calculation. Firstly, a steady state thermal model with Neumann boundary conditions in all of the open surfaces was used. This simulation had a homogeneous stationary 1 MW/m^2 heat load applied to the upper layer of the graphite tile, whilst the back part of the steel structure was assigned forced convection, the rest had adiabatic conditions. The results provided information on the temperature gradient and temperature and heat flux drops in contact surfaces. After inspection the model was modified into the second phase, transient thermal simulations, whose results were coupled with static mechanical analysis. Finally, the current simulation model was chosen and adapted during the experimental phase.

An initial temperature of $22 \text{ }^\circ\text{C}$ is set for all of the bodies at the beginning of the simulation. After 1 second of preload time, a 2-D Gaussian heat distribution (Eq. 3.3) is applied on the upper surface of the tile according equation 3.3. Figure 3.13 represents the profile on the tile according to a typical AUG plasma flux.

$$f(x, y) = Ae^{-\left(\frac{(x-x_0)^2}{2\sigma_x^2} + \frac{(y-y_0)^2}{2\sigma_y^2}\right)} \quad (3.3)$$

Where

- A = Peak heat flux.
- x_0, y_0 = Centre coordinates.
- σ_x^2 = Variance in the toroidal direction.
- σ_y^2 = Variance in the poloidal direction.

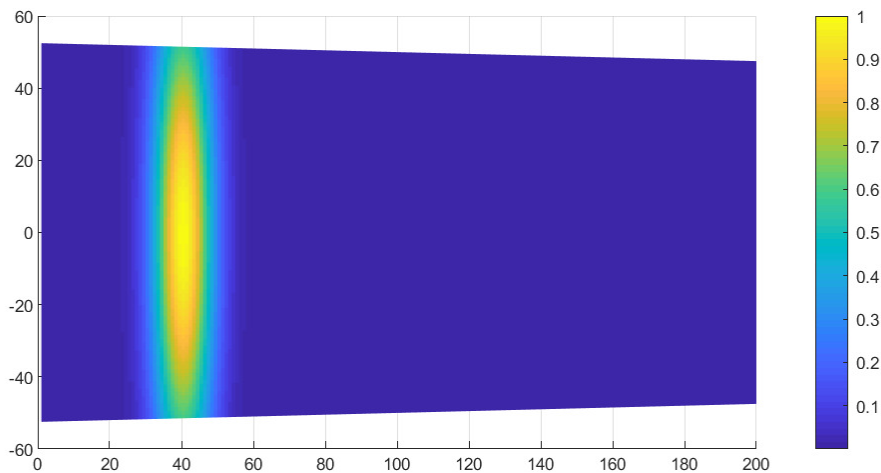


Figure 3.13: Normalized AUG heat distribution with $[\sigma_x, \sigma_y] = [50, 6]$ mm and centre at 40 mm.

3.3.4 Mechanical simulation

Thermomechanical simulation of the AUG upper divertor is performed as a static analysis divided in two steps. The first one is the clamping phase, where a displacement is applied on the base of the clamping elements, simulating the spring behaviour of the mechanism. Figure 3.14 presents this loading phase, where a maximum contact pressure of 0.255 MPa can be seen.

As mentioned before, contact behaviour is defined as frictional, meaning that shear stresses between contacting surfaces can be carried. These forces stick the model together as one structure, since only the side surfaces of the support structure body are fixed. By dividing the simulation in two steps, convergence is reached much faster, since expansion is simulated on an already joined model. Clamping of the tile is done by creating a displacement on the base of the clamping elements. This simulates the preloaded spring behaviour, while allowing thermal expansion of the tile, without over constraining the model.

Temperature results from the transient thermal simulations are coupled with the second phase of the static mechanical analysis to calculate the strain caused during operation. In particular, the peak temperature gradient is chosen as the point of reference for the maximum stresses and hence, the critical point of operation. Plastic behaviour of graphite R6710 is not considered, due to the brittle nature of graphite. Therefore, stresses must be limited to the temperature dependant elastic strength limit according to figure 3.4. All in all, this means that failure must be assessed on a case-per-case basis, since ANSYS workbench does not include a safety factor calculation with a non-linear strength limit.

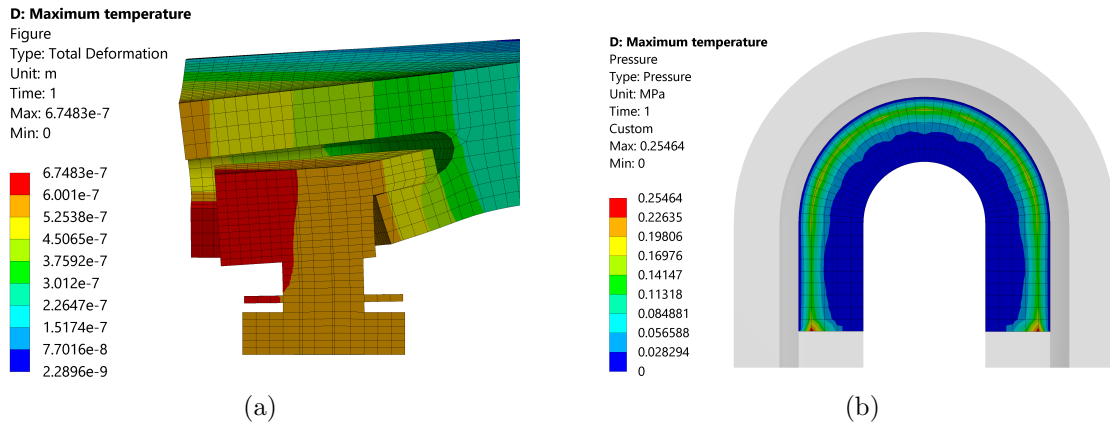


Figure 3.14: (a) Deformed graphite tile during preload ($\times 1.7 \cdot 10^4$ amplification factor). (b) Contact pressure on clamping region during preload.

3.4 GLADIS experimental campaign

3.4.1 Garching Large Divertor Sample (GLADIS) test facility

The Garching Large Divertor Sample (GLADIS) shown in figure 3.15 is an ion beam test facility equipped with two independent 1.1 MW sources. It is capable of reproducing steady state high heat fluxes (HHF) to test actively cooled plasma facing components. Each source can generate loads between 3 and 55 MW/m² with a FWHM of 70 mm. The facility is designed to be able to test full scale ITER divertor targets and in this work it will be used to test the new AUG upper divertor tiles [4].



Figure 3.15: View of the GLADIS test chamber.

3.4.2 Campaign definition

Model validation has been performed in the GLADIS test facility. Four types of tests were done, with two power inputs and two peak locations. Test identification number, peak power, location of the peak, applied time, resulting power and energy on the tile are presented in table 3.6. The two last parameters refer to heat absorbed by the tile, which has been calculated with a Matlab code shown in Appendix B. This code is able to integrate bivariate Gaussian distributions in a trapezoidal geometry. The proposed tests follow the campaign of high heat flux tests and structural analysis done for the solid tungsten divertor in 2015 [10]. Twenty cycles per each type were performed, with a cool down time of 3 minutes between cycles. Duration of experiment was 4 hours, without taking into account set-up time and an accumulated 3 minutes of exposure time.

GLADIS heat source is described in figure 3.16, where y is the poloidal symmetry axis. Appendix A contains a technical drawing with sensor placement and beam locations.

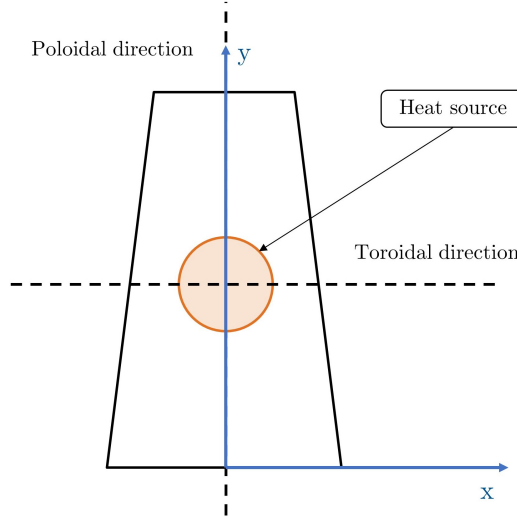


Figure 3.16: Heat source axis information for GLADIS experiments.

Equation 3.4 presents the heat source parameters of GLADIS, which corresponds to a univariate Gaussian distribution. The beam is described only by one axis because it is radially symmetric.

$$q = q_0 + \frac{A}{w \cdot \sqrt{\frac{\pi}{2}}} e^{-\frac{2(x-x_0)^2}{w^2}} \quad [\text{MW}/\text{m}^2] \quad (3.4)$$

Where

- q_0 = Baseline value.
- A = Total area between curve and baseline.
- x_0 = Peak centre coordinates.
- w = 2σ (σ , standard deviation).

Translating 1-D Gaussian data of GLADIS to the 2-D distribution used in ANSYS Workbench was difficult, particularly for high heat fluxes. To obtain the variance values for the bivariate distribution, an iterative process was performed. Figure 3.17 presents the Gaussian fit of 6 heat flux distributions measured at the GLADIS facility. Note the narrowing of the distribution with the increasing peak power.

Table 3.6: Parameters of the bivariate Gaussian distribution heat source applied on the graphite tile for the GLADIS tests.

Id	Peak power MW/m ²	σ_x, σ_y mm	Peak location mm	Time s	Power kW	Deposited energy kJ
1	10	[61, 61]	100	3.5	123.5	432.1
2			40		102.6	359.2
3	25	[55, 55]	100	1	281.6	281.6
4			40		233.8	233.8

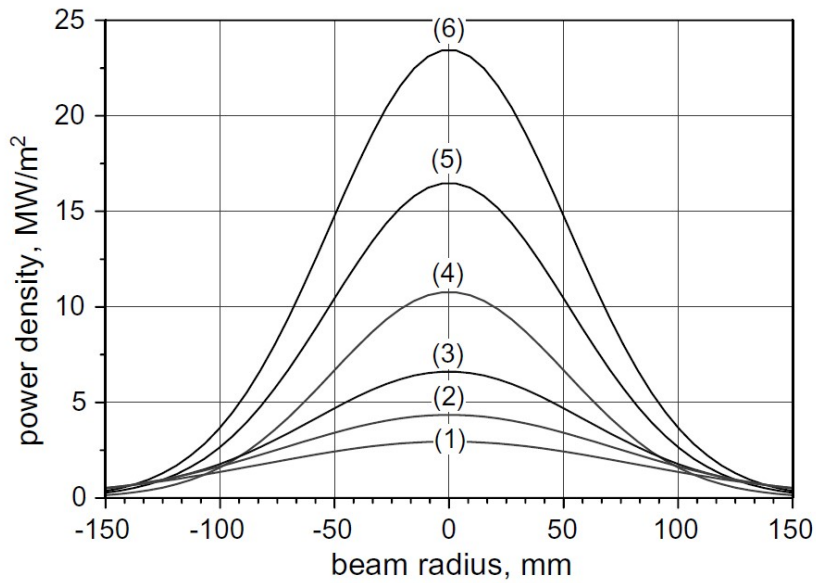
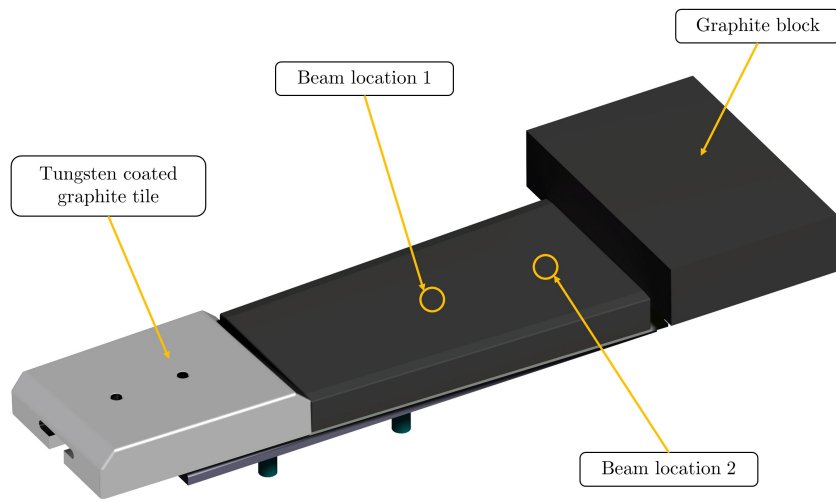


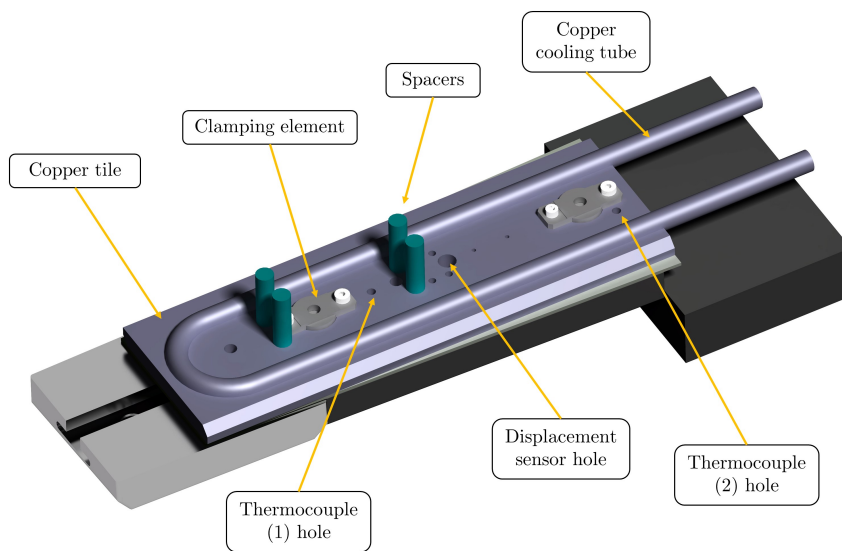
Figure 3.17: Gaussian fits and measured beam profiles for 6 distributions of: 130 kW (1), 155 kW (2), 182 kW (3), 252 kW (4), 353 kW (5) and 560 kW (6). H. Greuner [4].

3.4.3 Experimental setup

Figure 3.18 presents the upper and lower sides of the GLADIS experimental setup. Two elements are used to protect the copper elements from the ion flux: a tungsten coated graphite tile and a graphite block. A cooling tube is used to extract heat from the experiment. Spacers are used to move the whole setup. Figure 3.18a shows the two beam locations used and 3.18b has the perforations for the sensors.



(a)



(b)

Figure 3.18: Experimental setup (a) upper side (b) lower side.

A total of 5 sensors were placed on the back side of the tile to measure temperature and displacement during pulses, they can be seen on figure 3.19. Thermocouples (1) and (2) were spring loaded to maintain contact with graphite, while (3) and (4) were drilled into the clamping elements and glued with graphite adhesive. Additionally, infrared thermography provided surface temperature values. A potentiometric linear transducer model MM1012 from MEGATRON was used as a displacement sensor.

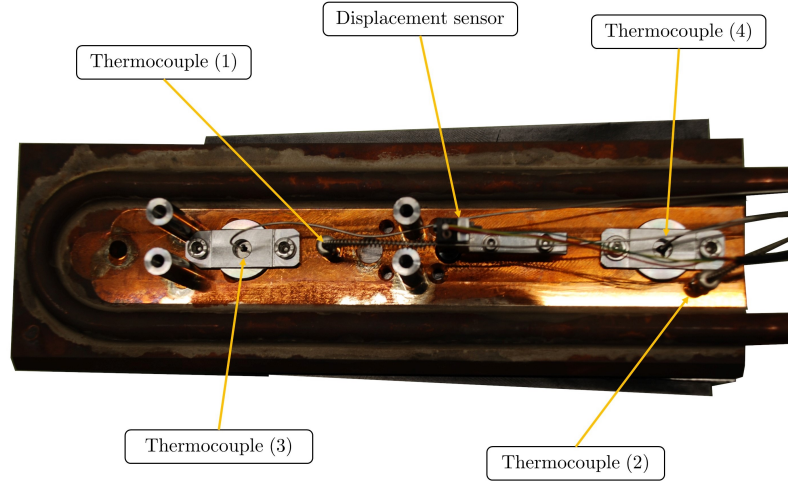


Figure 3.19: Sensor location of test tile for GLADIS experiment.

3.5 AUG upper divertor simulation

Two cases have been selected for simulation and analysis as shown in table 3.7. These correspond to the typical heat loads used as design criteria for the lower divertor, meaning they represent typical loading cases for the upper divertor in a single null configuration [6]. 1 - AUG has a peak power of 15 MW/m^2 and a duration of 3 s, comparing this to 2 - AUG, a higher temperature gradient will be obtained. However, larger deposited energy will result in larger overall temperatures and therefore more thermal expansion.

Table 3.7: Parameters of the Gaussian distribution applied to the graphite tile during AUG plasma.

Id	Peak power MW/m^2	σ_x, σ_y mm	Peak location mm	Duration s	Power kW	Deposited energy kJ
1 - AUG	15	[50, 6]	40	3	19.7	59.1
2 - AUG	7	[50, 10]		10	15.3	153.3

Chapter 4

Results

4.1 GLADIS experimental campaign

In this section results from the experiments performed at the GLADIS testing facility are presented. As explained before, 4 experimental setups were designed from which 30s of each pulse were recorded. Little variation was seen during the experiment, meaning high precision and low variation in the results are expected. For that reason, average thermal results will be presented in this chapter.

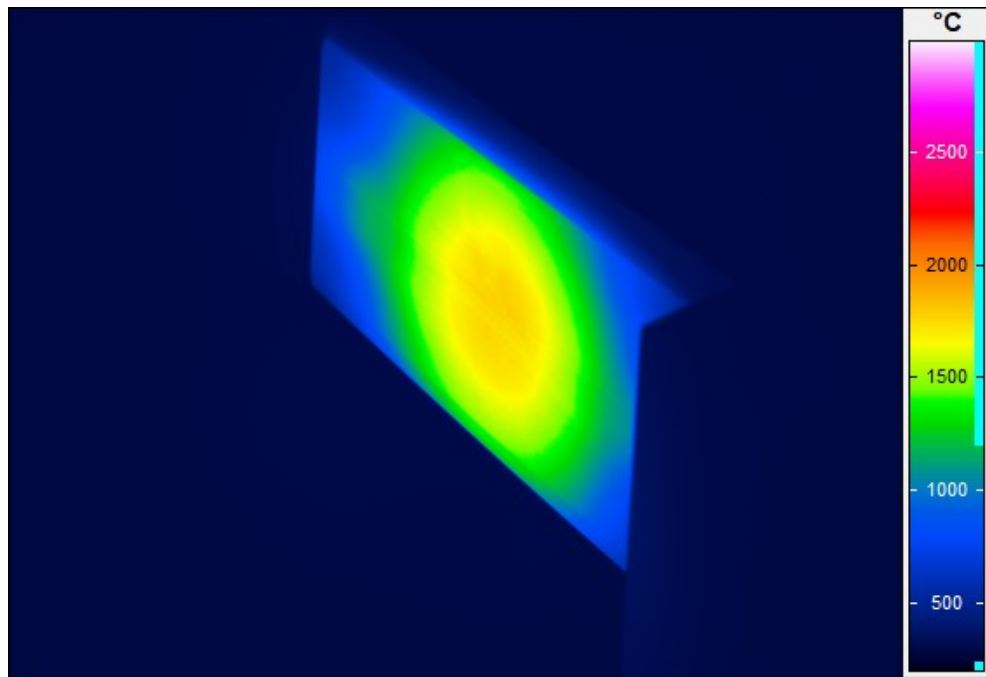
4.1.1 Infrared imaging and surface temperature

Table 4.1 presents the measured beam power and surface temperature according to each location and peak power. Beam power (kW) corresponds to the calculated electrical power obtained by the multiplication of the current and voltage measured on the ion sources. The surface temperature is measured through pyrometers located at the centre of the heat source.

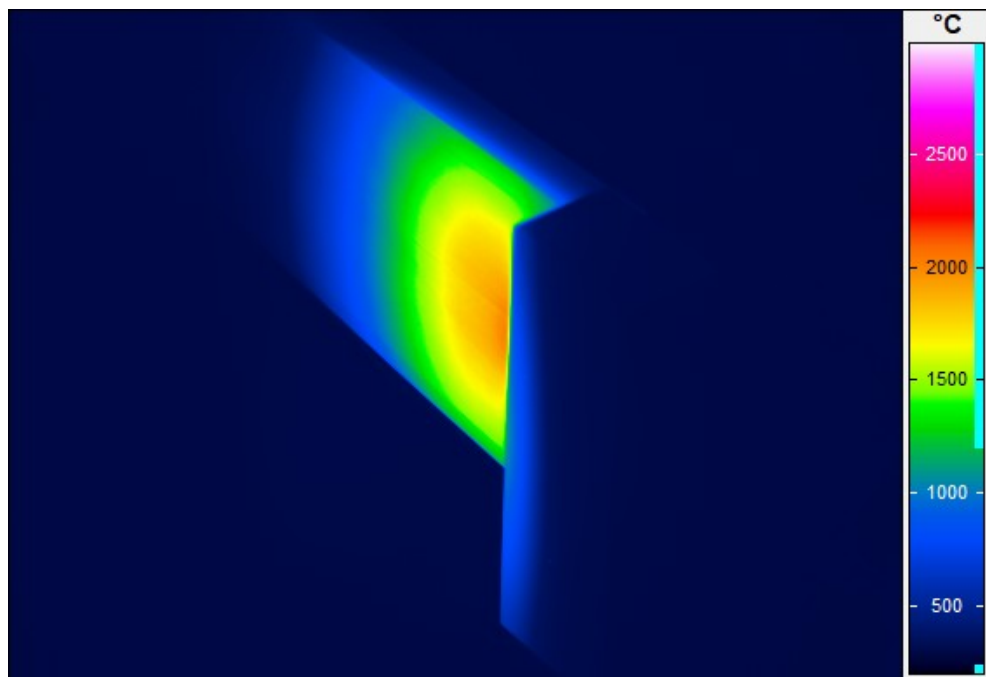
Table 4.1: Beam characteristics and maximum surface temperature results from GLADIS tests.

Id	Peak power MW/m ²	σ_x, σ_y mm	Peak location mm	Time s	Beam power kW	T _{surf,max} °C
1	10	[61, 61]	100	3.59	274.21	1796.1
2			40		273.85	1933
3	25	[55, 55]	100	1.08	733.08	2398.16
4			40		738.13	2472.4

Figures 4.1a and 4.1b show the IR thermography images taken during the experiments. Note the graphite block obstructing the view of the temperature distribution for fluxes focused on the clamping region.

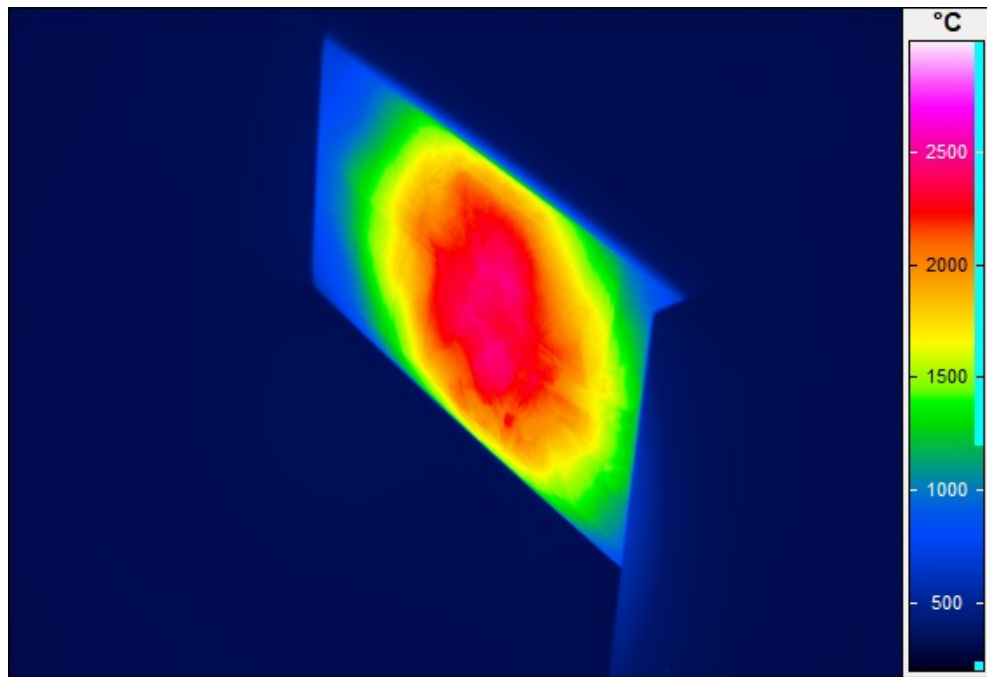


(a)

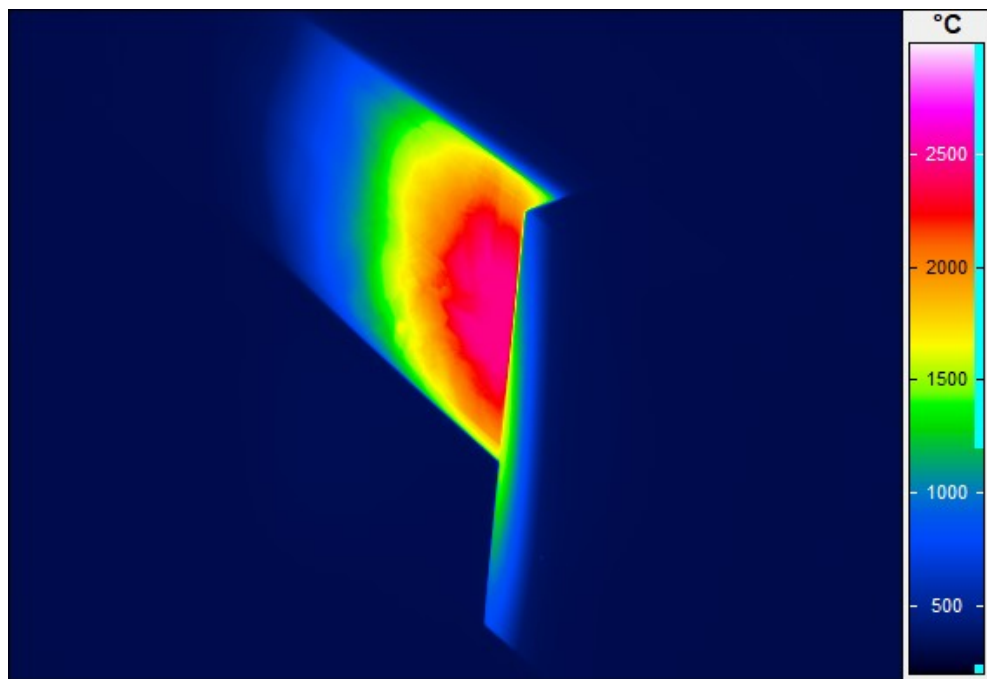


(b)

Figure 4.1: Maximum surface temperatures of the 10 MW/m² tests with (a) centred beam and (b) beam focused on the clamping region.



(a)



(b)

Figure 4.2: Maximum surface temperatures of the 25 MW/m^2 tests with (a) centred beam and (b) beam focused on the clamping region.

4.1.2 Thermocouple data

During the experiment temperature was measured through thermocouples on the rear side of the tile and inside the clamps, as shown in chapter 3. Table 4.2 contains initial and maximum temperatures measured on these sensors. Figure 4.3 shows the variation of the initial temperature throughout the experimental campaign according to thermocouples 3 and 4. Temperature evolution shows insufficient cooling for most tests since stationary temperature of 20°C was not reached. Negative values on the test number indicate set-up pulses.

Table 4.2: Measured temperature on thermocouples attached to the graphite tile (1, 2) and inserted on the clamps (3, 4).

Id	$T_{1,start}$ (°C)	$T_{1,max}$ (°C)	$T_{2,start}$ (°C)	$T_{2,max}$ (°C)	$T_{3,start}$ (°C)	$T_{4,start}$ (°C)
1	21.6	414.7	23.3	204.4	61.2	66.1
2	22.3	178.9	27.3	374.6	38.6	103.8
3	21.9	306.3	20.8	163.7	52.6	57.9
4	19.3	140.4	20.9	293.8	30.9	75.0

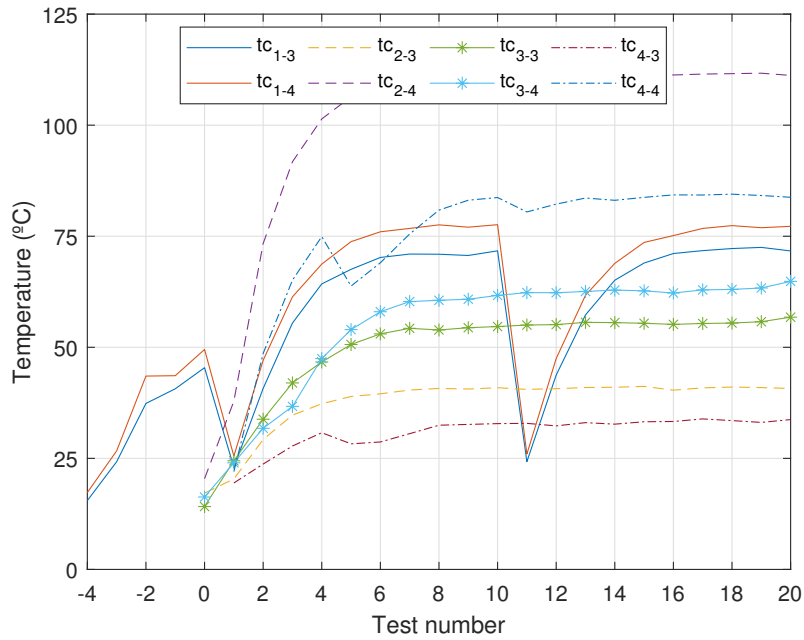


Figure 4.3: Temperature at the beginning of the pulse on thermocouples inserted in the clamps.

In addition to the previous table, figure 4.4a shows the temperature evolution for the 10 MW/m² tests and figure 4.4b of the 25 MW/m² according to sensors 1 and 2 and pyrometers.

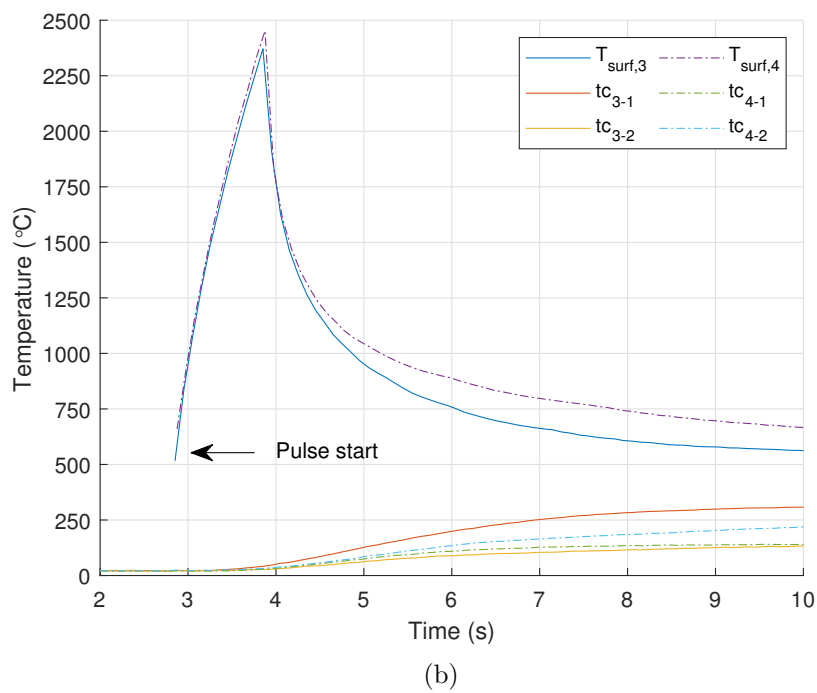
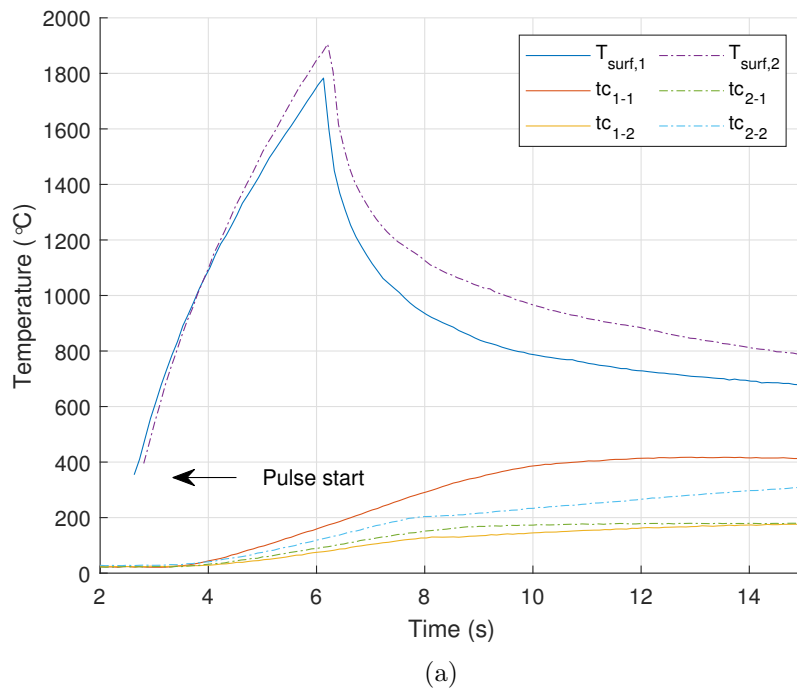


Figure 4.4: (a) Transient data from 10 MW/m² experiments #248575 and #248596. (b) Transient data from 25 MW/m² experiments #248647 and #248667

4.1.3 Mechanical results and inspection

As expected from the material research, graphite R6710 did not present plastic deformation. However, noticeable elastic deformation was shown in the camera and measured in the displacement sensor. Table 4.3 contains the measured data and in figure 4.6 pre exposure and peak test deformation are shown.

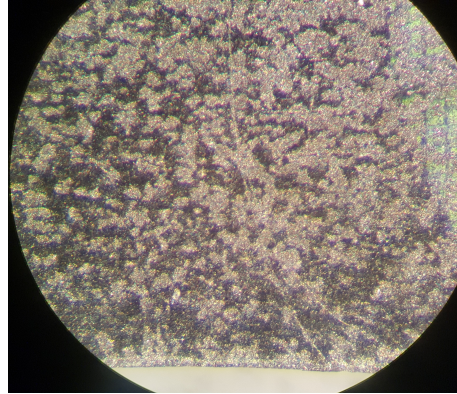
Table 4.3: Displacement measured on the tile during pulses.

Id	δ_{MIN} (mm)	δ_{AVG} (mm)	δ_{MAX} (mm)
1	1.03	1.04	1.05
2	0.62	0.63	0.65
3	1.27	1.39	1.45
4	0.83	0.87	0.91

After the tests the tile was unmounted and an inspection was performed under microscope in search of microfractures, but none were found. Only remarkable results were the presence of graphite dust from grinding between the clamps and the tile on the clamping regions. Additionally, graphite sublimation was observed (Fig. 4.5b), which according to figure 2.5 had a maximum rate of 20 mg/h. This sublimation area was not observed in the whole graphite surface, but aggregated in different areas of about 5 mm in diameter. Mass loss was not measured during the experiment.

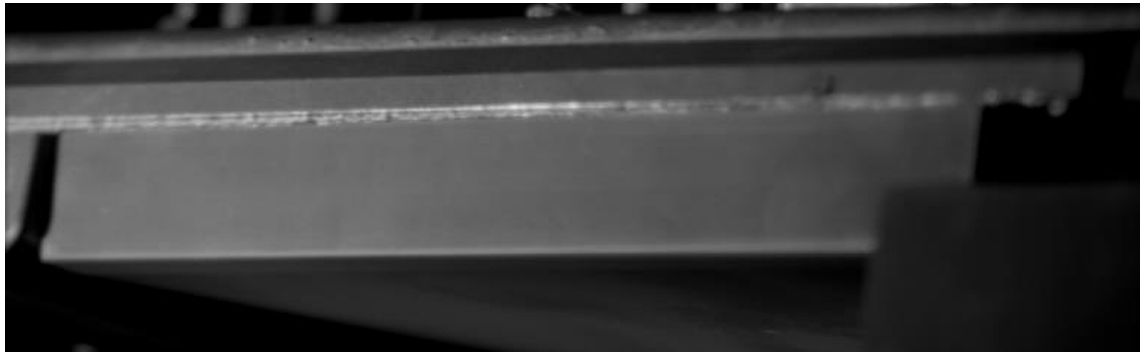


(a)

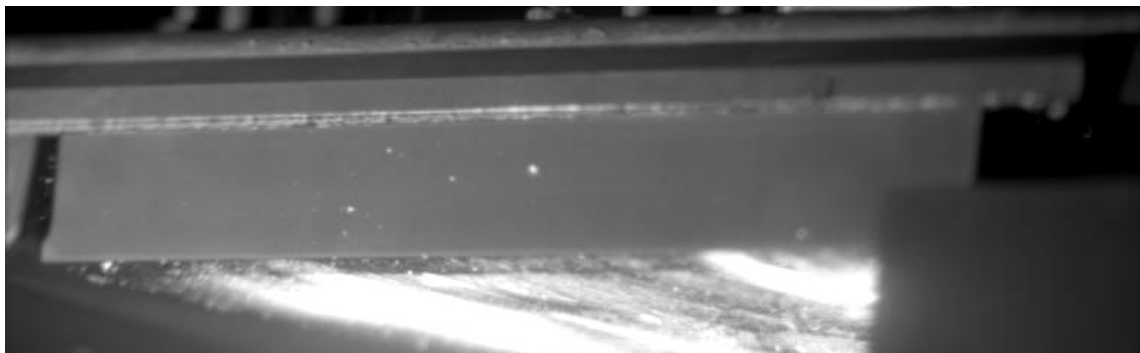


(b)

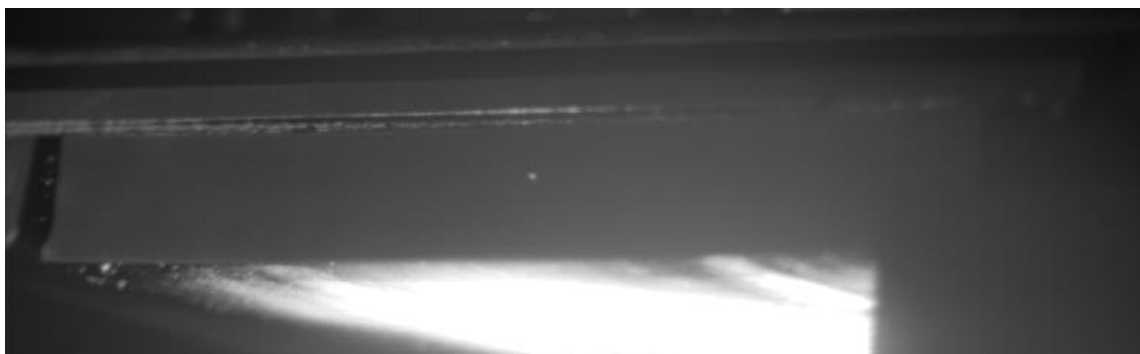
Figure 4.5: (a) Inspection with microscope. (b) Heat abrasion on graphite surface (x40 amplification).



(a)



(b)



(c)

Figure 4.6: GLADIS test scenario 3. (a) Before pulse. (b) Pulse start. (c) Maximum displacement.

4.2 Thermomechanical simulation of GLADIS

4.2.1 Thermal simulation (GLADIS)

Transient thermal simulation of GLADIS tests was implemented with the heat source parameters shown in table 4.4 and in accordance with equation 3.3. Power and deposited energy are calculated values. Radiation to ambient and from tile to clamping elements has been modelled. Steel structure has adiabatic conditions on its open surfaces. Initial temperature of the whole system is 20 °C.

Table 4.4: Parameters of the Gaussian distribution heat source applied on the graphite tile.

Id	Peak power MW/m ²	σ_x, σ_y mm	Peak location mm	Duration s	Power kW	Deposited energy kJ
1	9.99	[61, 61]	100	3.5	124.7	436.4
2			40		103.7	362.8
3	22.6	[55, 55]	100	1	254.6	254.6
4			40		211.3	211.3

Figure 4.7 displays the interest locations found during simulations, where 1a and 1b are for centred beams, 2a and 2b for a beam focused on the clamping region and 3 for the clamping slot in tile.

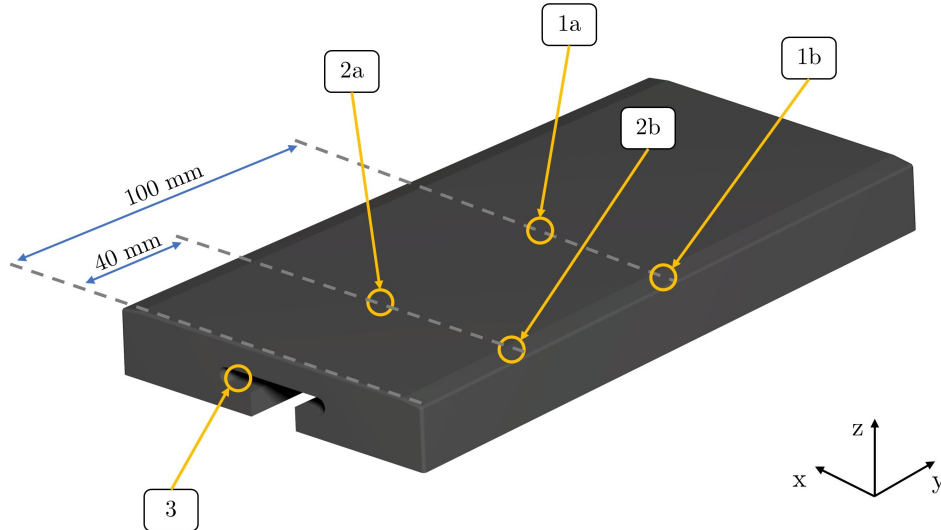


Figure 4.7: Interest location of simulation results.

The main transient thermal simulation results are shown in table 4.5. These are focused on the areas of interest since the temperature in those areas will directly determine the material’s safety factor. Heat load profiles are shown in figure 4.8, where negative values indicate a flux going into the tile.

Table 4.5: Heat flux and temperature in the areas of interest in GLADIS simulation.

Id	Location	Heat flux (MW/m ²)	Temperature (°C)
1	1a	9.81	1813.5
	1b	8.78	1197.8
2	2a	9.71	2039.4
	2b	8.58	1166.7
3	1a	22.67	2407.0
	1b	21.47	1384.6
4	2a	22.45	2425
	2b	20.8	1341.3

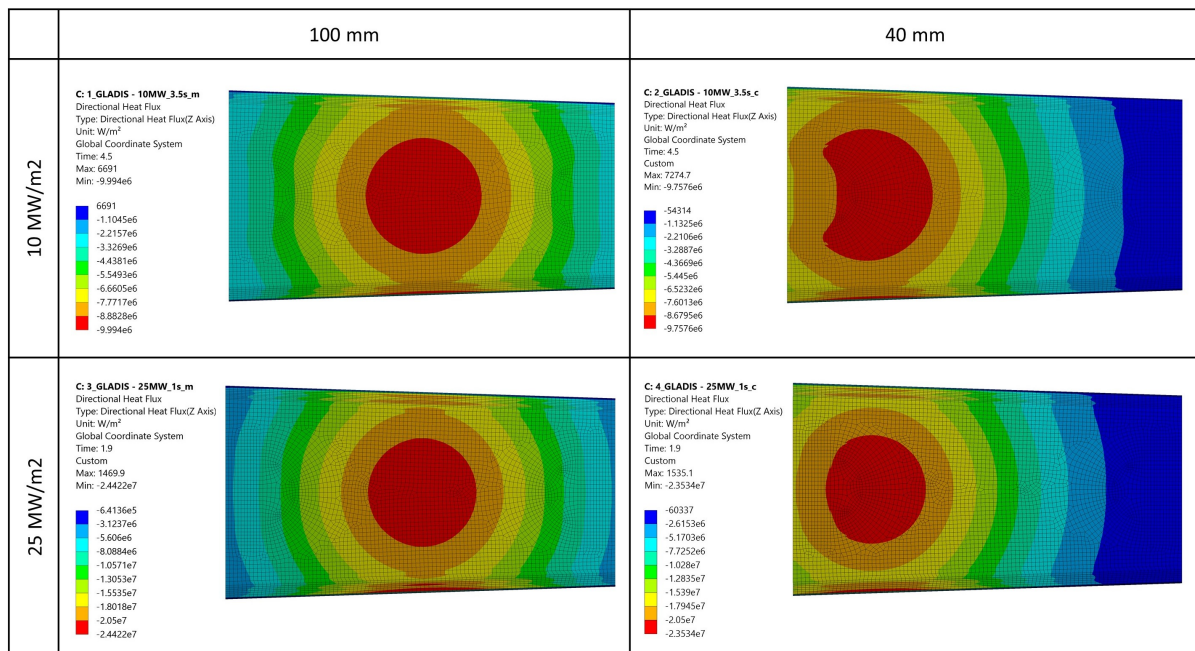


Figure 4.8: Heat source distribution for the 10 MW/m² and 25 MW/m² with peak centres in 100 mm and 40 mm, respectively.

Temperature distributions are shown in figures 4.9 and 4.10 which correspond to the 10 MW/m² heat sources. Figures 4.11 and 4.12 contain the results of the 25 MW/m².

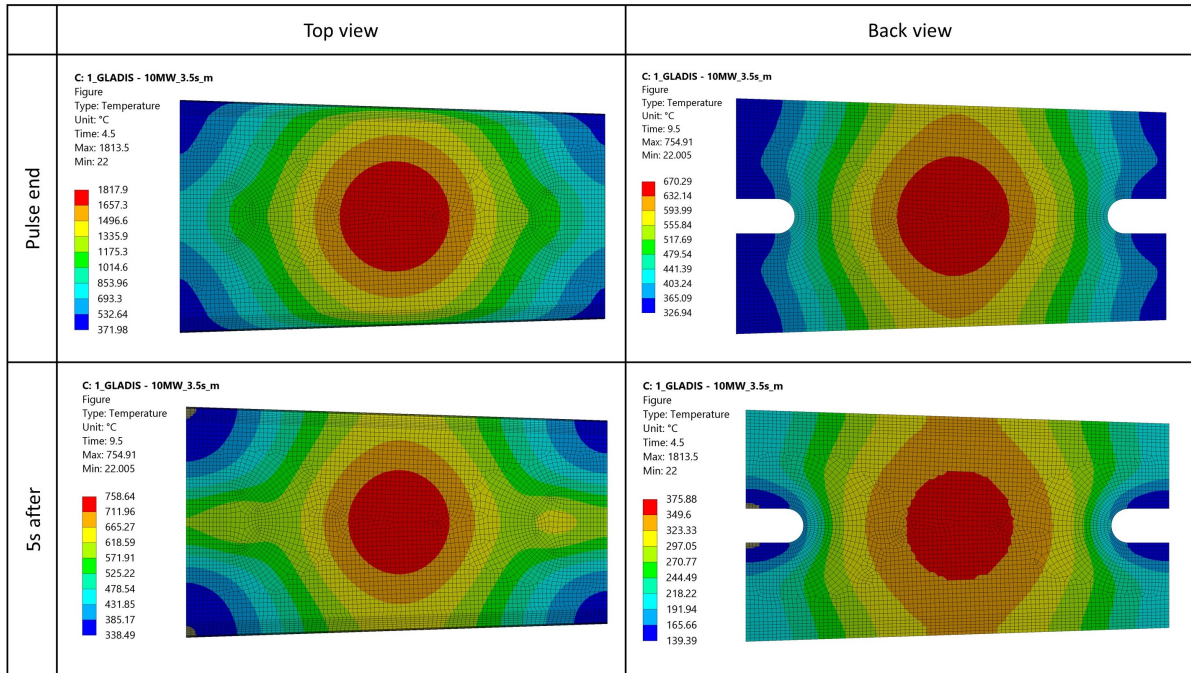


Figure 4.9: Temperature distribution of the upper and rear side of the tile during 10 MW/m² for 3.5s with centred beam (1 - GLADIS).

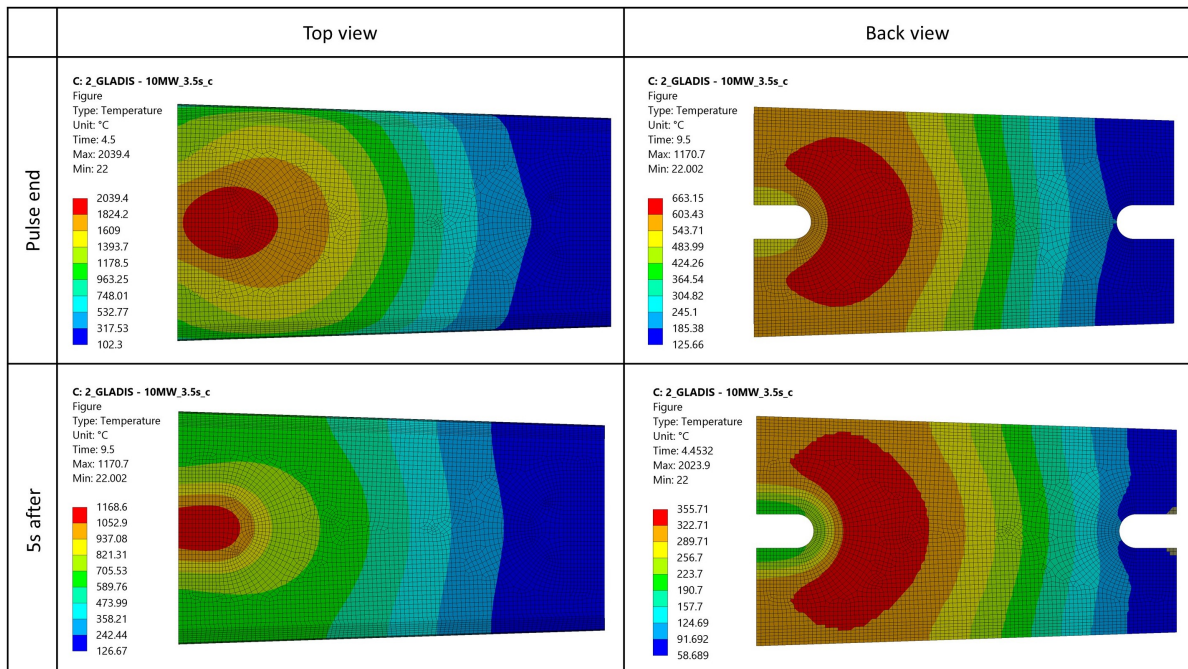


Figure 4.10: Temperature distribution of the upper and rear side of the tile during 10 MW/m² for 3.5s with beam focused on the clamp (2 - GLADIS).

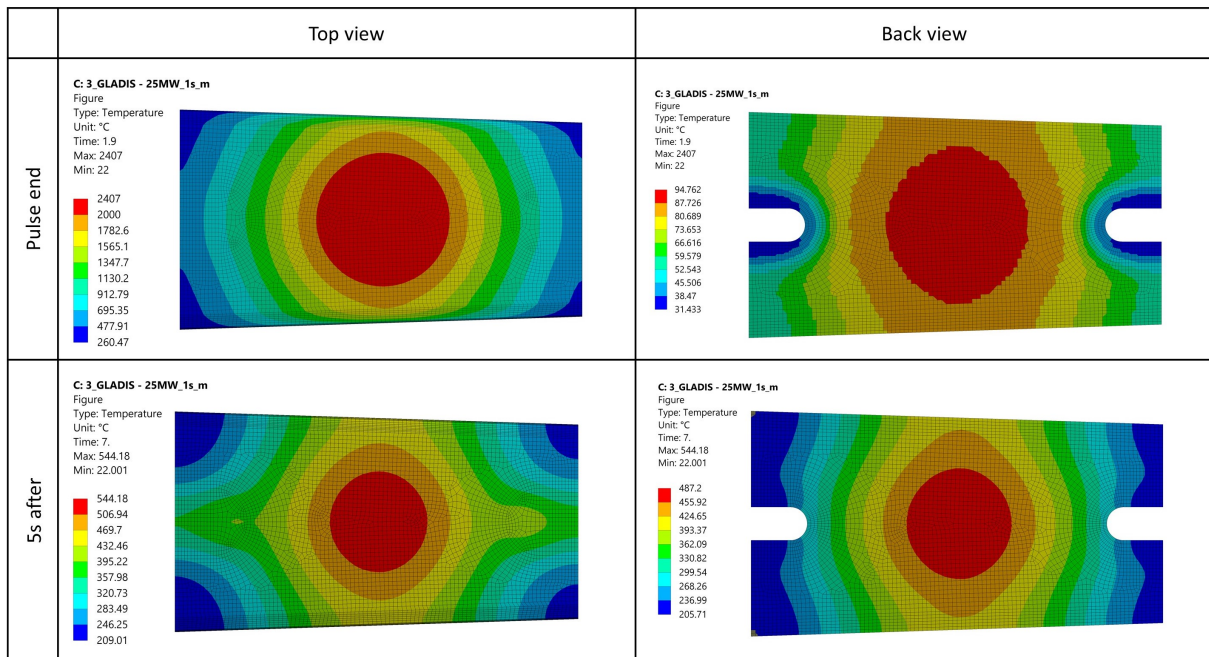


Figure 4.11: Temperature distribution of the upper and rear side of the tile during 25 MW/m² for 1s with centred beam (3 - GLADIS).

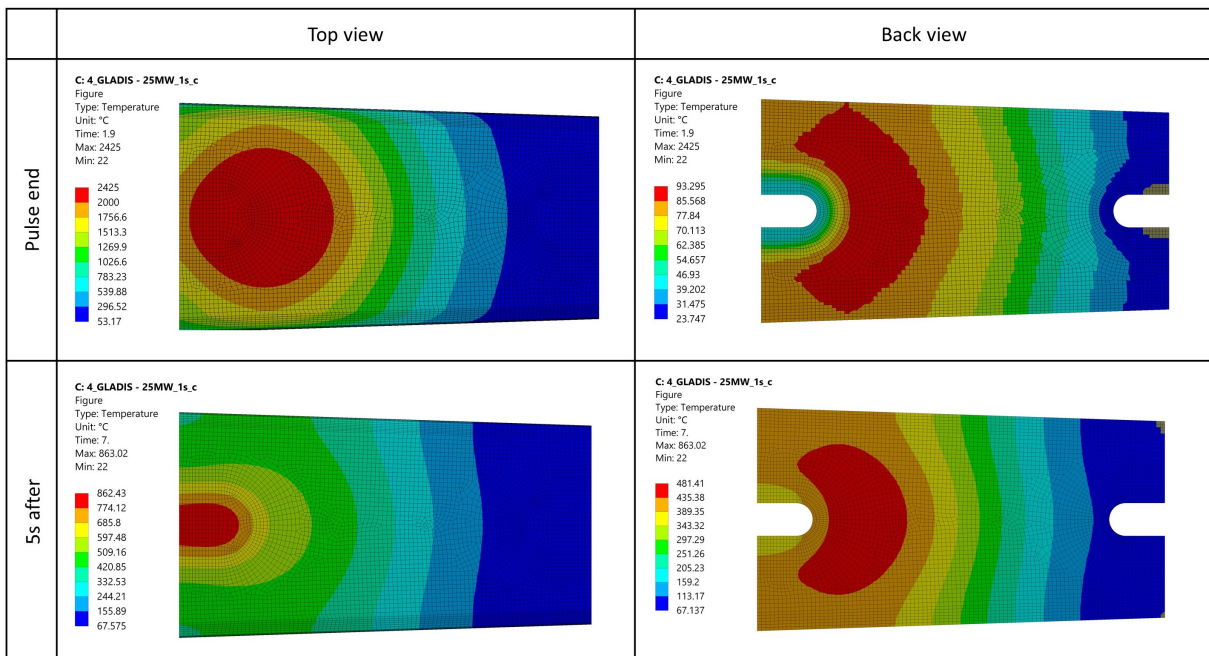


Figure 4.12: Temperature distribution of the upper and rear side of the tile during 25 MW/m² for 1s with beam focused on the clamp (4 - GLADIS).

4.2.2 Mechanical simulation (GLADIS)

During simulation two regions of the tile were found to be critical, tile's upper side on the beam's centre and clamping region of the wider part (1a, 2a and 3 on Fig. 4.7)). Maximum deformation and shear stresses were located at the peak centre and large principal stresses were concentrated on the clamping region. Mechanical results on that region required a finer analysis due to presence of a stress concentrator. Thanks to the convergence study, it was shown that the increased stresses were not caused by a singularity, but by a curvature change and proximity to a contact region. The solution was to provide an averaged result of the two closest nodes not belonging to the contact region, but part of the curvature. Figure 4.13 shows the contact region and the affected nodes, maximum stresses on these nodes will be averaged and used to calculate the safety factor.

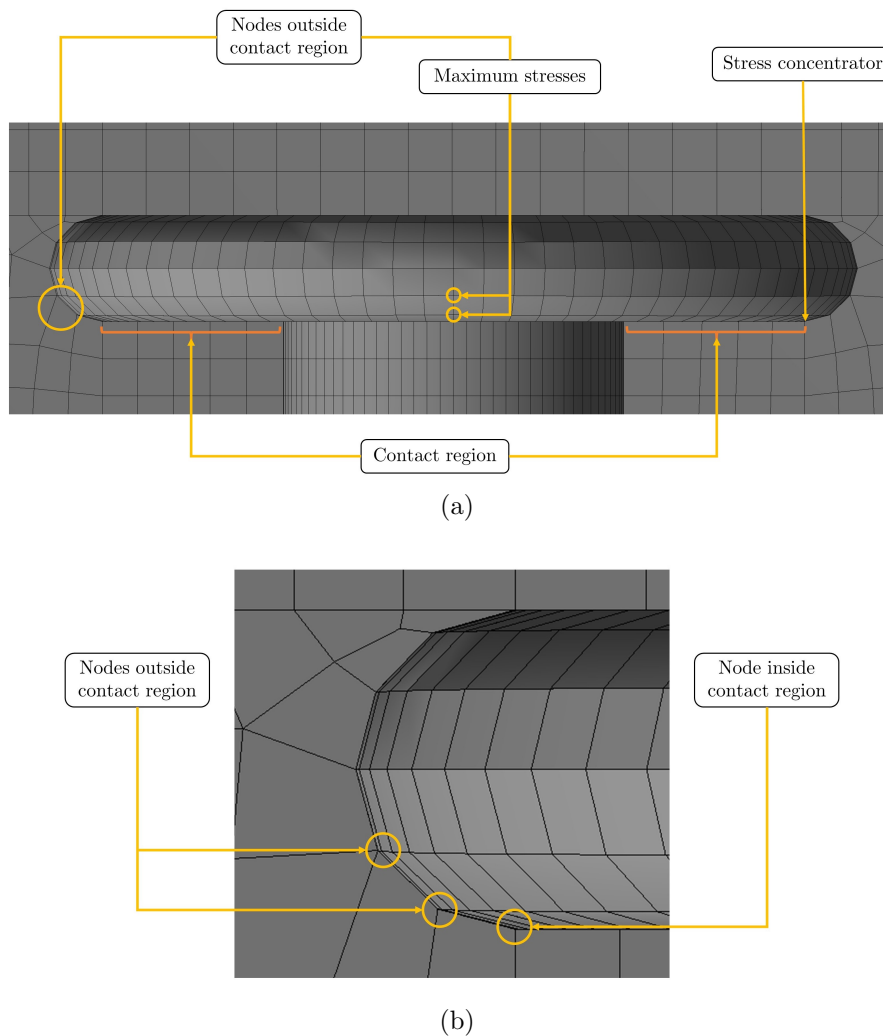


Figure 4.13: Clamping slot with stress concentrator.

Table 4.6 shows the principal stresses in the locations of interest and the displacement in the centre of the tile's upper side. Figures 4.14, 4.15, 4.16 and 4.17 show the total deformation of each case, respectively. Finally, table 4.7 presents the updated yield limit and calculated safety factors.

Table 4.6: Displacement and principal stresses on GLADIS mechanical simulation.

Test	δ_{max} (mm)	Location	σ_1 (MPa)	σ_2 (MPa)	σ_3 (MPa)	τ_{max} (MPa)
1	0.65	1a	0	- 64.5	- 74.9	37.1
		3	57.0	19.9	-2	25.1
2	0.41	2a	0.4	-86.1	-87.1	43.7
		3	89.1	36.8	0	37.6
3	0.73	1a	0	-130.9	-138.8	68.6
		3	62.0	19.4	0	27.5
4	0.47	2a	0	-150.1	-154.3	77.3
		3	95.77	38.1	0	40.5

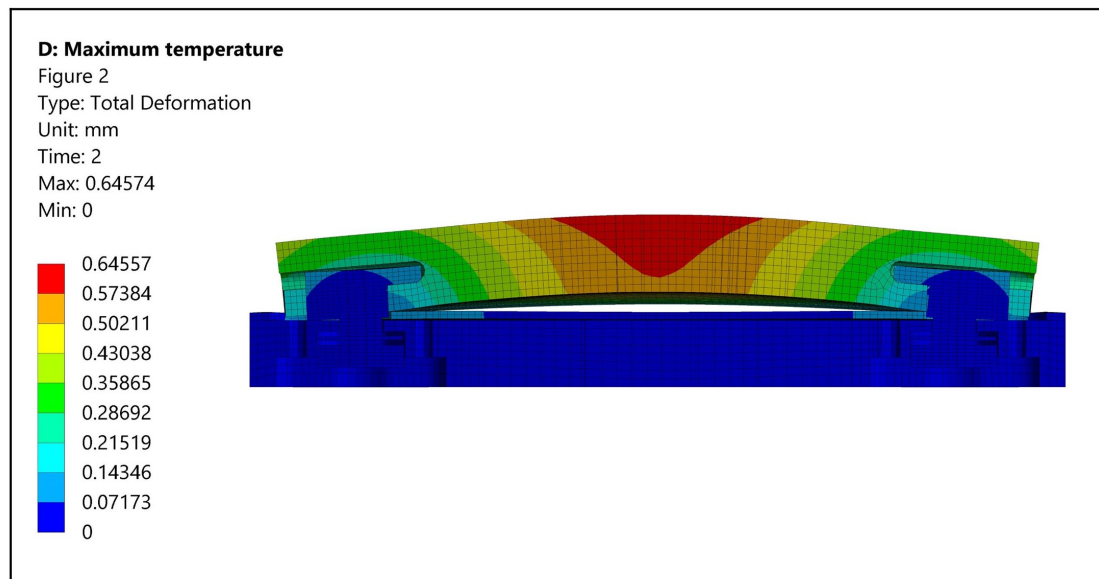


Figure 4.14: Total deformation of the 1 - GLADIS scenario (x10 amplification factor).

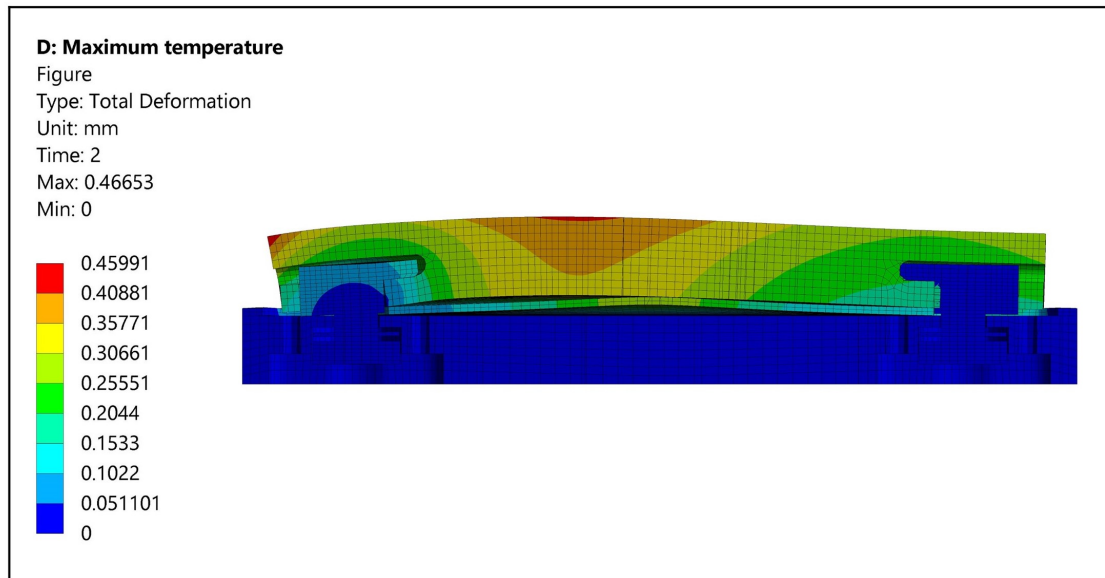


Figure 4.15: Total deformation of the 2 - GLADIS scenario (x10 amplification factor).

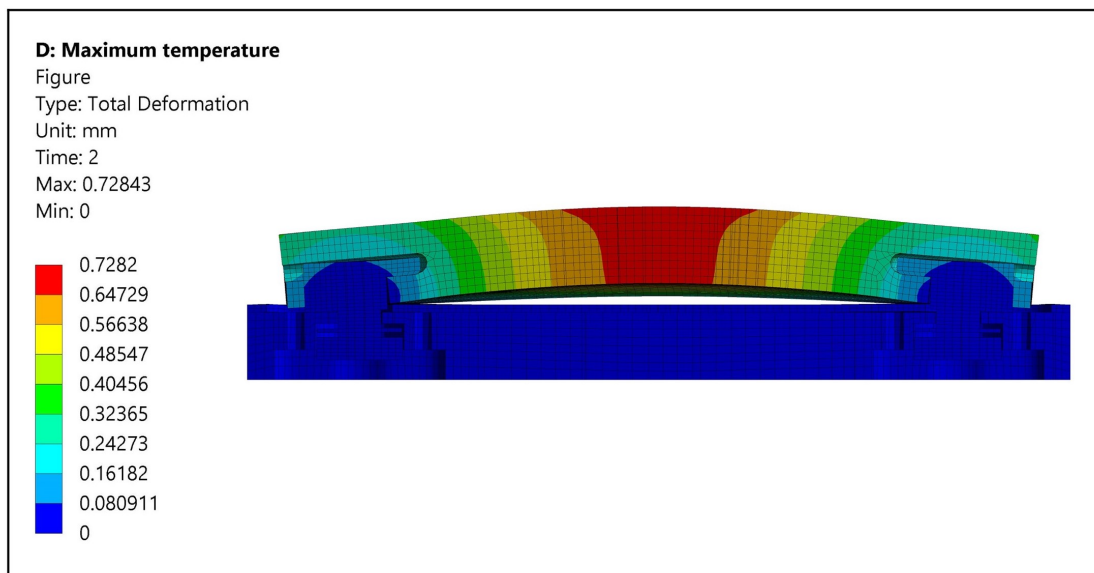


Figure 4.16: Total deformation of the 3 - GLADIS scenario (x8.5 amplification factor).

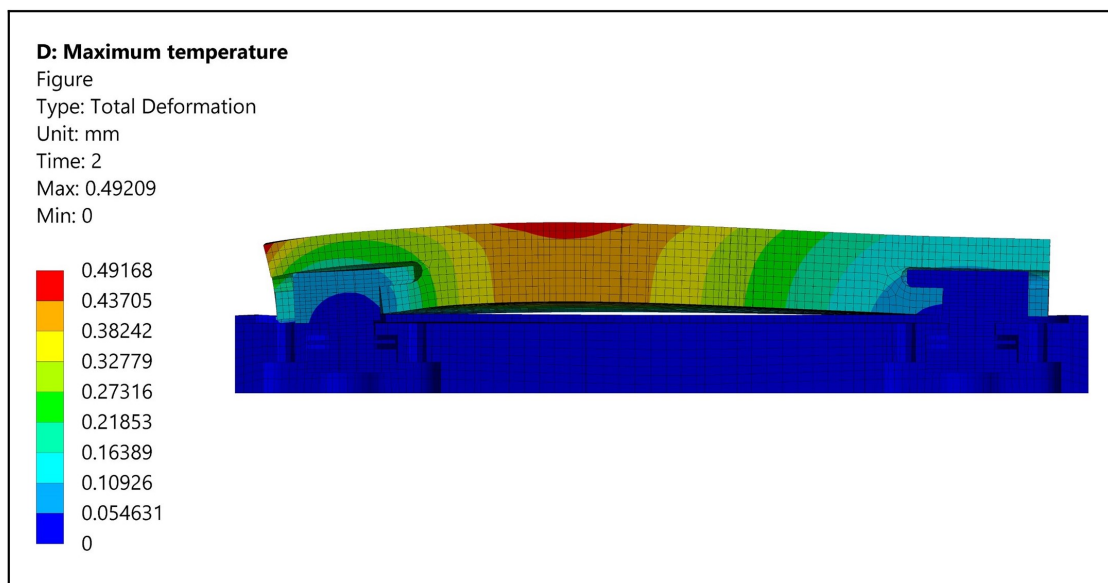


Figure 4.17: Total deformation of the 4 - GLADIS scenario (x8.5 amplification factor).

Table 4.7: Updated yield strength and safety factor of GLADIS tests.

Test	Location	Temperature (K)	S_{yield} (MPa)	SF_{MC}	$SF_{max.\sigma_1}$
1	1a	2086.5	109.7	2.27	Inf
	3	602.2	87.9	1.51	1.54
2	2a	2174.3	113.1	1.94	Inf
	3	686.4	88.2	0.99	0.99
3	1a	2678.3	163.5	1.22	Inf
	2	386.7	86.2	1.39	1.39
4	1b	2698.0	165.1	1.1	Inf
	2	895.2	89.46	0.9	0.9

4.3 Thermomechanical simulation of AUG divertor

4.3.1 Thermal simulation (AUG)

Similarly done for table 4.4, main thermal results of the FEM simulation of AUG scenarios is shown in table 4.8. Maximum measured heat flux on the tile is presented in figure 4.18 and 4.19 contains the flux distribution.

Table 4.8: Parameters of the Gaussian distribution heat source applied on the graphite tile in the AUG scenario simulation.

Id	Peak power MW/m ²	σ_x, σ_y mm	Peak location mm	Duration s	Power kW	Deposited energy kJ
1 - AUG	14.78	[50, 6]	41.6	3	19.63	58.89
2 - AUG	7.1	[50, 10]	41.6	10	15.54	155.38

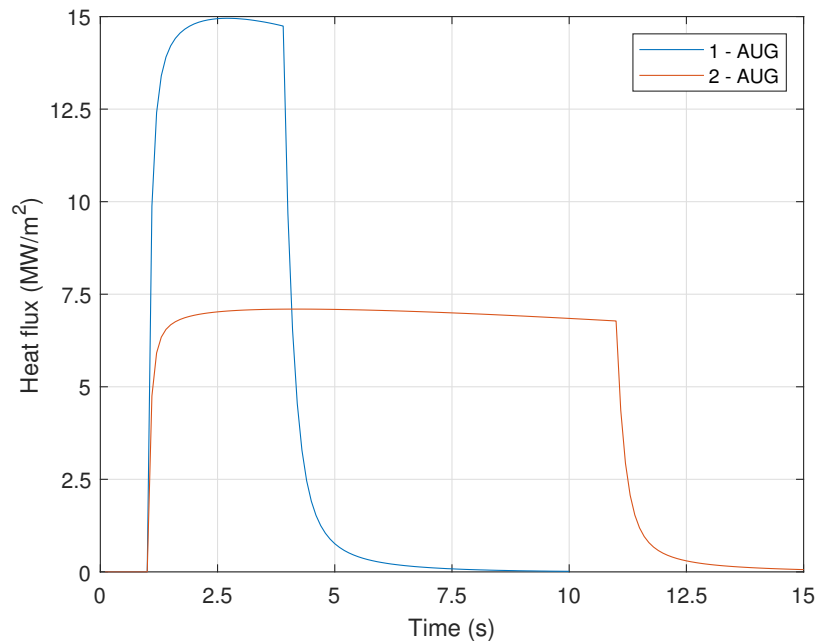


Figure 4.18: Heat flux at the peak location for the 15 MW/m² and 7 MW/m² distributions.

Finally, table 4.9 contains the heat flux and temperature in the areas of interest, whilst figure 4.20 and 4.21 show the temperature distribution.

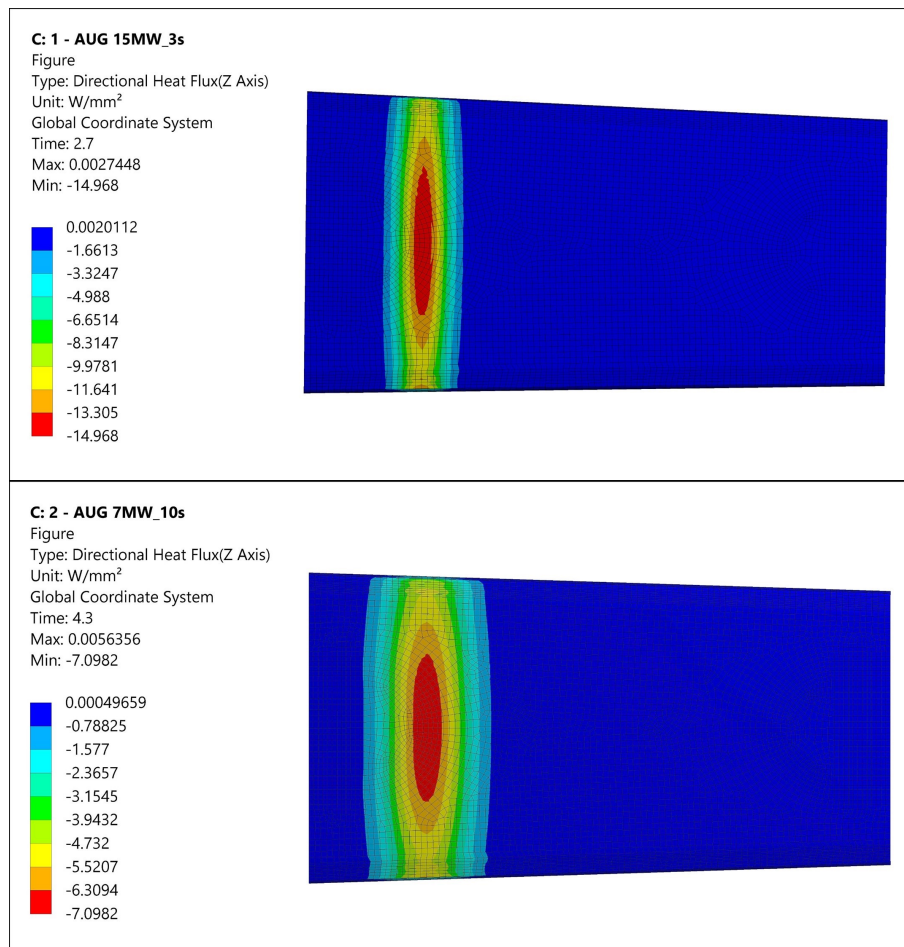


Figure 4.19: Heat flux distribution for the two AUG scenarios.

Table 4.9: Heat flux and temperature in the areas of interest of AUG simulation.

Id	Location	Heat flux (MW/m ²)	Temperature (°C)
1 - AUG	1a	14.78	2106.4
	1b	11.92	1040
2 - AUG	2a	7.1	1733
	2b	5.18	960.4

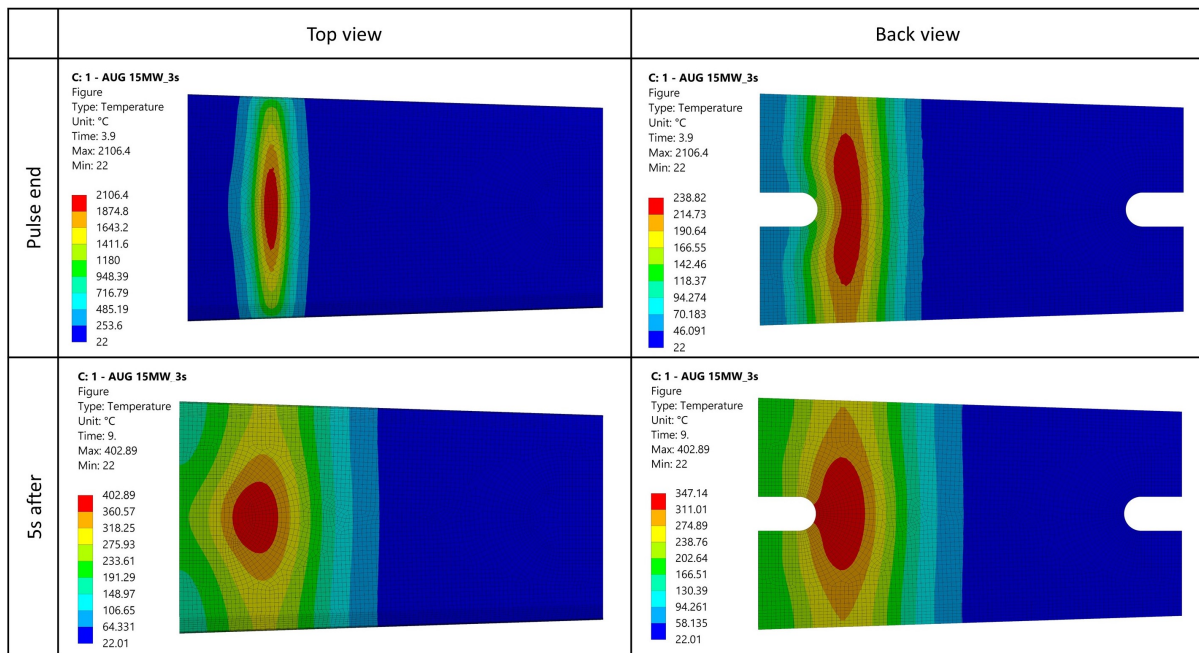


Figure 4.20: Temperature distribution of the upper and rear side of the tile during 15 MW/m² for 3s with beam focused on the clamp (1-AUG).

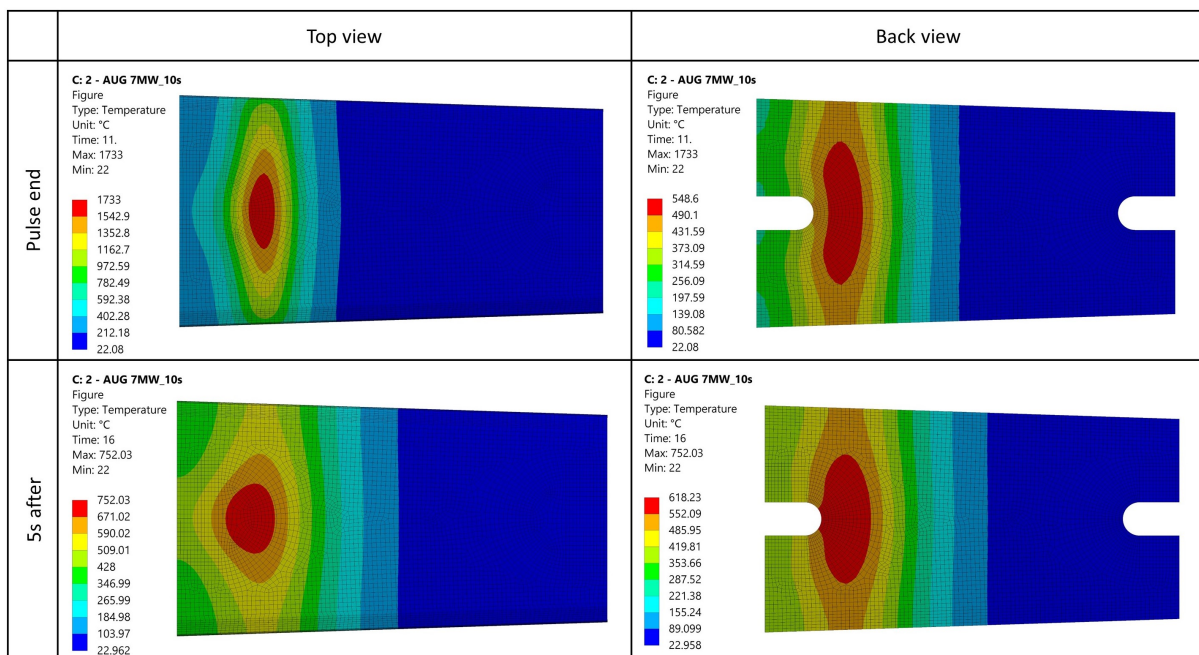


Figure 4.21: Temperature distribution of the upper and rear side of the tile during 7 MW/m² for 10s with beam focused on the clamp (2-AUG)

4.3.2 Mechanical simulation (AUG)

In the mechanical simulation of AUG cases the same procedure as for the GLADIS cases was followed. Temperature distribution at peak temperature calculated in the thermal simulation was used as input. Table 4.10 contains the directional displacement in the Z direction and the principal stresses. Figure 4.22 and 4.23 show the total deformation for each scenario.

Table 4.10: Displacement and principal stresses on AUG mechanical simulation.

Test	δ_{max} (mm)	Location	σ_1 (MPa)	σ_2 (MPa)	σ_3 (MPa)	τ_{max} (MPa)
1	0.14	1a	0	-55.3	-134.1	67
		3	31.7	6.6	0	14.7
2	0.15	2a	0	-37.4	-80.9	40.4
		3	31.5	5.5	0	15.3

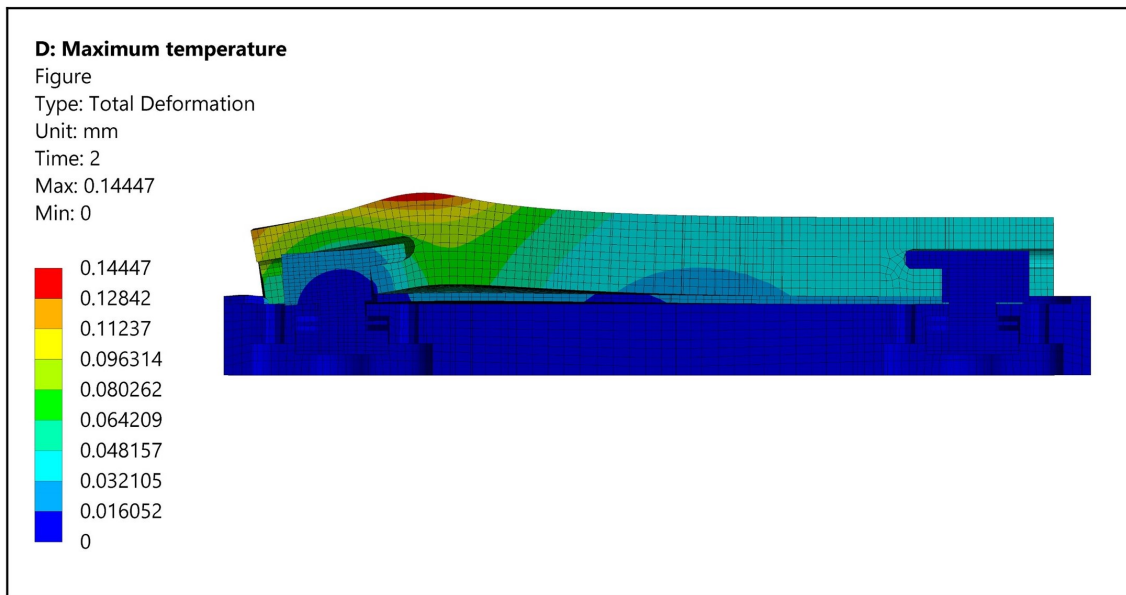


Figure 4.22: Total deformation of the 1 - AUG scenario (x43 amplification factor).

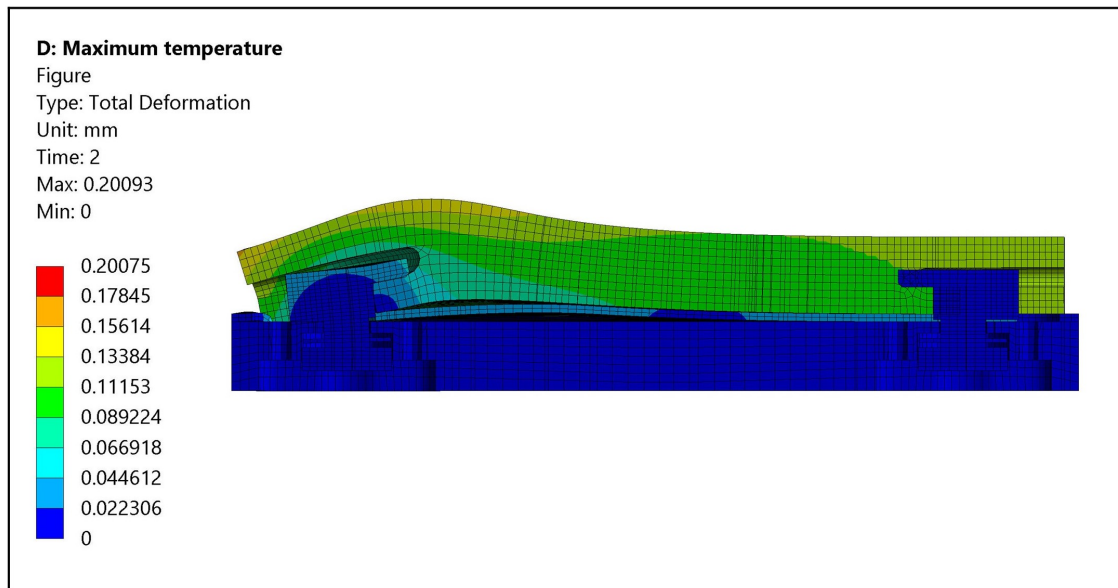


Figure 4.23: Total deformation of the 2 - AUG scenario (x64 amplification factor).

Table 4.11 presents the final safety factors calculated. 1 - AUG scenario with 15 MW/m^2 and 3 s exposure time resulted in lower overall safety factors, due to the increased temperature gradient, despite the fact that 2 - AUG had higher deposited energy.

Table 4.11: Updated yield strength and safety factor of GLADIS tests.

Test	Location	Temperature (K)	S_{yield} (MPa)	SF_{MC}	$SF_{max.\sigma_1}$
1 - AUG	1a	2379.4	125.7	1.27	Inf
	3	577.5	87.7	2.77	2.77
2 - AUG	2a	2006	107.2	2.1	Inf
	3	895.2	89.5	2.84	2.84

Chapter 5

Discussion

5.1 GLADIS experimental campaign

5.1.1 Thermal simulation and comparison to experimental data

Thermography imaging from GLADIS provided the main parameter to evaluate the peak temperature distribution on the tile and it was used as a design parameter for the heat source simulation. As it will be showed in this chapter, this approach might have been flawed for high energy pulses applied on graphite.

Comparing the surface temperature results presented on chapter 4 we arrive to table 5.1, where the experimental and simulation peak temperatures are presented. Difference in maximum temperatures are most noticeable in pulses where the peak was located closer to the clamping region. The cause for these could be attributed to different error sources, such as error in measurement at high temperatures due to uncertainty of the tile emissivity (used to measure temperature with pyrometer) and uneven heating of tile surface. Simulations error such as an improper physical description of the tile material might also be responsible. However, increased cooling due to the peak location must not be ruled out.

Table 5.1: Maximum surface temperatures of GLADIS (G) and simulation (S) result comparison.

Id	T _{G,surf} (°C)	T _{S,surf} (°C)	ΔT (°C)	[%]
1	1796.1	1813.5	17.4	1 %
2	1933.0	2039.4	106.4	5.5 %
3	2398.2	2407.0	8.8	0.4 %
4	2472.4	2425.0	-47.4	-1.9 %

Figure 5.1 shows a comparison of the temperature profile from the IR thermography and the simulation results, proving an adequate simulation of the heat source for case 1 - GLADIS. Figure 4.2 showed uneven heating and hotspots during the $25\text{MW}/\text{m}^2$ pulses, difficulting the process of characterizing the results. For that reason, a comparison of the profiles (e.g. figure 5.1) would not provide conclusive data.

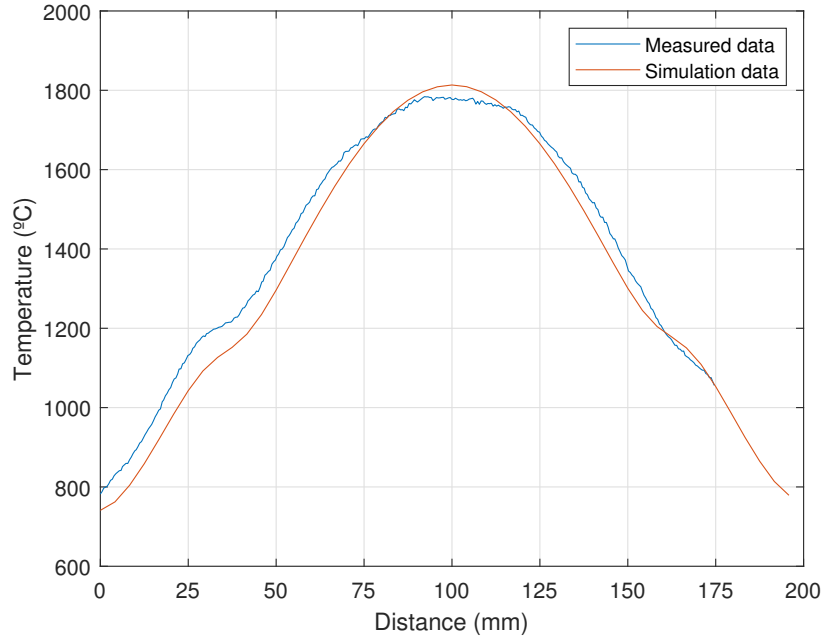


Figure 5.1: Temperature measured in the poloidal symmetry axis during a $10\text{MW}/\text{m}^2$ after 3.5s pulse.

Tile emissivity used for simulations was taken from [17] and assumed to have a value of 0.75. This figure proved to be in accordance with measured data obtained during the experimental phase, which averaged to 0.69. However, thermal imaging through infrared (Fig. 4.1b) was not accurately done due to the graphite block (Fig. 3.18a) obstructing the view of the maximum heat area on scenarios 2 and 4 - GLADIS.

In the FEM simulation, for the $25\text{MW}/\text{m}^2$ pulses the peak power on the tile reached $22.7\text{MW}/\text{m}^2$, 9.3% lower than the design, and slightly larger than the 5% difference observed in the latests GLADIS experiments [5]. With figures 5.2, 5.3, 5.4 and 5.5 a more in depth analysis of the heat fluxes and cool-down can be made.

Figure 5.2 shows proper thermal simulation, according to surface temperature evolution, since both peak value and ramp-up are matched. Figure 5.3 presents an accurate ramp-up, but a peak difference of $100\text{ }^\circ\text{C}$. Cool-down is slower for both 2 and 4 - GLADIS scenarios, marked in both cases with vertical arrows. The main cause for this difference is the fact that the peak power locations are closer to the inlet water pipe, having therefore enhanced cooling. This might have also affected the peak temperature difference, since in the simulation no heat extraction was added.

For the 25 MW/m^2 a difference in the ramp up can be observed, which would indicate a lower heat flux applied on the tile, despite the low peak temperature difference.

Taking into account hot-spots in figure 4.2 and graphite sublimation in figure 4.5b, the effect that it had at high temperatures should not be ignored. Reached temperatures during scenarios 3 and 4 - GLADIS had 4 orders of magnitude higher graphite sublimation and, thus, higher heat release from the tile. However, modelling material sublimation remained outside the scope of the project.

Comparing the IR thermography images and the resulting simulation gradients the beam source was apparently properly simulated for the 10 MW/m^2 energy pulses. However, the 25 MW/m^2 pulses could not be properly characterized with the provided data, since there is a high level of uncertainty on the peak temperatures.

In summary, on the one hand simulations showed high agreement with the measured data at the lower heat fluxes with peak temperatures in the order of $2000 \text{ }^\circ\text{C}$ and because of that it was concluded that the proposed AUG plasma scenarios would provide valid results. On the other hand, it was found out that uncoated graphite tiles should not be tested at high heat fluxes to prevent sublimation and unable a proper thermal characterisation. The effect of the cool-down system on the peak temperatures remains unclear for peak locations closer to the inlet and require further investigation.

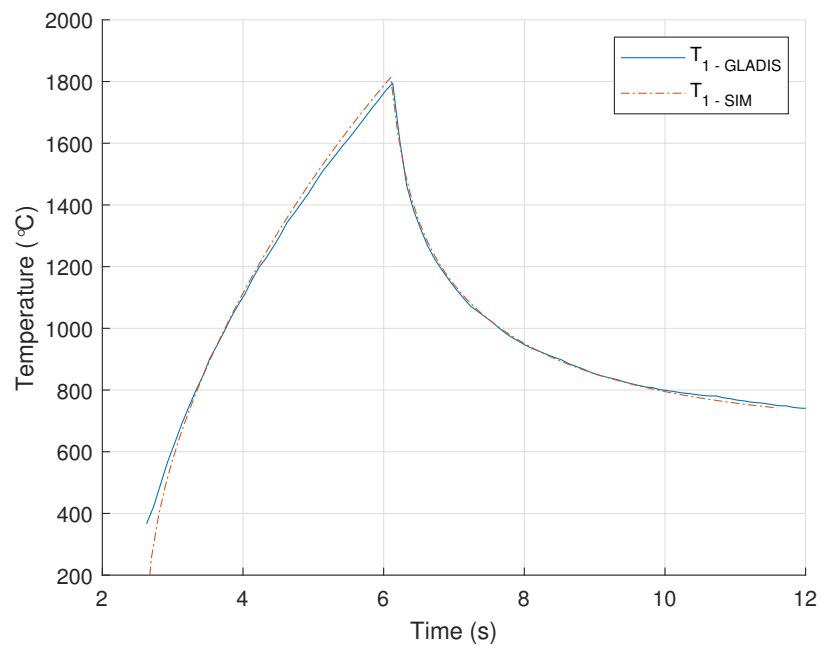


Figure 5.2: Simulation and experimental temperature evolution for GLADIS scenario 1.

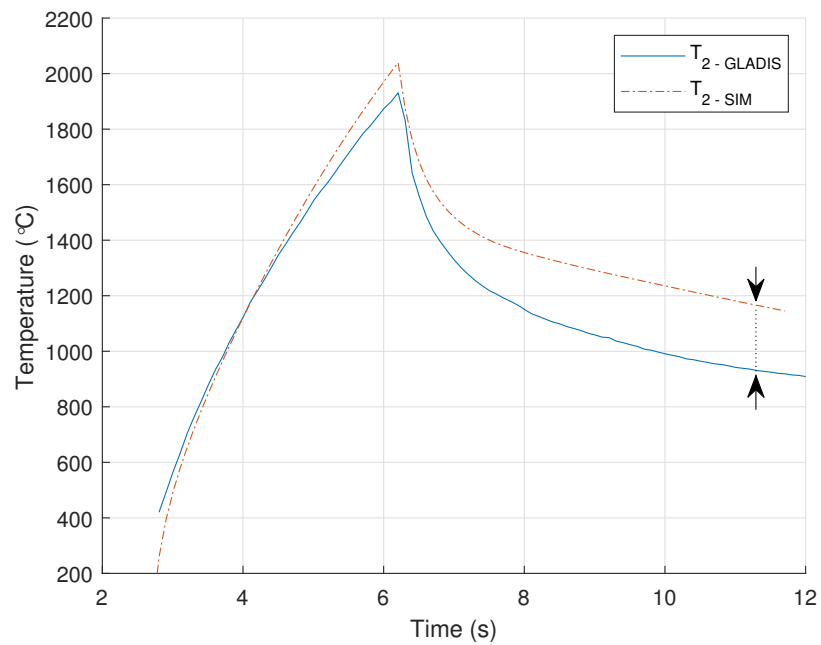


Figure 5.3: Simulation and experimental temperature evolution for GLADIS scenario 2.

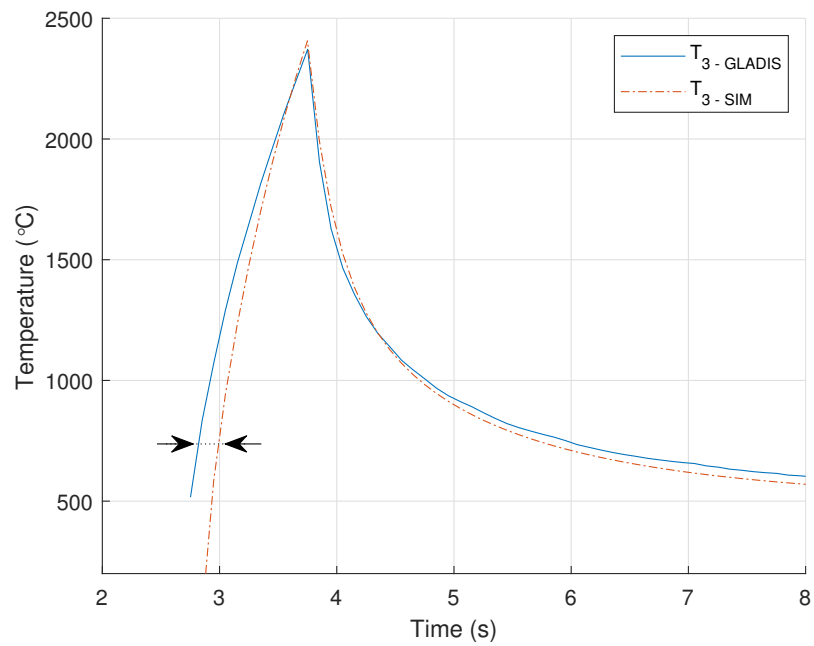


Figure 5.4: Simulation and experimental temperature evolution for GLADIS scenario 3.

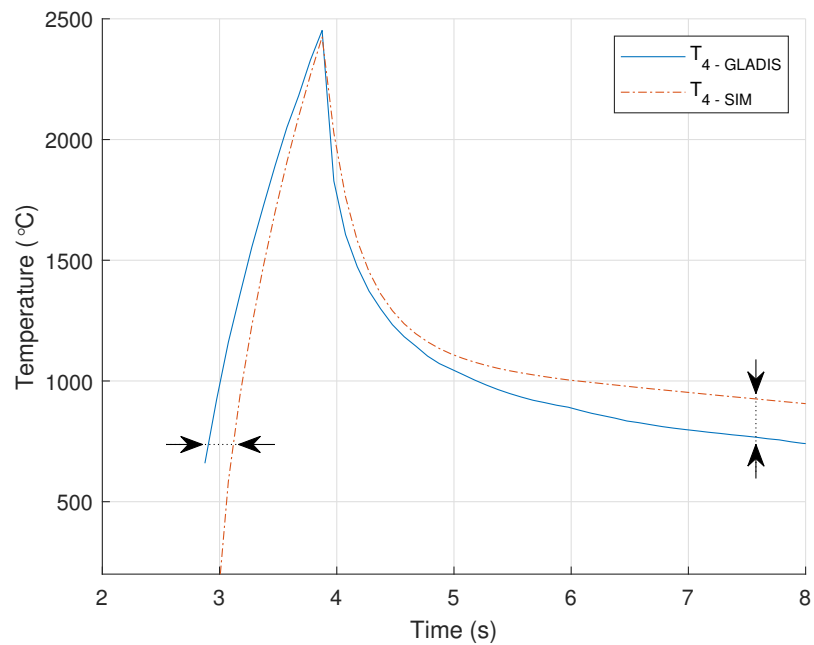


Figure 5.5: Simulation and experimental temperature evolution for GLADIS scenario 4.

5.1.2 Mechanical simulation of GLADIS tests

On the subject of the mechanical simulation, weakest area proved to be the clamping region, where maximum multiaxial stresses and lower safety factors were found. SF, as calculated with the yield limit remained over 0.90 on the clamping region. However, the effect of the stress concentrator and closeness to a contact region increased the total calculated stresses. All in all, the analysis showed tile resistance under the proposed loading, which was confirmed during inspection after the experimental campaign. Nevertheless, increased danger of fracture generation and propagation due to fatigue was not assessed, therefore subsequent studies should focus on the life-cycle of the tile.

Displacement sensor showed consistently larger values than simulated (Tab 5.2). This can be attributed to factors such as instrumentation errors, due to the calibration of the sensor or higher than recommended operation temperature (105 °C). Furthermore, the tile in the FEM model could be more tightly clamped to the structure during pulses, which would result in higher stresses. Therefore, in future works an improved measurement set-up should be implemented, one with higher operation temperature and better calibration prior to use. Additionally, disk spring behaviour should be modelled to more accurately determine the pressure increase with thermal expansion.

Table 5.2: Displacement measured on the tile during pulses and simulation results.

Id	δ_{AVG} (mm)	δ_{SIM} (mm)	$\Delta\delta$ (mm)	[%]
1	1.04	0.65	0.39	-37.5 %
2	0.63	0.41	0.22	-34.9 %
3	1.39	0.73	0.66	-47.5 %
4	0.87	0.47	0.40	-47.5 %

Finally, slower pulses with higher deposited energies resulted in lower stresses, due to the lower temperature gradient. Indicating that faster transients with higher heat fluxes will cause the larger strains on the upper outer divertor.

5.2 AUG plasma simulation

A limitation found during the project was the inability to experimentally simulate the heat flux during plasma operation at AUG. The only available option was to use the radially symmetric source at GLADIS. This resulted in higher deposited energies, but a lower thermal gradient, which could lead to failure. Therefore FEM simulations acquire a higher degree of importance in this context.

AUG scenarios heat fluxes were accurately simulated in ANSYS workbench, with a maximum discrepancy of -1.4 %. Maximum temperature was reached in 1 - AUG, with a peak value of 2106.4 °C. Figure 5.6 shows the temperature evolution of both scenarios. Analysing the figures 4.20 and 4.21 it is observed that overall temperatures are larger in the second scenario due to the higher deposited energy. However, lower gradients result in lower stresses, despite larger thermal expansion.

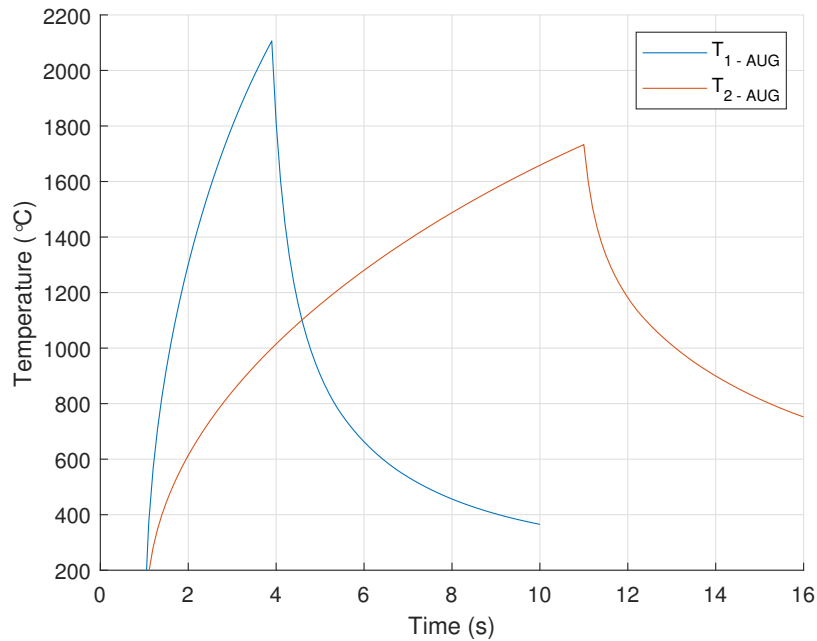


Figure 5.6: Temperature evolution for the two AUG scenarios.

The experimental campaign was useful to benchmark the ANSYS simulations and validate the analyses. Temperature evolution of the lower energy cases confirmed the validity of the simulation approach, even though stresses were found to be larger under GLADIS heat fluxes. This, actually proved tile resistance under higher than normal conditions, increasing the reliability of the study. All in all, for the AUG cases, the lowest safety factor calculated with Mohr-Coulomb remained over 2.77 in the clamping region, indicating non-yielding of the tile and a large slack during operation.

Chapter 6

Conclusions

A new upper divertor is to be installed in the near future at ASDEX Upgrade. The design of this plasma facing component has been developed and the aim of this work was to perform finite element method simulations to analyse its behaviour and confirm the validity of the new design. An experimental phase at GLADIS was performed to evaluate the validity of the simulations and tile's behaviour under high heat fluxes.

Summarizing the achievements of this master thesis, thermomechanical simulation of the graphite tile design with GLADIS heat source was performed and analysed. This was followed by an experimental phase, which aided in the validation of the simulations. Finally, a simulation of the tile under ASDEX Upgrade plasma was performed, which proved the tile's resistance under operation. Additionally, it was demonstrated that the model simplification of not including the cooling flow was a valid approach for stress calculations at maximum temperature and ramp-up, but not for temperature distributions during cool-down. Finally, it was found out that at higher heat fluxes graphite sublimation prevented a proper measure of the temperature of an uncoated graphite tile through IR thermography. In the analyses this effect was not considered.

A missing element from the validation is the measurement of the heat transfer through the clamping mechanisms to the structure. Contact pressure and thermal conductance are highly correlated, however the values are estimated from previous works. Additionally, tungsten coating of graphite tiles should be done and studied prior to next experimental phases. As prospective works to the current project, the following activities are proposed. Develop a model including electromechanical effects of plasma on graphite. Test a tungsten coated tile to assess tungsten coating behaviour and maximum operational conditions. Perform a life cycle assessment of the upper divertor.

All in all, the new upper divertor tile design has been validated through thermomechanical simulations that were benchmarked via an experimental campaign and will resist normal operation at ASDEX Upgrade.

Bibliography

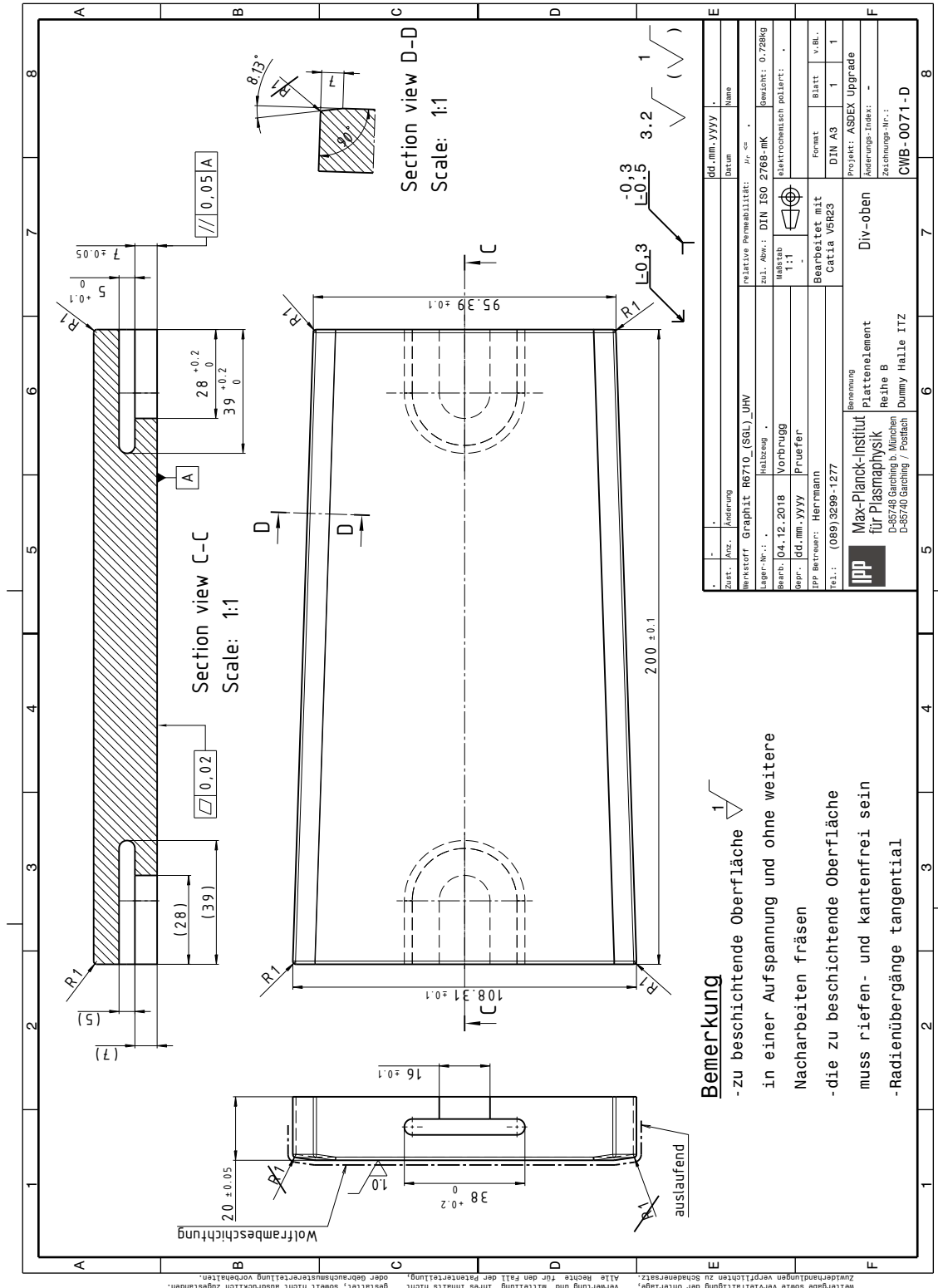
- [1] Appendix a, materials design limit data v3.3., 2013. IDM 222RLN, Page 65.
- [2] SGL Carbon. SIGRAFINE R6710 Datasheet. <https://www.sglcarbon.com/pdf/SGL-Datasheet-SIGRAFINE-R6710-EN.pdf>, 2019.
- [3] F. Escourbiac. Seminar. The ITER divertor Design and Engineering challenges. http://irfm.cea.fr/Phocea/file.php?file=Seminaires/2126/Seminar_Escourbiac.pdf, 2014.
- [4] H Greuner, B Boeswirth, J Boscary, and P McNeely. High heat flux facility gladis:: Operational characteristics and results of w7-x pre-series target tests. *Journal of Nuclear Materials*, 367:1444–1448, 2007.
- [5] Henri Greuner, B Böswirth, K Hunger, A Khan, TR Barrett, F Gallay, M Richou, E Visca, AV Müller, and JH You. Assessment of the high heat flux performance of european demo divertor mock-ups. *Physica Scripta*, 2020(T171):014003, 2020.
- [6] A Herrmann, H Greuner, N Jaksic, B Böswirth, F Reimold, A Scarabosio, S Vorbrugg, M Wischmeier, et al. Design and concept validation of the new solid tungsten divertor for asdex upgrade. *Fusion Engineering and Design*, 88(6-8):577–580, 2013.
- [7] A Herrmann, M Teschke, I Zammuto, M Cuevas, M Dibon, A Kallenbach, T Lunt, V Rohde, G Schall, T Vierle, et al. A new upper divertor with internal coils for asdex upgrade—status of the project. *Fusion Engineering and Design*, 146:920–923, 2019.
- [8] ASTM International. Standard Practice for Testing Graphite and Boronated Graphite Materials for High- Temperature Gas-Cooled Nuclear Reactor Components, Designation C781-08, 2014.
- [9] Masahiro Ishihara, Junya Sumita, Taiju Shibata, Tatsuo Iyoku, and Tatsuo Oku. Principle design and data of graphite components. *Nuclear Engineering and Design*, 233(1-3):251–260, 2004.
- [10] Nikola Jaksic, Henri Greuner, Albrecht Herrmann, Bernd Böswirth, and Stefan Vorbrugg. Results of high heat flux tests and structural analysis of the new solid tungsten divertor tile for asdex upgrade. *Fusion Engineering and Design*, 98:1333–1336, 2015.

- [11] M Khelifa, V Fierro, J Macutkevic, and A Celzard. Nanoindentation of flexible graphite: experimental versus simulation studies. *Adv Mater Sci*, 3(2):1–11, 2018.
- [12] Jochen Linke, Juan Du, Thorsten Loewenhoff, Gerald Pintsuk, Benjamin Spilker, Isabel Steudel, and Marius Wirtz. Challenges for plasma-facing components in nuclear fusion. *Matter and Radiation at Extremes*, 4(5):056201, 2019.
- [13] Luis Guilherme Borzani Manhani, Luiz Claudio Pardini, and Flaminio Levy Neto. Assesment of tensile strength of graphites by the iosipescu coupon test. *Materials Research*, 10(3):233–239, 2007.
- [14] GF Matthews, P Coad, H Greuner, M Hill, T Hirai, Jari Likonen, H Maier, M Mayer, R Neu, V Philipps, et al. Development of divertor tungsten coatings for the jet iter-like wall. *Journal of nuclear materials*, 390:934–937, 2009.
- [15] Mersen. Papyex Datasheet. <https://www.mersen.com/sites/default/files/publications-media/6-gs-papyex-graphite-souple-mersen.pdf>, 2018.
- [16] B Streibl, H Greuner, A Herrmann, S Koetterl, S Mukherjee, S Schweizer, J Simon-Weidner, H Euringer, J Linke, M Sauer, et al. Non-brazed plasma facing component for high steady state heat flux. In *Fusion technology 1998*. 1998.
- [17] RJ Thorn and OC Simpson. Spectral emissivities of graphite and carbon. *Journal of Applied Physics*, 24(5):633–639, 1953.

Appendix A

Technical drawings

A.1 Graphite tile (CWB-0071D)



Weitergabe sowie Vervielfältigung der Unterlage, Verwertung und Mitteilung ihres Inhalts nicht gestattet, soweit nicht ausdrücklich zugestanden. Alle Rechte für den Fall der Patentierung, Reservierung und Aneignung vorbehalten.

Appendix B

Developed codes

B.1 Deposited energy calculation

Calculation of input power and deposited energy on a trapezoidal plane with finite limits with MATLAB.

Listing B.1: Main code (dep_energy.m)

```
1  %---Heat flux parameters---%
2
3  A = 15; %Peak heat flux (MW/m2)
4  time = 3; %Pulse duration (s)
5
6  xc = 40; %beam center x,y
7  yc = 0;
8
9  sig_x = 55; %standard deviation x, y
10 sig_y = 55;
11
12 %---Tile dimensions-----%
13
14 % Geometry:
15 %
16 % |---
17 % |      ---
18 % |      -----
19 % |      |
20 % h1 |-----| h2 <- symmetry axis
21 % |      |
22 % |      -----
23 % |      ---
24 % |---
25 %
26 % |<--- x -->|
```

```

27
28 h1 = 105;
29 h2 = 95;
30 l = 200; %length
31 formfunction = @(xnorm) (1-xnorm)*h1/2 + xnorm*h2/2;
32
33 %----Mesh generation----%
34
35 dimX = 200; %each division in x must b of 1 mm
36 dimY = 99;
37
38 x = linspace(1,l,dimX); %dimX must make 1mm divisions of the space
39 X = repmat(x,dimY,1); %dimY dictates the precision of the integral
40 y = formfunction(x./l); %vector with the end positions of the Y matrix
41 Y = zeros(dimY,dimX);
42
43 for i=1:dimX
44 Y(:,i)= flip(linspace(1,y(i),dimY));
45 end
46
47 for i=1:dimX
48 y_pos = flip(linspace(y(i)/((dimY-1)/2),y(i),(dimY-1)/2));
49 y_neg = flip(linspace(-y(i),-y(i)/((dimY-1)/2),(dimY-1)/2));
50 Y(:,i)=[y_pos 0 y_neg];
51 end
52
53 %----Calculating power and energy----%
54
55 integr=0;
56 power = zeros(dimY,dimX);
57
58 for i=1:dimX
59 p_out = p_fun(x(i),xc,yc,sig_x,sig_y);
60
61 power(:,i) = exp(-((X(:,i)-xc).^2/(2*sig_x^2) + ...
        (Y(:,i)-yc).^2/(2*sig_y^2)));
62 integr = integr + integral(p_out,Y(dimY,i),Y(1,i));
63 end
64
65 power_target = integr*A/10^3;
66 energy = power_target*time;

```

Listing B.2: Power function (p_fun.m)

```

1 function f = p_fun(a,xc,yc,sig_x,sig_y)
2 f = @(t) exp(-(((a-xc)^2)/(2*sig_x^2) + ((t-yc).^2)/(2*sig_y^2)));
3 end

```

Listing B.3: Results and plots

```
1 %----Print results----%
2
3 fprintf('Peak power: %.2f MW/m2\n',A)
4 fprintf('Exposure time: %.2f s\n',time)
5 fprintf('Power on target: %.2f kW\n',power-target)
6 fprintf('Energy on target: %.2f kJ\n',energy)
7
8 %---Making some plots---%
9
10 mesh = pcolor(X,Y,zeros(size(X)));
11 set(mesh,'Edgecolor','blue'); %removes mesh grid lines
12 colormap('white');
13 drawnow
14
15 figure(2)
16 set(gca, 'FontSize', 18)
17 set(gcf, 'position', [34 164 560 420]);
18 set(gcf, 'paperUnits', 'centimeters', 'paperPosition', [0 0 10 ...
19     8], 'paperSize', [10 8])
20 hold off
21 h = surf(X, Y, power);
22 hold on
23 set(h, 'LineStyle', 'none')
24 set(gcf, 'paperUnits', 'centimeters', 'paperPosition', [0 0 18 ...
25     9], 'paperSize', [10 8])
26 c = colorbar;
```

Listing B.4: Output

```
1 Peak power: 15.00 MW/m2
2 Exposure time: 3.00 s
3 Power on target: 140.26 kW
4 Energy on target: 420.78 kJ
```

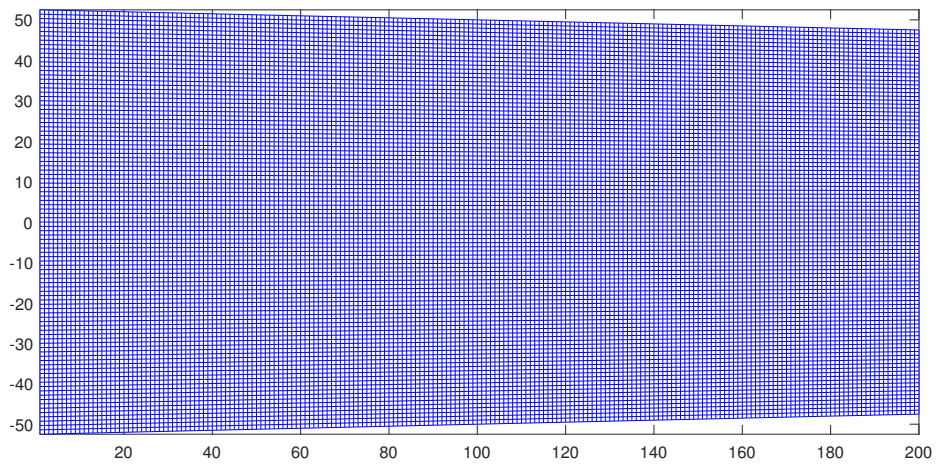


Figure B.1: Mesh of the trapezoidal calculation space.

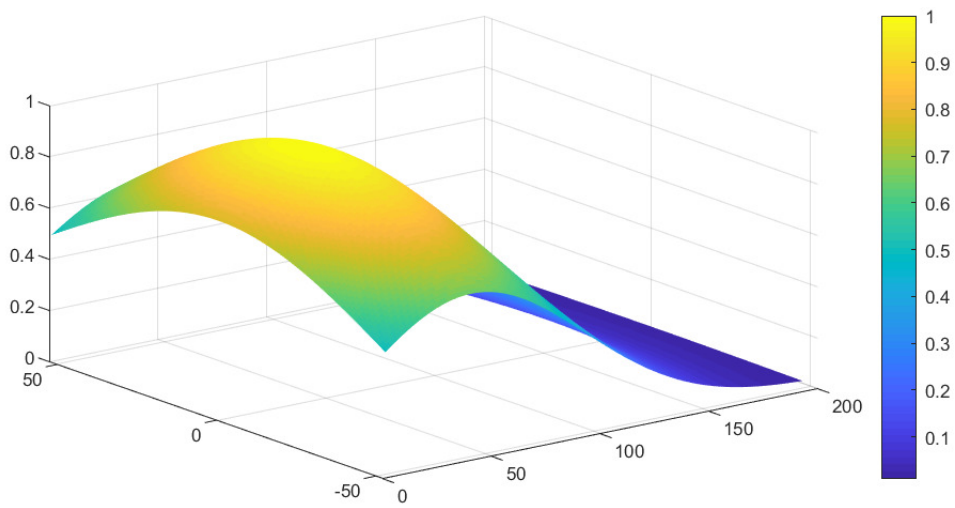


Figure B.2: Normalized power surface graph.

B.2 Bivariate Gaussian heat source in APDL

Bivariate Gaussian distribution for a 10 MW/m² applied during 3 s with σ_x and σ_y equal to 50 mm and 6 mm respectively. This APDL code had to be created to simulate the heat source in ANSYS Workbench and was used as an input command.

$$f(x, y) = A \cdot \exp \left[-\frac{(X - B)^2}{2 \cdot C^2} + \frac{(Y - D)^2}{2 \cdot E^2} \right] \quad (\text{B.1})$$

where

- A = Maximum heat flux.
- B, D = Centre coordinates.
- C, E = Standard deviation.

Listing B.5: APDL-Code

```

1 !   Commands inserted into this file will be executed just prior to ...
   !   the ANSYS SOLVE command.
2 !   These commands may supersede command settings set by Workbench.
3
4 !   Active UNIT system in Workbench when this object was created: ...
   !   Metric (m, kg, N, s, V, A)
5 !   NOTE: Any data that requires units (such as mass) is assumed to ...
   !   be in the consistent solver unit system.
6 !           See Solving Units in the help system for more ...
   !   information.
7
8
9 ! /INPUT,HFLUX_func,,,1
10
11
12
13
14 *DIM,HEAT_FLX1, TABLE,6,29,4,,,,,12
15 !
16 ! Begin of equation: {TIME}
17 *SET,HEAT_FLX1(0,0,1), 0.0, -999
18 *SET,HEAT_FLX1(2,0,1), 0.0
19 *SET,HEAT_FLX1(3,0,1), 0.0
20 *SET,HEAT_FLX1(4,0,1), 0.0
21 *SET,HEAT_FLX1(5,0,1), 0.0
22 *SET,HEAT_FLX1(6,0,1), 0.0
23 *SET,HEAT_FLX1(0,1,1), 1.0, 99, 0, 1, 1, 0, 0
24 *SET,HEAT_FLX1(0,2,1), 0
25 *SET,HEAT_FLX1(0,3,1), 0
26 *SET,HEAT_FLX1(0,4,1), 0
27 *SET,HEAT_FLX1(0,5,1), 0

```

```

28 *SET, HEAT_FLX1 (0, 6, 1), 0
29 *SET, HEAT_FLX1 (0, 7, 1), 0
30 *SET, HEAT_FLX1 (0, 8, 1), 0
31 *SET, HEAT_FLX1 (0, 9, 1), 0
32 *SET, HEAT_FLX1 (0, 10, 1), 0
33 *SET, HEAT_FLX1 (0, 11, 1), 0
34 *SET, HEAT_FLX1 (0, 12, 1), 0
35 *SET, HEAT_FLX1 (0, 13, 1), 0
36 *SET, HEAT_FLX1 (0, 14, 1), 0
37 *SET, HEAT_FLX1 (0, 15, 1), 0
38 *SET, HEAT_FLX1 (0, 16, 1), 0
39 *SET, HEAT_FLX1 (0, 17, 1), 0
40 *SET, HEAT_FLX1 (0, 18, 1), 0
41 *SET, HEAT_FLX1 (0, 19, 1), 0
42 *SET, HEAT_FLX1 (0, 20, 1), 0
43 *SET, HEAT_FLX1 (0, 21, 1), 0
44 *SET, HEAT_FLX1 (0, 22, 1), 0
45 *SET, HEAT_FLX1 (0, 23, 1), 0
46 *SET, HEAT_FLX1 (0, 24, 1), 0
47 *SET, HEAT_FLX1 (0, 25, 1), 0
48 *SET, HEAT_FLX1 (0, 26, 1), 0
49 *SET, HEAT_FLX1 (0, 27, 1), 0
50 *SET, HEAT_FLX1 (0, 28, 1), 0
51 *SET, HEAT_FLX1 (0, 29, 1), 0
52 ! End of equation: {TIME}
53 !
54 ! Begin of equation: 0
55 *SET, HEAT_FLX1 (0, 0, 2), 1, -999
56 *SET, HEAT_FLX1 (2, 0, 2), 0.0
57 *SET, HEAT_FLX1 (3, 0, 2), 0.0
58 *SET, HEAT_FLX1 (4, 0, 2), 0.0
59 *SET, HEAT_FLX1 (5, 0, 2), 0.0
60 *SET, HEAT_FLX1 (6, 0, 2), 0.0
61 *SET, HEAT_FLX1 (0, 1, 2), 1.0, 99, 0, 0, 0, 0, 0
62 *SET, HEAT_FLX1 (0, 2, 2), 0
63 *SET, HEAT_FLX1 (0, 3, 2), 0
64 *SET, HEAT_FLX1 (0, 4, 2), 0
65 *SET, HEAT_FLX1 (0, 5, 2), 0
66 *SET, HEAT_FLX1 (0, 6, 2), 0
67 *SET, HEAT_FLX1 (0, 7, 2), 0
68 *SET, HEAT_FLX1 (0, 8, 2), 0
69 *SET, HEAT_FLX1 (0, 9, 2), 0
70 *SET, HEAT_FLX1 (0, 10, 2), 0
71 *SET, HEAT_FLX1 (0, 11, 2), 0
72 *SET, HEAT_FLX1 (0, 12, 2), 0
73 *SET, HEAT_FLX1 (0, 13, 2), 0
74 *SET, HEAT_FLX1 (0, 14, 2), 0
75 *SET, HEAT_FLX1 (0, 15, 2), 0
76 *SET, HEAT_FLX1 (0, 16, 2), 0
77 *SET, HEAT_FLX1 (0, 17, 2), 0
78 *SET, HEAT_FLX1 (0, 18, 2), 0

```

```

79 *SET, HEAT_FLX1 (0,19,2), 0
80 *SET, HEAT_FLX1 (0,20,2), 0
81 *SET, HEAT_FLX1 (0,21,2), 0
82 *SET, HEAT_FLX1 (0,22,2), 0
83 *SET, HEAT_FLX1 (0,23,2), 0
84 *SET, HEAT_FLX1 (0,24,2), 0
85 *SET, HEAT_FLX1 (0,25,2), 0
86 *SET, HEAT_FLX1 (0,26,2), 0
87 *SET, HEAT_FLX1 (0,27,2), 0
88 *SET, HEAT_FLX1 (0,28,2), 0
89 *SET, HEAT_FLX1 (0,29,2), 0
90 ! End of equation: 0
91 !
92 ! Begin of equation: A*exp(-((X)-B)^2/(2*C^2)+({Y}-D)^2/(2*E^2)))
93 *SET, HEAT_FLX1 (0,0,3), 4, -999
94 *SET, HEAT_FLX1 (2,0,3), 0.0
95 *SET, HEAT_FLX1 (3,0,3), 0.0
96 *SET, HEAT_FLX1 (4,0,3), 0.0
97 *SET, HEAT_FLX1 (5,0,3), 0.0
98 *SET, HEAT_FLX1 (6,0,3), 0.0
99 *SET, HEAT_FLX1 (0,1,3), 1.0, -1, 0, 0, 0, 0, 0
100 *SET, HEAT_FLX1 (0,2,3), 0.0, -2, 0, 1, 0, 0, -1
101 *SET, HEAT_FLX1 (0,3,3), 0, -3, 0, 1, -1, 2, -2
102 *SET, HEAT_FLX1 (0,4,3), 0.0, -1, 0, 0.0, 0, 0, 2 !VAL6 defines x0
103 *SET, HEAT_FLX1 (0,5,3), 0.0, -2, 0, 1, 2, 2, -1
104 *SET, HEAT_FLX1 (0,6,3), 0.0, -1, 0, 2, 0, 0, -2
105 *SET, HEAT_FLX1 (0,7,3), 0.0, -4, 0, 1, -2, 17, -1
106 *SET, HEAT_FLX1 (0,8,3), 0.0, -1, 0, 0.050, 0, 0, 0 !VAL6 defines x ...
    standard deviation
107 *SET, HEAT_FLX1 (0,9,3), 0.0, -2, 0, 2, 0, 0, -1
108 *SET, HEAT_FLX1 (0,10,3), 0.0, -5, 0, 1, -1, 17, -2
109 *SET, HEAT_FLX1 (0,11,3), 0.0, -1, 0, 2, 0, 0, -5
110 *SET, HEAT_FLX1 (0,12,3), 0.0, -2, 0, 1, -1, 3, -5
111 *SET, HEAT_FLX1 (0,13,3), 0.0, -1, 0, 1, -4, 4, -2
112 *SET, HEAT_FLX1 (0,14,3), 0.0, -2, 0, 0.100, 0, 0, 3 !VAL6 defines y0
113 *SET, HEAT_FLX1 (0,15,3), 0.0, -4, 0, 1, 3, 2, -2
114 *SET, HEAT_FLX1 (0,16,3), 0.0, -2, 0, 2, 0, 0, -4
115 *SET, HEAT_FLX1 (0,17,3), 0.0, -5, 0, 1, -4, 17, -2
116 *SET, HEAT_FLX1 (0,18,3), 0.0, -2, 0, 0.006, 0, 0, 0 !VAL6 defines y ...
    standard deviation
117 *SET, HEAT_FLX1 (0,19,3), 0.0, -4, 0, 2, 0, 0, -2
118 *SET, HEAT_FLX1 (0,20,3), 0.0, -6, 0, 1, -2, 17, -4
119 *SET, HEAT_FLX1 (0,21,3), 0.0, -2, 0, 2, 0, 0, -6
120 *SET, HEAT_FLX1 (0,22,3), 0.0, -4, 0, 1, -2, 3, -6
121 *SET, HEAT_FLX1 (0,23,3), 0.0, -2, 0, 1, -5, 4, -4
122 *SET, HEAT_FLX1 (0,24,3), 0.0, -4, 0, 1, -1, 1, -2
123 *SET, HEAT_FLX1 (0,25,3), 0.0, -1, 0, 1, -3, 3, -4
124 *SET, HEAT_FLX1 (0,26,3), 0.0, -1, 7, 1, -1, 0, 0
125 *SET, HEAT_FLX1 (0,27,3), 0.0, -2, 0, 10e6, 0, 0, -1 !VAL6 defines max ...
    heat flux
126 *SET, HEAT_FLX1 (0,28,3), 0.0, -3, 0, 1, -2, 3, -1

```

```

127 *SET,HEAT_FLX1(0,29,3), 0.0, 99, 0, 1, -3, 0, 0
128
129 ! Begin of equation: A*exp(-((X)-B)^2/(2*C^2)+({Y}-D)^2/(2*E^2)))
130 !
131 ! Begin of equation: 0
132 *SET,HEAT_FLX1(0,0,4), 10, -999
133 *SET,HEAT_FLX1(2,0,4), 0.0
134 *SET,HEAT_FLX1(3,0,4), 0.0
135 *SET,HEAT_FLX1(4,0,4), 0.0
136 *SET,HEAT_FLX1(5,0,4), 0.0
137 *SET,HEAT_FLX1(6,0,4), 0.0
138 *SET,HEAT_FLX1(0,1,4), 1.0, 99, 0, 0, 0, 0, 0
139 *SET,HEAT_FLX1(0,2,4), 0
140 *SET,HEAT_FLX1(0,3,4), 0
141 *SET,HEAT_FLX1(0,4,4), 0
142 *SET,HEAT_FLX1(0,5,4), 0
143 *SET,HEAT_FLX1(0,6,4), 0
144 *SET,HEAT_FLX1(0,7,4), 0
145 *SET,HEAT_FLX1(0,8,4), 0
146 *SET,HEAT_FLX1(0,9,4), 0
147 *SET,HEAT_FLX1(0,10,4), 0
148 *SET,HEAT_FLX1(0,11,4), 0
149 *SET,HEAT_FLX1(0,12,4), 0
150 *SET,HEAT_FLX1(0,13,4), 0
151 *SET,HEAT_FLX1(0,14,4), 0
152 *SET,HEAT_FLX1(0,15,4), 0
153 *SET,HEAT_FLX1(0,16,4), 0
154 *SET,HEAT_FLX1(0,17,4), 0
155 *SET,HEAT_FLX1(0,18,4), 0
156 *SET,HEAT_FLX1(0,19,4), 0
157 *SET,HEAT_FLX1(0,20,4), 0
158 *SET,HEAT_FLX1(0,21,4), 0
159 *SET,HEAT_FLX1(0,22,4), 0
160 *SET,HEAT_FLX1(0,23,4), 0
161 *SET,HEAT_FLX1(0,24,4), 0
162 *SET,HEAT_FLX1(0,25,4), 0
163 *SET,HEAT_FLX1(0,26,4), 0
164 *SET,HEAT_FLX1(0,27,4), 0
165 *SET,HEAT_FLX1(0,28,4), 0
166 *SET,HEAT_FLX1(0,29,4), 0
167 ! End of equation: 0
168 !-->
169
170
171
172 sf,a1,hflux,%HEAT_FLX1%

```